

INFORMATION TO USERS

This manuscript has been reproduced from the microfilm master. UMI films the text directly from the original or copy submitted. Thus, some thesis and dissertation copies are in typewriter face, while others may be from any type of computer printer.

The quality of this reproduction is dependent upon the quality of the copy submitted. Broken or indistinct print, colored or poor quality illustrations and photographs, print bleedthrough, substandard margins, and improper alignment can adversely affect reproduction.

In the unlikely event that the author did not send UMI a complete manuscript and there are missing pages, these will be noted. Also, if unauthorized copyright material had to be removed, a note will indicate the deletion.

Oversize materials (e.g., maps, drawings, charts) are reproduced by sectioning the original, beginning at the upper left-hand corner and continuing from left to right in equal sections with small overlaps. Each original is also photographed in one exposure and is included in reduced form at the back of the book.

Photographs included in the original manuscript have been reproduced xerographically in this copy. Higher quality 6" x 9" black and white photographic prints are available for any photographs or illustrations appearing in this copy for an additional charge. Contact UMI directly to order.

UMI

A Bell & Howell Information Company
300 North Zeeb Road, Ann Arbor, MI 48106-1346 USA
313/761-4700 800/521-0600

The Pennsylvania State University
The Graduate School
Department of Industrial and Manufacturing Engineering

**MICRO-SCALE FREEFORM FABRICATION USING LOW-ENERGY
ELECTRON-BEAM DEGRADATION**

A Thesis in
Industrial and Manufacturing Engineering

by
Brian Kevin Paul

Submitted in Partial Fulfillment
of the Requirements
for the Degree of

Doctor of Philosophy
August 1995

UMI Number: 9600231

UMI Microform 9600231

Copyright 1995, by UMI Company. All rights reserved.

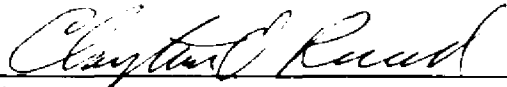
**This microform edition is protected against unauthorized
copying under Title 17, United States Code.**

UMI

**300 North Zeeb Road
Ann Arbor, MI 48103**

We approve the thesis of Brian Kevin Paul.

Date of Signature



Clayton O. Ruud
Professor of Industrial Engineering
Thesis Co-Advisor
Co-Chair of Committee

6/30/95



Randall M. German
Professor, Brush Chair in Materials
Thesis Co-Advisor
Co-Chair of Committee

5 July 95



Paul H. Cohen
Professor of Industrial Engineering

June 30, 1995



Allen L. Soyster
Professor of Industrial Engineering
Head of the Department of Industrial and Manufacturing Engineering

July 10, 1995

ABSTRACT

Future micro-mechanical systems will consist of circuits, actuators, sensors, power sources, manipulators, and other components all integrated onto a single chip. To achieve this sophistication, future microfabrication technologies must be capable of precision mechanical fabrication and assembly. The object of this thesis has been to apply additive freeform fabrication principles to micro-mechanical fabrication and assembly. The approach has been to use low-energy electron beams to selectively pattern layers of electron resist and to dissolve away exposed regions in a development solvent. The expected advantages of this approach include its ability to fabricate pre-assemblies and its sub-micrometer resolution leading to high aspect ratios, good surface texture, and sub-micrometer dimensional precision.

A critical issue in the development of this process is dimensional control of the voxel geometry created by taking a single electron beam scan across the surface of an electron resist. A low-energy electron penetration profile (LEEPP) model was developed to predict voxel geometry dimensions based on various material and process conditions. Subsequently, an investigation was initiated to validate this model and to use the knowledge obtained for fabricating a multi-layer micro-structure.

Model validation was sought by comparing model results with data from the low-energy electron microlithography literature. The use of literature data during model validation revealed that large discrepancies exist between the values used for the critical dosage for dissolution. Use of the model to reconcile these discrepancies was found to add credibility to the model. Further validation of the model was sought by exposing an electron resist within an environmental scanning electron microscope (ESEM).

As a result of this investigation, it was found that low-energy electron beams can be used to create voxels suitable for micro-scale freeform fabrication since they reduce the scattering range of the penetrating electrons resulting in limited proximity effects. In

addition, it was found that under proper conditions, the dimensional resolution of the proposed process exceeds that of existing micro-scale freeform fabrication techniques. Potential issues for further development include electrostatic charging of the resist, layering of the resist, and three-dimensional resist development.

TABLE OF CONTENTS

| | |
|---|----------|
| LIST OF FIGURES | ix |
| LIST OF TABLES | xii |
| ACKNOWLEDGMENTS..... | xiii |
| 1. INTRODUCTION..... | 1 |
| 1.1. Investigative Summary..... | 4 |
| 1.2. Thesis Organization | 6 |
| 2. BACKGROUND | 7 |
| 2.1. Micro-Mechanical Fabrication..... | 7 |
| 2.2. Freeform Fabrication..... | 9 |
| 2.2.1. Processes..... | 10 |
| 2.2.1.1. Subtractive..... | 12 |
| 2.2.1.2. Additive | 15 |
| 2.2.1.2.1. StereoLithography | 16 |
| 2.2.1.2.2. Solid Ground Curing | 22 |
| 2.2.1.2.3. Selective Laser Sintering | 25 |
| 2.2.1.2.4. Fused Deposition Modeling..... | 28 |
| 2.2.1.2.5. Three-Dimensional Printing..... | 30 |
| 2.2.1.3. Hybrid | 32 |
| 2.2.1.3.1. Laminated Object Manufacturing | 32 |
| 2.2.1.3.2. Other Hybrid Processes | 35 |
| 2.2.2. Applications..... | 36 |
| 2.2.2.1. Functional Testing..... | 37 |
| 2.2.2.2. Tooling..... | 38 |

| | |
|---|----|
| 2.2.2.3. Bio-Medical | 43 |
| 2.2.2.4. Microfabrication | 45 |
| 2.2.3. Technological Issues..... | 46 |
| 2.2.3.1. Voxel Geometry | 46 |
| 2.2.3.2. Material Addition Rate | 48 |
| 2.2.3.3. Surface Finish and Texture..... | 51 |
| 2.2.3.4. Dimensional Accuracy | 53 |
| 2.2.3.5. Material Properties..... | 56 |
| 2.2.3.6. Equipment Size and Work Envelope | 57 |
| 2.3. Electron Beam Processing..... | 59 |
| 2.3.1. Scattering..... | 60 |
| 2.3.2. Polymerization..... | 62 |
| 2.3.3. Cross-Linking and Chain Scission..... | 63 |
| 2.3.4. Process Models..... | 65 |
| 2.3.4.1. Polymer Coating Models | 66 |
| 2.3.4.2. Micro-Lithography Models..... | 68 |
| 3. STATEMENT OF PROBLEM | 73 |
| 3.1. Thesis Statement..... | 74 |
| 3.2. Objectives of the Proposed Research..... | 74 |
| 4. PRELIMINARY INVESTIGATION..... | 77 |
| 4.1. Simple, Electron Energy Dissipation Model..... | 77 |
| 4.2. Experimental Setup and Design | 83 |
| 4.3. Experimental Procedure..... | 86 |
| 4.4. Preliminary Results..... | 88 |
| 4.5. Preliminary Findings..... | 91 |

| | |
|--|-----|
| 5. PRIMARY INVESTIGATION..... | 93 |
| 5.1. Low-Energy Electron Penetration Profile (LEEPP) Model..... | 93 |
| 5.2. Model Implementation | 102 |
| 5.3. Comparison of LEEPP Model with Existing Models | 105 |
| 5.4. Model Validation..... | 108 |
| 5.5. Experimental Setup and Design..... | 114 |
| 5.6. Experimental Procedure..... | 116 |
| 6. FINDINGS | 118 |
| 6.1. Experimental Results..... | 118 |
| 6.1.1. Baseline Data | 118 |
| 6.1.2. Development Time Effects | 127 |
| 6.1.3. Chamber Pressure Effects..... | 127 |
| 6.2. Analysis of Results..... | 129 |
| 6.3. Multi-Layer Micro-Structure | 137 |
| 7. SUMMARY AND CONCLUSIONS..... | 140 |
| 7.1. Investigations | 141 |
| 7.2. Conclusions | 141 |
| 7.3. Application Potential | 143 |
| Appendix A. EXPERIMENTAL PROCEDURE FOR THE PRELIMINARY INVESTIGATION..... | 145 |
| Appendix B. SAMPLE MATHCAD PLUS 5.0 IMPLEMENTATION OF THE LOW- ENERGY ELECTRON PENETRATION PROFILE (LEEPP) MODEL..... | 149 |
| Appendix C. SAMPLE EXPERIMENTAL PROCEDURE FOR PREPARING, EXPOSING, AND DEVELOPING LOW-ENERGY ELECTRON PENETRATION PROFILES IN ELECTRON RESIST..... | 157 |
| Appendix D. CALCULATIONS OF THE AVERAGE ABSORBED DOSE IN THE ELECTRON RESIST..... | 162 |

REFERENCES..... 164

LIST OF FIGURES

| | |
|--|----|
| Figure 1.1. Micro-mechanical actuator showing the intricate mechanical geometries which must be fabricated and assembled [GIAN92]. The diameter of the gear is roughly that of a human hair. | 2 |
| Figure 2.1 Coordinate system for additive RP technologies. | 16 |
| Figure 2.2. Schematic of SLA process. | 17 |
| Figure 2.3. Schematic of the different SL methods including: (Top left) Descending platform; (Top right) Ascending suspension; (Bottom left) Ascending surface; (Bottom right) Masked-lamp descending platform. | 19 |
| Figure 2.4. Schematic of SGC process. | 23 |
| Figure 2.5. Schematic of SLS process. | 25 |
| Figure 2.6. Schematic of FDM process. | 29 |
| Figure 2.7. Schematic of 3DP process. | 31 |
| Figure 2.8. Schematic of LOM process. | 33 |
| Figure 2.9. Components of an engineering tooling assembly. | 41 |
| Figure 2.10. Schematic view of the SLA voxel geometry. | 47 |
| Figure 2.11. Stair-stepping effect due to additive freeform fabrication of a curved surface. | 52 |
| Figure 2.12. Depth-dose curve for 25 keV electrons in carbon. | 62 |
| Figure 2.13. Kinetic curves of dissolution as a function of dose for a positive EB resist. Four curves represent four different exposure doses. | 66 |
| Figure 2.14. Schematic of EB lithography process showing the scattering of the electron beam and its interaction with both the electron resist and the resist substrate. | 69 |
| Figure 2.15. Schematic of low-energy EB lithography process showing a much smaller interaction with both the electron resist and the resist substrate. | 71 |
| Figure 3.1. Graphical depiction of the model objectives. | 75 |
| Figure 4.1. Coordinate system for the approach used in the preliminary investigation. | 78 |
| Figure 4.2. Experimental design for the preliminary investigation. | 85 |
| Figure 4.3. Schematic of the sample holder used in the preliminary investigation. | 86 |

| | |
|---|-----|
| Figure 4.4. Micrograph of the multi-layer micro-structure formed during the preliminary investigation..... | 91 |
| Figure 5.1. Coordinate system for the model developed in the primary investigation. | 95 |
| Figure 5.2. Summary of the model implementation showing the interrelationships between model parameters and variables. All input parameters are shown on the left with the result being the linewidth at each depth, z, found in the lower right. | 103 |
| Figure 5.3. Comparison of LEEPP model linewidth results with Wolf, et al. [WOLF71], for 5 keV electrons over a range of exposure doses (line charge densities). The critical dosage for dissolution used in the model was $1.5 \cdot 10^{22}$ eV/cm ² | 110 |
| Figure 5.4. Comparison of LEEPP model linewidth results with Possin and Norton, 1975 for 5 keV electrons over a range of exposure doses (line charge densities). The critical dosage for dissolution used in the model was $0.68 \cdot 10^{22}$ eV/cm ² | 112 |
| Figure 5.5. Comparison of LEEPP model linewidth results with Sugita and Tamamura [SUGI88] for 5 keV electrons over a range of exposure doses (line charge densities). The critical dosage for dissolution used in the model was $6.0 \cdot 10^{23}$ eV/cm ² | 114 |
| Figure 5.6. Comparison of LEEPP model linedepth results with Sugita and Tamamura [SUGI88] for 5 keV electrons over a range of exposure doses (line charge densities). The critical dosage for dissolution used in the model was $6.0 \cdot 10^{21}$ eV/cm ² | 115 |
| Figure 6.1. A micrograph of a voxel profile. | 120 |
| Figure 6.2. Comparison of LEEPP model linewidth with baseline experimental results for 5 keV electrons over a range of exposure doses (line charge densities). The critical dosage for dissolution used in the model was $0.9 \cdot 10^{22}$ eV/cm ² | 121 |
| Figure 6.3. Comparison of LEEPP model linedepth with baseline experimental results for 5 keV electrons over a range of exposure doses (line charge densities). The critical dosage for dissolution used in the model was $0.9 \cdot 10^{22}$ eV/cm ² | 121 |
| Figure 6.4. A micrograph of a sample profile showing problems encountered with cleaving the sample. | 122 |
| Figure 6.5. A micrograph showing problems related to improper mounting of the sample on the sample holder. | 123 |
| Figure 6.6. A micrograph of the top of a resist sample showing the image which was measured for collecting linewidth data. | 123 |
| Figure 6.7. A micrograph showing the elimination of profile undercutting in thick resist. | 124 |
| Figure 6.8. A second micrograph showing the elimination of profile undercutting in thick resist. | 125 |
| Figure 6.9. A low-magnification micrograph of sample to be imaged showing that an angle exists between the profile surface and the microscope's line-of-sight. | 125 |

| | |
|--|-----|
| Figure 6.10. A micrograph showing the negative-resist behavior in PMMA at high exposure doses. The exposure was for a 5 keV beam incident on 0.4 micrometers of PMMA coated on a Si substrate. | 126 |
| Figure 6.11. Graph showing the effect of development time on electron penetration profile dimensions. Samples were developed in a 1:3 solution of MIBK:IPA in approximately 0.7 μm of resist. | 128 |
| Figure 6.12. Graph showing the effect of chamber pressure on linewidth in 0.7 micrometers of PMMA resist. Preparation, exposure, and development conditions of the samples were the same..... | 129 |
| Figure 6.13. Example beam current distribution at specimen surface in typical ESEM as a result of beam scattering in the vapor environment. The flared portion at the base of the distribution is called the beam skirt..... | 130 |
| Figure 6.14. Graph showing the magnitude of difference between the data of Wolf and Possin/Norton relative to the data in Figure 6.10..... | 131 |
| Figure 6.15. A micrograph showing the results of a sample exposed at a chamber pressure less than 0.1 torr under a high exposure dose. | 134 |
| Figure 6.16. A micrograph showing the results of a sample exposed at a chamber pressure setting of 0.4 torr under a high exposure dose..... | 134 |
| Figure 6.17. A micrograph of a UV-cured micro-mechanical part showing the potential for stress risers on the surface [IKUT94]. | 136 |
| Figure 6.18. A micrograph showing EB-generated voxels with dimensions well below 1 μm | 136 |
| Figure 6.19. A micrograph showing 0.5 μm stairsteps fabricated by the MicroFFED process. The picture shows three layers (A, B, and C) with B and C being 0.5 and 1.0 μm deeper than A, respectively..... | 138 |

LIST OF TABLES

| | |
|--|-----|
| Table 1.1. Effect of micro-scale dimensions on thermal expansion..... | 1 |
| Table 1.2. Effect of micro-scale dimensions on material stresses. Two cubes of material affixed to a substrate. | 1 |
| Table 2.1. Summary of some machining processes..... | 14 |
| Table 2.2. Material properties of pressed and LOM-fabricated alumina bars. | 35 |
| Table 2.3. Comparison of RP processes for producing investment-casting patterns. | 40 |
| Table 2.4. Comparison of metal properties for DTM RapidTool™..... | 43 |
| Table 2.5. Material addition rates (MARs) calculated for various RP vendors. | 49 |
| Table 2.6. Comparison of material addition rates when using the same layer thickness (0.1 mm). For scanning based RP systems, the same sized voxel was used (0.02 mm ³)..... | 50 |
| Table 2.7. Extrapolated effect of layer thickness on build rates for the SLA -500/30..... | 52 |
| Table 2.8. Dimensional accuracies claimed by various RP vendors. | 53 |
| Table 2.9. Material properties claimed by various RP material vendors..... | 57 |
| Table 2.10. Equipment size, weight, and work envelope of various RP machines. | 58 |
| Table 2.11. Analysis of equipment cost to work envelope for several RP systems..... | 59 |
| Table 2.12. Parameters affecting resist sensitivity. | 65 |
| Table 4.1. Preliminary results showing feasibility for micro-scale EB process..... | 88 |
| Table 5.1. Various computed values from the computer implementation of Equation 5.9 (i.e. the LEEPP model)..... | 106 |
| Table 5.2. Various computed values from the computer implementation of Equation 5.10 (i.e. the LITHOS model [GLEZ92]) implemented as a part of this thesis..... | 106 |
| Table 6.1. A comparison of the average absorbed doses calculated using solubility rates and the LEEPP model over a range of development times. | 133 |

ACKNOWLEDGMENTS

Many people contributed to the successful completion of this dissertation. First, I thank my wife, Lynn, for her encouragement and commitment to me over the course of my doctoral education. In addition to being a good mother, she spent endless hours editing this dissertation manuscript. Next, I thank my advisors Randall German and Clayton Ruud for their vital participation. Professor German's wisdom and technological vision were critical elements of my success along with Professor Ruud's receptivity and seasoned pragmatism. I thank Dr. Paul Cohen and Dr. Allen Soyster, each, for their participation as committee members. I also thank Terry Doherty and Russ Rhoads of the Department of Energy's Pacific Northwest Laboratory for their confidence and timely financial support. Special thanks goes to that small group of people on South Atherton Street who encouraged my life considerably and who prayed for me faithfully over the last six months of my doctoral work. Finally, I thank Christ Jesus, himself, who gives my life meaning and purpose. In addition to providing me with a research topic, research funding, a theoretical model, and experimental results, He gave me the strength to endure it all.

1. INTRODUCTION

The miniaturization of electronic systems has revolutionized world society in a relatively short 30-year period. Motivated by this wave of technological success, present-day research groups from around the world have begun to demonstrate the advantages afforded by miniaturizing mechanical systems. In fields such as medicine and biology, many researchers have begun to exploit the greater mechanical precision which can be achieved by smaller instruments and machines. As shown in Table 1.1, this improved precision is in part due to the diminishing effect of thermal expansion on dimensional error at the micro-scale [SLOC92]. Similarly, the effects of vibration on dimensional error are also greatly diminished at the micro-scale [TRIM87].

Table 1.1. Effect of micro-scale dimensions on thermal expansion.

| | Cast Iron | Silicon |
|--|---------------------|----------------------|
| Length of arm (m) | 1 | $1 \cdot 10^{-5}$ |
| Coefficient of thermal expansion | $1.1 \cdot 10^{-5}$ | $0.5 \cdot 10^{-5}$ |
| Expansion due to increase of 1°C (m) | $1.1 \cdot 10^{-5}$ | $0.5 \cdot 10^{-10}$ |

Another advantage being exploited by micro-mechanical researchers involves the reduced structural requirements imposed on materials at the micro-scale. Table 1.2 shows the diminishing effect of micro-scale dimensions on material stresses. This effect suggests

Table 1.2. Effect of micro-scale dimensions on material stresses. Two cubes of material affixed to a substrate.

| | Cast Iron | Silicon |
|---|--------------------|---|
| Dimensions (m) | 1 x 1 x 1 | $10^{-5} \times 10^{-5} \times 10^{-5}$ |
| Area of face affixed to substrate (cm^2) | 10^4 | 10^6 |
| Volume of cube (cm^3) | 10^6 | 10^9 |
| Density (g/cm^3) | 7.9 | 2.3 |
| Gravity (cm/s^2) | 980 | 980 |
| Avg. stress at the joining surface (Pa) | $7.742 \cdot 10^4$ | $2.254 \cdot 10^4$ |

that weaker materials, such as silicon and conductive polymers, may be used in many micro-mechanical applications making the integration of electrical and mechanical components much easier [PETE82].

Other advantages of micro-mechanical systems include the effects of micro-scale proportions on mechanical responsiveness, energy efficiency, portability, and cost. Efforts are currently being made to exploit these advantages in mechanisms designed to deliver insulin [VANL88], monitor blood pressure [O'CON93], inject engine fuel, heat and air condition homes, and cool micro-electronic circuits [BUHR92]. Figure 1.1 shows an electric motor which could be used to actuate micro-surgery tools for brain surgeons [GIAN92].

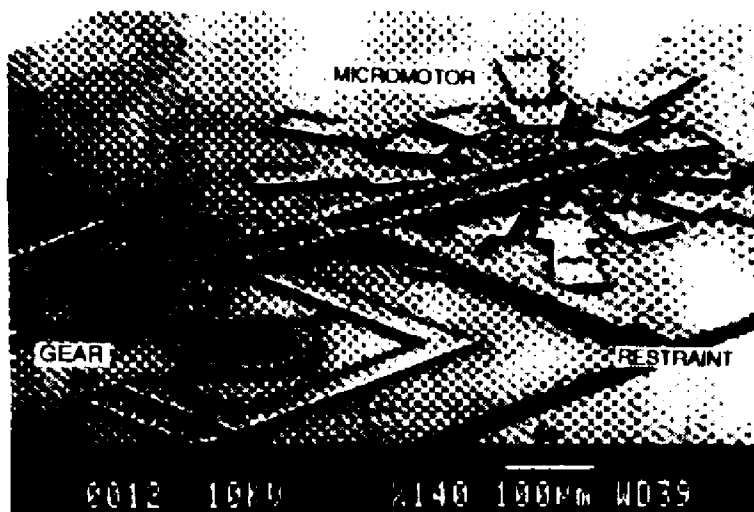


Figure 1.1. Micro-mechanical actuator showing the intricate mechanical geometries which must be fabricated and assembled [GIAN92]. The diameter of the gear is roughly that of a human hair.

To deliver these capabilities, future micro-mechanical systems will need to consist of circuits, actuators, sensors, power sources, manipulators, end effectors, and other components integrated onto a single chip. While much progress has been made in fabricating integrated circuits with on-chip mechanical sensors or in fabricating individual

actuators, little success has been made in fabricating integrated micro-devices consisting of multiple electrical, optical, or mechanical components. To achieve this end, one significant challenge will be the coupling of force and communication of data between individual components of the system.

As mentioned, few attempts have been made to couple multiple micro-components into an integrated system. Approaches involving bulk silicon micro-machining all require some extent of alignment and assembly [GIAN92]. Despite efforts to address challenges [RUSS93], research in micro-assembly techniques is still very primitive [WISE91]. *In situ* fabrication techniques employed by surface micro-machining and the LIGA (x-ray lithography, electroplating, and molding) process have permitted the generation of pre-assembled, freely rotating microstructures [MULL90], [MENZ91]. The predominate *in situ* fabrication technique involves the use of a sacrificial layer of material upon which a micro-mechanical superstructure can be built. After fabricating the superstructure, the sacrificial layer is etched, selectively releasing pre-assembled micro-mechanisms from the substrate. However, linkages between mechanical components formed using these techniques are constrained to lie in the same plane as the components themselves (i.e. gears).

Single-step, *in situ* fabrication methods capable of producing non-planar, pre-assembled micro-structures are needed to simplify the coupling of mechanical parts within micro-mechanical systems. Such methods must be capable of fabricating complex mechanical structures consisting of integrated moving parts each having high dimensional precision [JUDY91] and smooth surface texture [MORI93].

At normal-scales, one fabrication method capable of producing *in situ* pre-assemblies is that of *additive freeform fabrication*. Also known as *rapid prototyping*, *desktop manufacturing*, and *toolless manufacturing*, freeform fabrication methods are receiving much research attention largely due to their many applications in manufacturing

product development. Freeform fabrication methods include both subtractive methods, such as six-axis robotic end milling with a ball mill, and additive methods, such as StereoLithography. Additive freeform fabrication methods can be distinguished from subtractive methods in that the final part is built up layer-by-layer rather than machined from a workpiece. Additive freeform fabrication methods are unique among manufacturing methods in that many of them can fabricate a “ship-in-a-bottle”.

In particular, Solid Ground Curing is an additive freeform process specifically adept at fabricating pre-assemblies. This process constructs mechanical components layer-by-layer by shining light from a high-power UV lamp through a photo-mask to selectively solidify regions of a photo-resin layer. Its unique ability to fabricate pre-assemblies with reasonably good tolerances is largely due to the backfilling of uncured photo-resin with solid wax after exposure under the photo-mask. Thus, each layer is fabricated upon a solid substrate and does not require supports to fabricate difficult-to-build geometries such as cantilevers. After the part is fabricated, the solid cube of resin and wax can be washed with hot water to remove the wax. This process has been used to fabricate pre-assembled mechanical devices such as universal joints and three-dimensional gear meshes [BURN93].

1.1. Investigative Summary

In this thesis, an investigative procedure was conducted with the goal to develop a superior micro-scale freeform fabrication process capable of pre-assembly. Current methods of micro-scale freeform fabrication use ultra-violet (UV) irradiation of monomers and metallic vapors. Preliminarily, electron-beam (EB) irradiation was chosen as the micro-fabrication method in this thesis due to the improved resolution of electron beams over UV rays and lasers. Initially, a simple, electron energy dissipation model was developed to understand the physics involved with EB irradiation. A preliminary investigation was conducted to experimentally validate the improved resolution expected of

EB irradiation. The fabrication approach used in the preliminary investigation involved the vapor deposition and EB polymerization of a monomer on an aluminum substrate. Results from the preliminary experimentation suggested a need to incorporate electron scattering into the model. In addition, it was determined that the requirements for the ideal EB micro-scale pre-assembly method included: 1) use of low-energy electrons; 2) fabrication in solid material systems for in-process support of the part being fabricated; and 3) removal of the excess material (i.e. supports) in a post-process.

A second, primary investigative procedure was undertaken to develop a fabrication method capable of micro-scale pre-assembly. The fabrication approach used in the primary investigation used electron beams to selectively depolymerize layers of electron resist and was called Micro-scale Freeform Fabrication using Electron-beam Degradation (MicroFFED). Sequentially, MicroFFED involves the following process steps: 1) layering of electron resist; 2) selective degradation of the polymer with an electron beam; and 3) removal of the exposed polymer via chemical development in a post-process. The advantages afforded by this process over existing micro-mechanical fabrication processes include its ability to fabricate pre-assemblies and its sub-micrometer resolution leading to high aspect ratios, good surface texture, and sub-micrometer dimensional precision and repeatability. It is expected that this process could be used to fabricate integrated micro-systems directly from a conductive polymer or indirectly from a mold using electro-forming techniques or as a net shaping technique for micro-scale powder processing.

The key issue addressed in the primary investigation involved the prediction of the voxel (volume element) geometry generated by scanning a low-energy electron beam over the surface of an electron resist. The voxel geometry is the geometry below the surface of the electron resist affected by the electron beam-material interaction. Current models for predicting voxel dimensions produced by low-energy electron beams do not exist. Prediction of this geometry is crucial for controlling the MicroFFED process. Such

information can be used in optimizing such parameters as distance between adjacent beam scans, layer thickness, energy efficiency, and surface texture.

As part of the primary investigation, a low-energy electron penetration profile (LEEPP) model was developed to predict the voxel linewidth and linedepth. Model validation involved the comparison of model results with linewidth and linedepth from the literature. Further validation of the LEEPP model was conducted via experimentation. A final effort was made to fabricate a three-dimensional micro-structure to test the feasibility of the proposed MicroFFED process.

1.2. Thesis Organization

The organization of this thesis is as follows. Background material in micro-mechanical fabrication, freeform fabrication, and electron-beam processing is provided in Chapter 2. Specific objectives of the research are outlined in Chapter 3. The preliminary model and investigative procedure are described in detail in Chapter 4. The primary model and investigative procedure are discussed in Chapter 5. Results from the primary investigation are discussed in Chapter 6. Further discussion in Chapter 6 concerns the fabrication of a multi-layer micro-structure which confirms some of the benefits expected of the MicroFFED process. Chapter 7 summarizes the thesis including the conclusions drawn and potential applications.

2. BACKGROUND

Micro-fabrication research is being conducted in many different fields involving many different types of components including electrical, optical, and mechanical, to name a few. Research conducted in conjunction with this work involves the fabrication of micro-mechanical components specifically, though it is expected that these techniques could be extended to other areas of micro-fabrication research as well.

This chapter includes literature summaries of several topics related to *in situ* micro-mechanical fabrication. Following a review of current micro-mechanical fabrication technologies is a summary of freeform fabrication technologies including pertinent voxel geometry models. Subsequently, several electron-beam microlithography models for predicting energy deposition profiles are reviewed. Finally, a problem statement and hypothesis are presented to establish the conditions under which MicroFFED is expected to advance micro-mechanical fabrication.

2.1. Micro-Mechanical Fabrication

Many net-shape micro-mechanical fabrication technologies currently exist most of which are extensions to conventional microelectronics fabrication technology. Most proliferate are the bulk- and surface-micromachining techniques based mainly on lithography, etching, and epitaxy of Si [FARO92], [ENGE92] and GaAs [HJOR90]. In bulk-micromachining, a lithography mask is developed on top of a bulk substrate and a subsequent anisotropic etching process is used to selectively remove material. In surface-micromachining, thin films of different materials are sequentially deposited and etched using epitaxial growth, lithography, and selective etching techniques. While well-developed, micromachining techniques are limited by small aspect ratios [FRAZ92] with the number of net shapes being restricted by the crystallographic orientation of the substrate [ENGE92].

More recently, x-ray and deep UV lithography techniques have been exploited to overcome these limitations. In particular, the LIGA process [MENZ91], based on x-ray microlithography, is desirable because it is capable of producing micro-devices with high aspect ratios, highly parallel edges, and micrometer-scale precision. Microstructures with aspect ratios of up to 100 have been demonstrated. The LIGA process involves three process steps. First, an x-ray resist on the order of 350 μm in thickness is exposed through a lithography mask by x-ray synchrotron radiation. Exposure times can range from one half hour to several hours depending upon the thickness of the resist. The resulting layer of resist is developed in an organic developer to dissolve unwanted material, forming a lateral-shaped polymeric pattern. Next, the polymeric pattern is used to form a metal mold insert via an electroforming process. Finally, the insert is used in an injection molding process for the mass production of polymeric microstructures.

As a whole, the LIGA process is restricted to the *extrusion* of a 2D lithography mask and, therefore, is limited to lateral-shaped microstructures [ENGE92]. In addition, the LIGA process is dependent upon high-cost synchrotron x-radiation [O'CON93]. A less costly alternative to the LIGA process utilizes deep UV lithography [ENGE92], [FRAZ92] but, like the LIGA process, also requires a lithography mask and is restricted to lateral-shaped geometries.

Other net-shape microfabrication techniques have exploited laser-beam, electron-beam, ion-beam, and plasma-assisted material deposition and removal. Several laser and electron-beam-assisted chemical vapor deposition methods have been proposed [BRUN92], [BOMA92]. Ion-beam milling uses the physical bombardment of ions to selectively erode material while reactive ion etching uses a gaseous etchant to chemically remove material through a lithography mask [BROD82]. While many of these methods allow direct fabrication in metal, they are very slow and are limited to a small range of geometries.

Today, two major prohibitions stand in the way of proliferating micromachine applications [FUJI93]. First, unfortunately as the size of machines becomes smaller, the number of control signals does not get smaller. Thus, in coupling micro-components, the data and control paths can be as large as the micromachine itself. This suggests the need for greater integration of micro-components and micro-electronics to reduce the need for physical cabling between components. And second, despite significant progress in micro-mechanical fabrication techniques, efficient, high-volume fabrication and assembly of integrated microelectromechanical systems is still an issue [WISE91].

2.2. Freeform Fabrication

Freeform fabrication is a relatively new term used to describe an emerging technology capable of fabricating complex, unsymmetrical surfaces and contours. Many analogous terms have been used to describe it. *Rapid prototyping* (RP) suggests that the technology is capable of faster, cheaper product development which can ultimately impact customer satisfaction and future profits. *Desktop manufacturing* refers to the size and convenience of the technology and is analogous to the term “desktop publishing” used in the publishing industry. In addition, the term *3D printing* has been used to describe the technology and draws an analogy between it and the ubiquitous laser printer used to produce two-dimensional computer graphics. Finally, the term *tool-less manufacturing* has been used to emphasize that some freeform fabrication technologies require no specialized tooling providing the added advantage of short setups. Overall, these terms describe a technology ideal for fabricating one-of-a-kind items with complex geometries. Throughout the remainder of this section, this type of technology will be referred to as RP technology.

In this section, an effort will be made to differentiate between the applications, methods, and processes of RP. To begin with, the term rapid prototyping itself describes an application. While many new flexible manufacturing technologies are being labeled RP

technologies, the applications of these technologies are not limited to prototyping. Other applications such as rapid tooling and direct rapid fabrication have been implemented in fields as diverse as manufacturing, architecture, medicine, archaeology, and the arts. It is also important to realize that rapid prototyping is not limited to mechanical part prototyping. The term rapid prototyping is also used to refer to the prototyping of software and microelectronic products, though in this section we will focus on the application to mechanical part prototyping and fabrication.

Moreover, several different methods can exist for implementing any one application. For example, rapid prototyping of mechanical parts can be carried out by *subtractive, additive, or hybrid* fabrication processes [BURN93]. The term subtractive can be used to classify processes which remove material from some bulk workpiece or raw material. A five axis milling machine with an end ball mill can be classified as a subtractive fabrication process used for rapid prototyping. The term additive can be used to classify a new set of processes which “build-up” parts layer-by-layer. StereoLithography is an additive fabrication process used for rapid prototyping. Hybrid refers to those flexible fabrication processes which are a combination of subtractive, additive, or formative processes. The Laminated Object Manufacturing (LOM) process which uses a laser to ablate layers of bonded paper is an example of a hybrid additive-subtractive process.

2.2.1. Processes

The heart of the RP field is the material processing equipment used to fabricate parts and prototypes. Process development in this field has been motivated by a vision of future manufacturing industry leading to several trends among RP process technologies. In the future, it is imagined that designers will work to turnaround customized products within very short time horizons. As a result, one emphasis within the RP field has been on reducing the *setup* and increasing the *throughput* of RP processes while minimizing the

secondary processing requirements of RP parts. Efforts to reduce setup times in RP processes have resulted in the name tool-less manufacturing technologies. By tool-less it is meant the lack of specialized tools specific to any group of products. Tool-less manufacturing reduces the amount of time spent preparing for material processing and increases the overall utilization of equipment.

In addition, it has been suggested that future designers will need to be less constrained in the number of design iterations conducted in meeting specific requirements. Some futurists have expressed this by suggesting that if current product development efforts follow the “ready, aim, fire” approach, future efforts will become “ready, fire, aim”. RP processes will help manufacturers turnaround design iterations quicker and cheaper as they become more accessible to design engineers. A current trend toward greater process *accessibility* can be evidenced by observing the *shrinking “footprints”* and *lower costs* of many RP processes. The antithesis of accessibility is *work envelope*. The work envelope of a process is the largest product volume which it can handle. While some processes are shrinking in size, other processes have become larger to deal with larger product sizes. These two trends (smaller desktop units vs. larger machine tool units) mark the first product segmentation within the RP market.

Finally, it is hoped that future designers will add more value to products more quickly, being more concerned with customer requirements than manufacturability constraints. This vision has led to the trend to develop processes unlimited by *geometric complexity* of the product design. Some processes have unlimited capabilities for producing geometries of any shape while other processes may require the “in-process” fabrication of supports for cantilevered designs. Some processes are possibly even capable of fabricating tailored micro- and milli-structures within the product.

Such trends can be used in comparing and contrasting the capabilities of the various RP processes. These attributes are used to contrast and differentiate the various processes

described below. Other attributes used below to contrast and compare RP processes include *dimensional accuracy*, *surface texture*, and *material properties*.

2.2.1.1. Subtractive

Most common within industry, subtractive fabrication is carried out on machining equipment such as milling machines and lathes. Since the early 1960's, much progress has been made toward the goal of computerizing machining processes. Today, well over 100 vendors of CNC machining equipment exist in the world. Consequently, this section does not contain an exhaustive list of vendors and machine capabilities but rather contains a summary of current CNC machining capabilities for comparison with the more recently developed additive fabrication technologies discussed in the next section.

Several process setups are associated with all CNC machining centers. (Typically, the term machining center is used to describe a generic machine tool capable of a variety of machine operations - e.g. milling, turning, drilling, etc.) First, are the numerical instructions themselves. These instructions carry all information concerning the machining operation including speeds, feeds, depths of cut, and tool changes. Second, all machining operations require cutting tool setups. Most machining centers offer automatic tool changers (ATCs) which can reduce tool setup times to as little as a few seconds. ATCs maneuver tools for mounting on the end of the CNC spindle. Third, all machining centers must have a mechanism for loading and unloading the workpiece. Many machining centers use automatic pallet changers (APC) to reduce workpiece setup. APCs may consist of multiple pallets on a turntable so that workpiece loading and unloading can be performed while machining a workpiece on an alternate pallet. Unmanned operation of machining centers is typically limited by workpiece loading and unloading. Ultimately, robotic loading and unloading can be fed by automated guided vehicles in totally unmanned operations.

Today, many geometries can be automatically produced on a CNC machining center. However, fully automated machining has been hampered due largely to special tooling and fixturing requirements for specific part geometries. To minimize tooling setups, some milling machines used in RP applications make use of ball-nosed end mills. However, such general-purpose tooling is not a “magic pill” which work for all part geometries. Ball-nosed end mills require tradeoffs between dimensional accuracy, surface finish, and material removal rate. Overall, the surface finish and dimensional tolerance produced by a milling machine with a standard end mill on a quadrate surface may be very different from the finish and tolerance produced with a general-purpose ball-nosed end mill for RP applications.

In addition, because machining operations require cutting tools, the process is prone to tool wear and tool failure. Many machining centers now use adaptive control (AC) systems to prevent the work stoppages associated with tool failure. Most AC systems monitor parameters such as spindle deflection, horsepower, or cutting forces in an effort to trade-off material removal rates and tool wear. However, much research has been conducted to integrate various sensors into AC systems for the purposes of optimizing other parameters such as tool wear and surface finish. Most machining centers have some mechanism for recognizing and responding to tool failure as well.

Like cutting tools, part-specific workholding devices may also be required in RP machining. These devices are required to secure the workpiece during processing against forces on the order of several thousand newtons. If the part geometry is so complex that general clamps cannot seat properly, specific fixturing must be fabricated with associated lead times and expense. For RP applications, this time and expense can be critical.

Table 2.1 summarizes some basic process parameters for various machining processes [DEGA88], [KALP92]. Included in the table are workpiece sizes, material

Table 2.1. Summary of some machining processes.

| Machine | Typical Max. Workpiece Size cm(in.) | Typical Production Rate pcs/hour | Achievable Tolerance mm(in.) | Typical Surface Roughness mm(μ in.) |
|------------------|--|-------------------------------------|---------------------------------|---|
| Milling | 183 x 122 x 183 (72 x 48 x 72) | 1-100 | 0.0125 (0.0005) | 1.6-6.3 (63-250) |
| Engine Lathe | 200 dia. x 185 (78 x 73) | 1-10 | 0.025 (0.001) | 3.2-6.3 (125-250) |
| Machining Center | 91 x 30 x 46 (36 x 12 x 18) | 10-120 | 0.0025 (0.0001) | 1.6-6.3 (63-250) |

removal rates, tolerances, and surface roughness generated by the various machine tools. However, these figures should be treated with caution due to the wide variety of machines and machine operators available. A typical cost for the machining center featured below would be on the order of US\$300,000.

Subtractive processes like those described above have many advantages over the newer additive processes described below. Unlike the additive processes, machining processes can fabricate in many different kinds of engineering materials. Possibly most important is the order of magnitude improvements in production rate held by subtractive processes. In addition, machine tools tend to be much more accurate and provide generally better surface finish though great strides have been made by additive processes in this area. At the same time, machine tools require greater energy requirements, less geometric complexity, and more attended operation than additive processes.

2.2.1.2. Additive

While progress has been made toward the goal of freeform machining, certain geometries cannot be produced on a CNC machining center. In addition, it has been suggested that fully flexible machining automation can be hampered by special tooling and fixturing requirements which can significantly increase development times and costs. Solid freeform fabrication (SFF) is a term which has been used to describe collectively the emerging suite of additive RP technologies designed to overcome these deficiencies.

SFF processing technologies aim to rapidly "build-up" parts without the use of specialized tooling, thereby eliminating costly delays and expensive specialized tools. Each of these technologies employ the use of solid modeling techniques and computer control technologies to directly deliver energy to material layers for the purposes of selective, localized manipulation. In all cases, a solid model of the part is created on a CAD workstation and dissected into many thin cross-sections with a typical thickness of 75 to 250 micrometers. These cross-sections are then used to deliver energy to each layer of material.

Figure 2.1 shows a generic coordinate system which will be helpful in the following discussion on additive RP technology. This figure shows a generic energy source being scanned over the surface of a material in an additive process. Notice that the x- and y-axes form a plane parallel with the material surface with the x-axis being congruent with the direction of the scan. Notice also that the z-axis is perpendicular to the scan, across the laminated layers of material. These axes are important for indicating various material properties such as yield strength and surface texture. In general, material properties are anisotropic and tend to degrade along the z-axis.

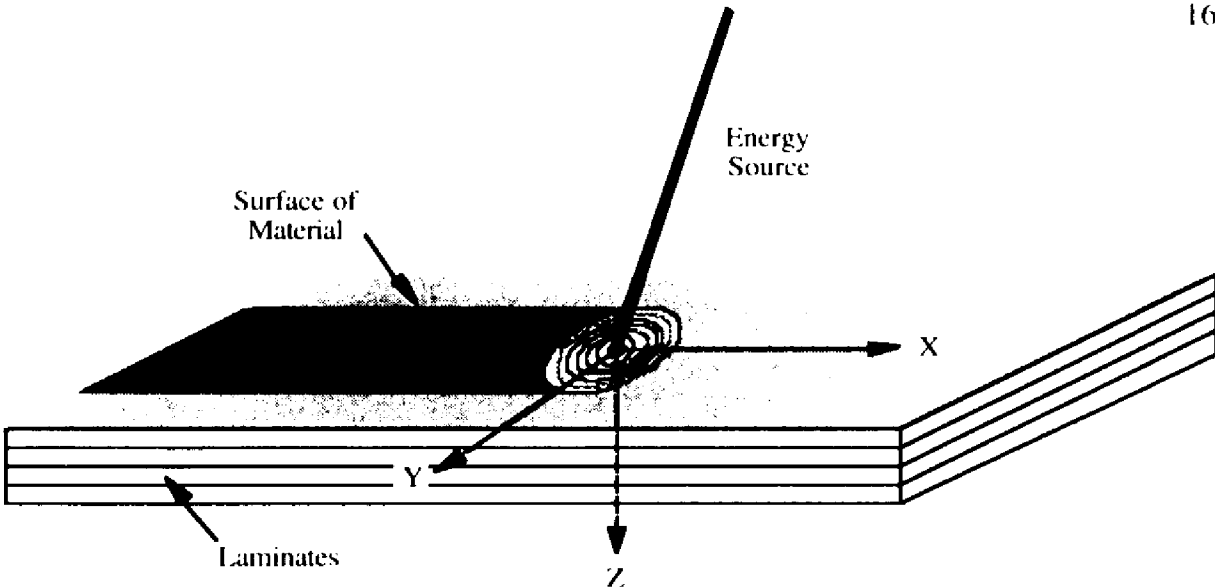


Figure 2.1 Coordinate system for additive RP technologies.

Over 40 different types of additive RP technologies have been identified in various stages of development [BURN93], [JACO92], [KOCH93], [PACH93]. The ultimate goal of each of these processes is the production of complex, fully-dense mechanical parts with minimal lead time. Each of these processes has its own unique set of advantages and limitations. The most advanced commercial technologies are summarized below.

2.2.1.2.1. StereoLithography

StereoLithography (SLA) employs ultra-violet (UV) radiation in the form of a computer-controlled laser to selectively cure a photopolymer. A diagram of the process built by 3D systems is shown in Figure 2.2.

Specifically, like all additive RP processes, the SLA process starts by converting a 3D solid model object into a series of very thin cross-sections or slices, as though the object were cut into multiple layers. Then, using the data from each cross-section, it sequentially traces each cross-section onto the surface of liquid photopolymer with a laser-generated UV light beam. The small but intense spot of UV light causes the polymer to locally harden where it is scanned. To build-up a part layer-by-layer, an elevator is placed

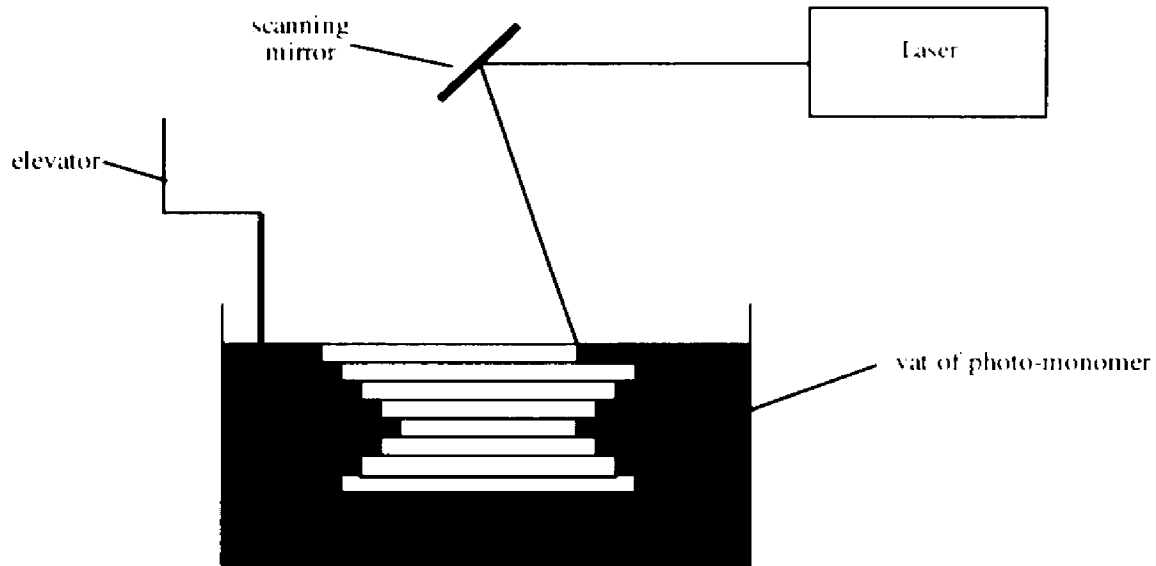


Figure 2.2. Schematic of SLA process.

within a vat of liquid photopolymer. Prior to scanning each cross-section, the elevator is lowered one layer thickness into the vat and a mechanical carriage is used to spread a uniform layer of photopolymer over the elevator surface. These steps are repeated over and over again until the desired 3D geometry is complete. Once complete, the part must be post-cured in a ultraviolet flood oven to achieve full polymerization and, consequently, better material properties.

SLA is a proven technology with the largest user base of all RP systems currently available. In 1992, about 90% of all RP systems worldwide were SLA units designed, developed, tested, and sold by 3D Systems, Inc. [JACO92]. Over 275 are currently in use around the world [BURN93]. Advantages afforded by this large user base include greater product support and development. 3D Systems currently operates five sales offices in the U.S. as well as four wholly-owned subsidiaries in Europe and Asia. Throughout the world, more RP applications and process research have been carried out on SLA machines than any other.

In 1992, another 5% of the RP systems worldwide were derivatives of the SLA technology described above, developed by companies such as Sony and CMET (Computer Modeling and Engineering Company) in Japan, EOS (Electro Optical Systems) in Germany, and Quadrax in the US [JACO92]. Since 1992, at least two other SLA-like (or SL) technologies have become commercially available from companies like Teijin Seiki in Japan and Laser 3D in France. Other technologies developed by Cubital in Israel and Light Sculpting in the US use a masked-lamp approach to selective photopolymerization. All of these methods build polymer objects in a vat of liquid resin with the exception of the Solid Ground Curing (SGC) process developed by Cubital. (The SGC process is described in more detail in the next section.)

Figure 2.3 shows some of the different layering methods adopted by these various photopolymer-based RP processes [BURN93]. Each of these methods has its own set of technological advantages and issues. Most photopolymer-based RP systems use the *descending platform* method. This method can benefit from lower viscosity resins as this enables faster layering and promotes better flatness of liquid layers during build with faster drainage of resin from objects after build. However, low viscosity resins are more sensitive to vibration and, thus, less desirable for most installations. Also, the low molecular weights of most low viscosity resins result in weaker solid materials due to the fewer number of cross-links produced among the short oligomers used to reduce viscosity [BURN93].

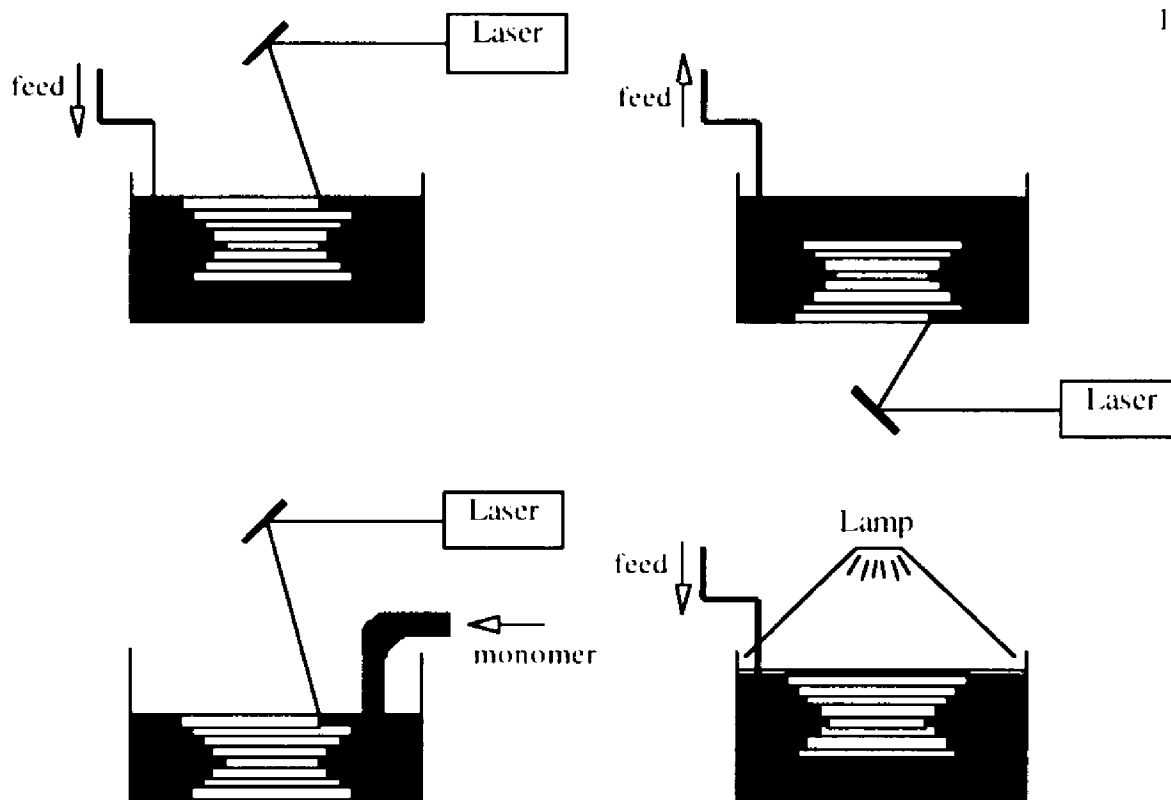


Figure 2.3. Schematic of the different SL methods including: (Top left) Descending platform; (Top right) Ascending suspension; (Bottom left) Ascending surface; (Bottom right) Masked-lamp descending platform.

Alternatives to this approach include the *ascending suspension* method used by Mitsui in their developmental COLAMM process and the *masked-lamp descending platform* method implemented by Light Sculpting. In both of these processes, solidification is produced in contact with a transparent window. In the COLAMM process, the part is built from the top cross-section, down. As the elevator is raised to scan each successive cross-section, resin flows between the transparent window and the suspension substrate. In contrast, the photopolymer-based process developed by Light Sculpting simply creates photo-masks for each layer which rest upon a transparent material that is in contact with the resin surface. The advantages of these processes lie in potentially higher throughputs and shorter layering setups between layers. These methods are also much less sensitive to vibration since the polymer surface is formed by contact with a solid surface, thus, making

lower viscosity photopolymers desirable. The final layering method, the *ascending surface* method, was used by the Quadrax Mark 1000 process before that process was discontinued in 1992.

Advantages of SL technology include high accuracy and good surface finish. SL processes tend to offer the best dimensional accuracies of all additive RP processes available with repeatable accuracies down to 0.03% over a 60 mm dimension [KRUT91]. As can be expected, accuracies worsen over longer dimensions with typical values for accuracy between 0.1% and 0.5%. Surface finishes below 16 μin (0.4 μm) on surfaces perpendicular to the beam axis have been reported by 3D Systems using SLA technology [JACO94].

A major disadvantage of all SL processes involves the use of expensive photopolymers which are often highly toxic. Current prices for a typical photopolymer resin run 100 to 200 US\$/kg. Further, many of the liquid resins used are acrylics which can cause skin irritation or other toxic effects if handled improperly. Some resins also contain suspected carcinogens [BURN93]. Thus, safety precautions must be taken when handling these raw materials which generally eliminates the accessibility of SL technology within typical office environments. Because of their toxicity, it is expected that stiffer environmental requirements in the future may pose further difficulties for photopolymer-based fabrication.

Another disadvantage of these processes involves the need for supports in processing objects, negating some of the advantages of tool-less production. In addition to wasting material, supports must be removed after processing. In most SL processes, further post-processing is required to fully cure the part in an ultraviolet flood oven. (Although, one of the SL vendors, CMET, claims that their process uses photopolymers which do not require post-curing.) Such post-processing is another disadvantage of the SL technologies.

In the past, many SL resins had other less desirable properties. Early in their development, many acrylate monomers were prone to much volumetric shrinkage resulting in curling and poor dimensional accuracies. These resins also produced very brittle polymers. More recently, great strides have been made in reducing the shrinkage and brittleness of photopolymer resins. Several types of SL resins are available each with a unique application. Photopolymers have been designed strictly for low shrinkage for prototyping applications, increased toughness for functional testing applications, and low melting temperature for investment casting applications. Some resins have much lower viscosity capable of providing improved surface textures without adding volatility.

In comparing the various SL technologies with one another, several processes stand out. In 1994 Chrysler sponsored an RP technology benchmarking study, evaluating fifteen different RP processes on the basis of part cost and processing time for a small speedometer adaptor [SCHM94]. Of particular interest was the comparison of the nine SL vendors in the study. The SL processes developed by Laser 3D in France and EOS in Germany had processing times up to 5 times faster than those of other SL technologies. In addition, it was found that the costs for outsourcing work to the vendors of these processes were among the lowest of any currently available RP technology. A physical inspection of the parts produced by Chrysler during the benchmarking study showed that these advantages were provided without a loss of surface texture quality.

The advantages provided by the EOS process have been attributed in part to a faster laser scanning speed. This is not surprising since EOS is a spin-off company of General Scanning, a manufacturer of galvanometers such as those used in SL technology. Other reasons expected for the improvements in speed include a proprietary layering technique that is claimed to reduce non-scanning time to 20 seconds per layer [BURN93].

A peculiarity of the RP process provided by Laser 3D is that the process can only be accessed through a service contract directly with Laser 3D while most other processes,

including the Stereos, are commercially available for purchase. It is expected that the limited accessibility of the Laser 3D process is due in part to protection of proprietary process innovation. By considering advances available through the EOS process, some speculation can be made concerning the areas of improvement on the Laser 3D process.

2.2.1.2.2. Solid Ground Curing

Solid ground curing (SGC) cures layer upon layer of photopolymer with the use of a photomask and a high-intensity UV lamp. The process is similar in nature to the Light Sculpting process eluded to in the previous section. However, the implementation is much different; not requiring the fabrication of supports for certain geometries and, thus, warrants an explanation of its own.

A diagram of the SGC process is shown in Figure 2.4. Like other SL technology, the SGC process gets its operating data from CAM software used to slice the original CAD solid model of the part into thin cross-sections. Fabrication of a layer begins with the development of a photomask through a process known as *ionography*. This process, shown as the *mask plotter cycle*, is similar to Xerography, used in photocopiers and laser printers. A cross-sectional pattern of static charge is put down on a glass plate and covered with electrostatically-attracted black powder, or toner. The resulting photomask is used to selectively expose a layer of photopolymer. Subsequently, the photomask is erased and recycled by removing the charge and powder from the glass plate.

Once a layer of photopolymer has been exposed under the photomask, it is then further processed within a *model grower cycle*. First, any unexposed, excess resin is removed from the layer. Then, a layer of liquid wax is applied and solidified to fill-in any voids left by removing the unexposed resin. Finally, the entire layer of wax and photopolymer is milled down to a specific thickness by a face milling operation.

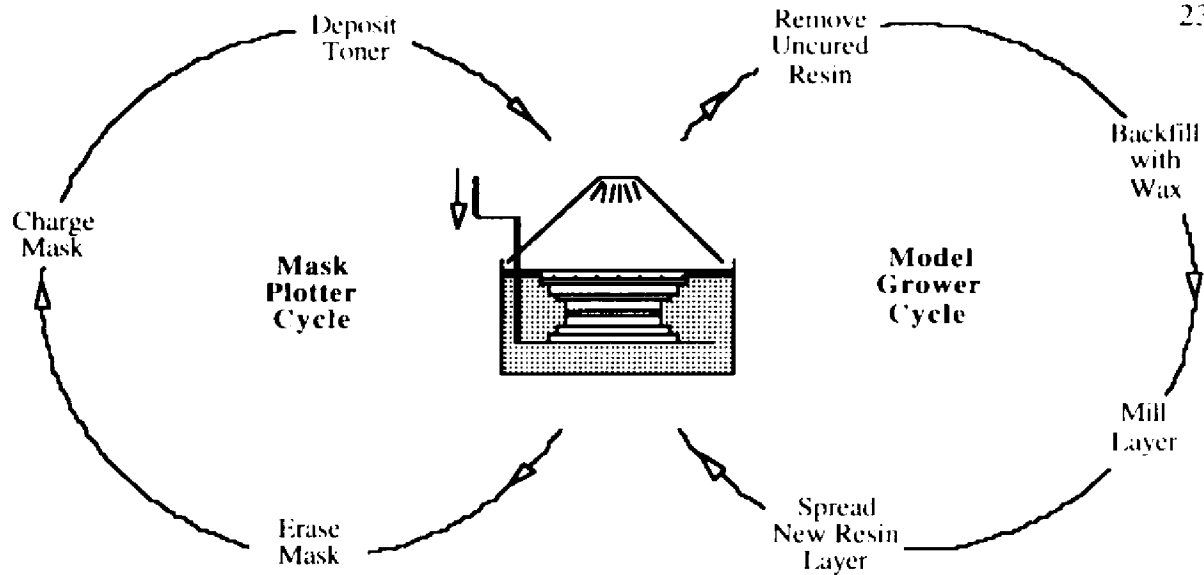


Figure 2.4. Schematic of SGC process.

In addition to producing a precise, uniform layer thickness, the milling operation is also performed to promote adhesion between layers by roughening up the surface. Adhesion between layers is a more difficult problem within masked-lamp RP processes the difference being that the photopolymer is not exposed to oxygen inhibition within a masked-lamp processes. Within open-air, descending-platform, SL processes, oxygen from the air inhibits initiation of the polymerization process within a thin surface layer of the exposed photopolymer. This thin liquid layer aids in the adhesion between model layers. In an enclosed, masked-lamp process, the layers of photopolymer are not exposed to air and, thus, do not retain this thin layer of unpolymerized resin. As a result, a method such as milling is needed for improving the adhesion between layers.

Like other SL technologies, dimensional accuracies tend to be very good with the SGC process. Claimed accuracy for the process is 0.1% up to 0.02 inches (0.05 cm) [LEWA91]. Also, the use of photomasking technology provides the SGC process with a potential for fast processing times. Once a mask is developed, layers can be

photopolymerized within 3 seconds. However, because of the number of steps involved, the process, as implemented, requires around one minute per layer [BACK91].

While the process is not the fastest photopolymer-based process on the market, it is quite fast and does have a relatively large throughput. This is because the process can fabricate parts in much larger batches than many of the other processes. In the SGC process, all of the work envelope can be dedicated to the fabrication of parts. In other SL processes, much of the work envelope is consumed by supports needed to reinforce parts during fabrication.

One extraordinary feature of the SGC process is its ability to fabricate "pre-assembled" structures. Pre-assembled structures are multiple piece assemblies which are fabricated already assembled. For example, one company has used this feature to prototype a universal joint, complete with moving parts. As a result, no assembly was required and since the part was fabricated as one piece, dimensional tolerances were less of an issue. This ability to fabricate pre-assembled structures is unique among existing mechanical part fabrication technologies.

Disadvantages of the machine include that it is the largest and most expensive to buy at roughly US\$550,000 in 1994 prices. As a machine, the process weighs over 4 tons and is more than 10 feet in length. Further, because of the complexity of the process, users have been plagued by unreliable performance. As of early 1993, customers were being told to expect about 25 to 30 percent downtime [BURN93]. In addition, many users have experienced difficulties with the removal of wax especially from smaller features and crevices such as those found in pre-assembled items.

2.2.1.2.3. Selective Laser Sintering

The Selective Laser Sintering (SLS) process relies on a laser beam to fuse selected areas of loosely compacted powder. An illustration of the process is given in Figure 2.5. Unlike the SL technologies which fabricate objects within a vat of liquid photopolymer, the SLS process operates on a cylinder of powder. A piston within the cylinder acts as an elevator to vertically position the powder bed. As before, CAM data for the operation is prepared by virtual slicing of a CAD solid model.

Since the process is carried out at elevated temperature, the atmosphere within the process chamber is important. For polymeric powders, the chamber is typically filled with nitrogen and heated to the final operating temperature prior to build. To begin a build cycle, the piston is lowered a layer thickness and powder is spread evenly over its surface by a mechanical roller. Like the SL technology, a laser is scanned over the surface of the

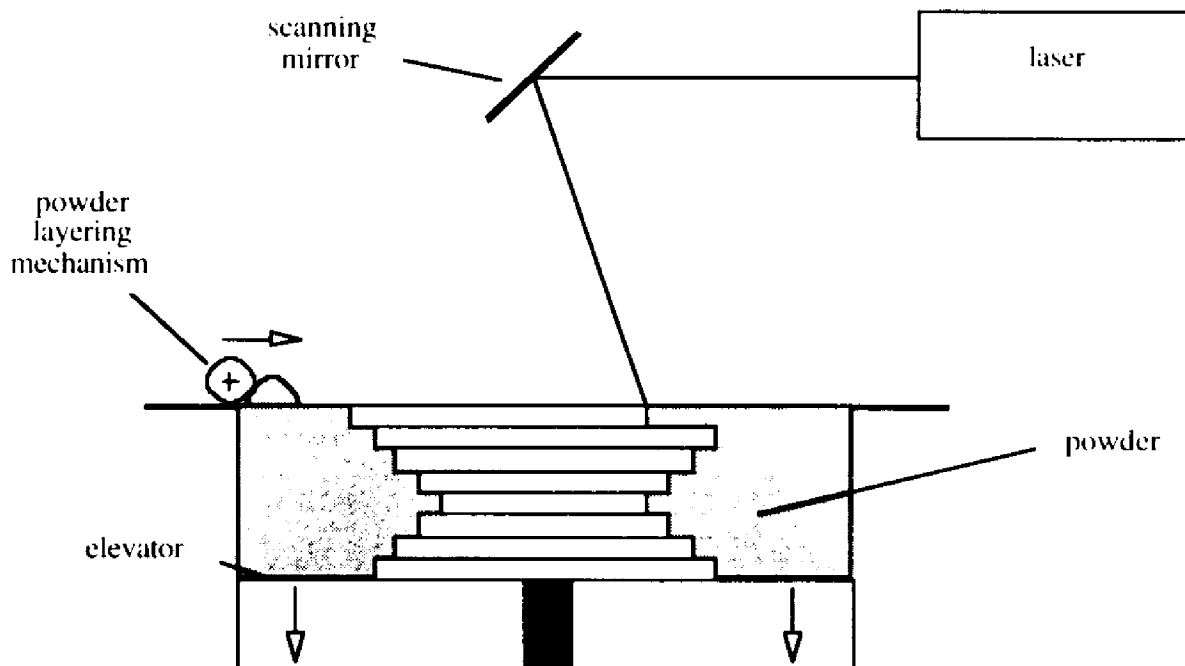


Figure 2.5. Schematic of SLS process.

powder substrate in the desired pattern. Where the laser contacts the powder, a small region of the powder is heated causing it to fuse with surrounding powder. After a cross-section has been scanned, the piston is lowered again in a manner similar to the descending platform method used by many SL processes. When the part is completed, it is extracted from the powder cylinder and excess powder is removed. Excess powder within the cylinder can be reused.

Because of the short durations of localized heating during SLS processing, the primary mechanisms for binding together and densifying particles are *fusion* based on melting and resolidification and *sintering* based on viscous flow [BOUR92]. Sintering is the preferred method for binding together thermoplastic powders due to their low activation energies for viscous flow. Contrary to popular belief, sintering of metal and ceramic powders does not actually occur under the laser beam in the SLS process. Sintering is a process in which solid particles fuse together at temperatures just below the melting point of a material based on the accelerated atomic transport of matter. Because of the high viscosity of metals and ceramics even at temperatures approaching the melting point, sintering must be conducted over prolonged periods of time to achieve densification within metals and ceramics. Thus, actual metal and ceramic sintering requires a much longer period of time than experienced under the laser beam during SLS processing.

While sintering is not actually experienced during the SLS processing of metals or ceramics, oven sintering can be used in the post-processing of SLS metal and ceramic parts. Because a metal or ceramic powder does not have enough time to sinter under the laser beam, an alternate method is needed to consolidate the particulates. As in other powder metallurgy techniques, the SLS process can be used to *bind* together powder particulates into a net shape which can then be densified or infiltrated within a sintering furnace. In the SLS process, the method for doing this involves the use of *polymer-coated* metal and ceramic powders. That is, the metal and ceramic powders used within the SLS

process are actually coated with a very thin layer of polymer binder. Thus, where the laser contacts the powder, the polymer coating *binds* the powder particulates together. When finished, the so-called *green part* is removed from the powder cylinder and placed into a sintering furnace for densification. Once in the furnace, the polymer binder is first evaporated or wicked away leaving a porous metal or ceramic material behind. Upon further heating at a higher temperature, the metal or ceramic is eventually densified via sintering.

Possibly the greatest advantage of the SLS process is that it permits fabrication using a variety of engineering materials. DTM, the manufacturer of the SLS process, has become the first vendor to offer direct fabrication of metal tooling for injection molding with the introduction of RapidTool™ in mid-1994. Early metals available for rapid tooling fabrication include tool steel infiltrated with copper for full densification during sintering. In addition, a variety of polymeric materials are available for the process including nylon, investment casting wax, and polycarbonate. Nylon provides good surface texture and dimensional accuracy while the polycarbonate has better mechanical properties. Further research is being conducted by DTM for application of the SLS process to ceramics and composites.

Like the SGC process, another major advantage of the SLS process is that it does not require special support structures for certain geometries. In the SLS process, the excess powder acts as a “natural” support. Thus, time and materials are not wasted in building and removing support structures. And, as mentioned above, excess powder from one build can be used in another build further decreasing material waste. Further, another advantage of the SLS process over SL technologies is that the SLS process does not require any post-curing for polymeric materials.

Because of the need to significantly raise the temperature of the material, the SLS process requires a much more powerful laser than the SL processes. The SLS process

uses a CO₂ laser which is about a 1000 times more powerful than the HeCd lasers used on the SLA-250. However, the CO₂ laser is also about 1000 times more efficient and subsequently any difference in power consumption is minimal [JACO92]. In addition, because of the mechanisms involved, the SLS process tends to have a slower scan rate than SL processes on the order of 100 cm/s [BOUR92]. Overall, however, the SLS process has an average throughput when compared with other additive RP processes [SCHM94].

Early in the development of the SLS process, DTM incurred difficulties with high equipment costs, poor dimensional control, poor surface finish, and poor edge definition [BOUR92], [MARC90A]. Initially, the SLS process stood out as one of the higher price processes, though, by 1994, prices had dropped to US\$289,000 per machine. Problems with dimensional control and surface finish have improved with many of the problems stemming from the speed of localized cooling after scanning [BOUR92], [MARC90B]. To minimize the effect of localized cooling, it has been found advantageous to increase the total powder system temperature, requiring only a relatively small increment in temperature to promote local consolidation. In particular, the surface finish and dimensional accuracy of metal parts have improved dramatically over the past year with the optimization of processing parameters such as powder size, distribution, and binder content. Current estimates for dimensional accuracy are in the 0.005 inch (0.0125 cm) range though this can vary widely from material to material.

2.2.1.2.4. Fused Deposition Modeling

Fused deposition modeling (FDM) produces laminated three-dimensional objects through robotically guided extrusion. A schematic of the process is shown in Figure 2.6. A spool of thermoplastic filament is unwound and fed through a robotic extruding head. The extruding head melts the thermoplastic which bonds with the layer below. As a whole, the process resembles a pen plotter except that the plots are three-dimensional.

The build cycle for the FDM process is much simpler than in the prior additive processes. As a result, the FDM process has the advantages of being compact and low-cost; ideal for application in a design engineering office environment. As of early 1994, Stratasys, the manufacturer of the FDM process, had three units with prices well under US\$100,000. As shown below, FDM units are among the lowest equipment cost per unit working envelope available. The footprint for the smallest machine is about 0.6 meter²

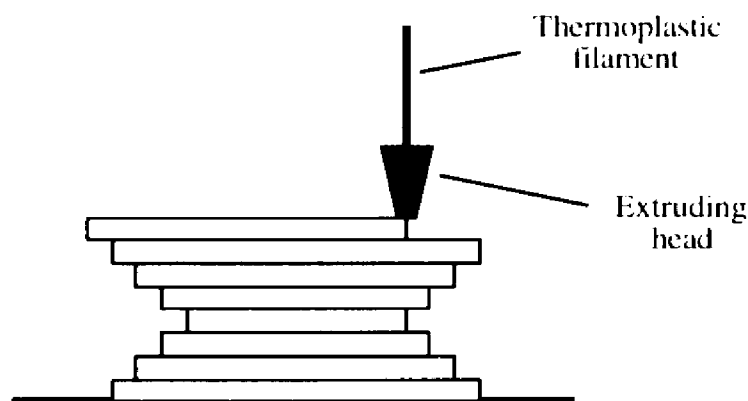


Figure 2.6. Schematic of FDM process.

weighing less about 250 lbs (≈ 114 kg); close to the size of a desktop printer. Stratasys has plans to further reduce its size and price in pursuit of capturing a large share of the anticipated desktop manufacturing market.

As a desktop unit, the target application for the FDM process is the production of 3D shapes for visualizing designs. Consequently, many of the design features are different for the FDM machines. For example, they use materials which are non-toxic; a requirement within office environments. Also, the process does not require venting or post-processing which would require more office space.

Currently the process is capable of fabricating in machinable wax, investment casting wax, nylon, and ABS. While non-toxic, most of the FDM materials have poor

mechanical properties; wax materials having worse properties than the other thermoplastic materials. Further, the surface finish of FDM parts tend to be the poorest and the process is considered to be slow. While the parts fabricated by the process do not require post-processing, the build rate of the process is slowest among the additive processes described in this section. Also, the build envelopes of the FDM machines are among the smallest of the additive processes reviewed. Finally, contrary to popular belief, the material cost of the FDM filaments are among the highest cost per unit volume.

2.2.1.2.5. Three-Dimensional Printing

Three-dimensional printing (3DP) uses an ink-jet mechanism to control a stream of binder droplets used to locally consolidate areas within a powder metal or ceramic substrate. A diagram of the process is shown in Figure 2.7. Like the SLS process described above, the 3DP process begins by compacting a thin layer of powder for processing. Next an ink jet mechanism is raster scanned over the surface of the powder, depositing droplets of molten polymer into the powder substrate. In the substrate, the droplets solidify binding together local powder particles. Like other processes, the raster scan is controlled by the CAM data generated by slicing the original CAD solid model.

The 3DP process is similar to the SLS process in that the resulting structures require post-processing in a sintering furnace. The *green* structures produced by the 3DP process consist of metal or ceramic powder particles bound together by an organic compound. Further processing of this green part is required to achieve higher material densities and better mechanical properties. Like the SLS process, this requires driving out the organic binder and consolidating the remaining powder in a sintering furnace.

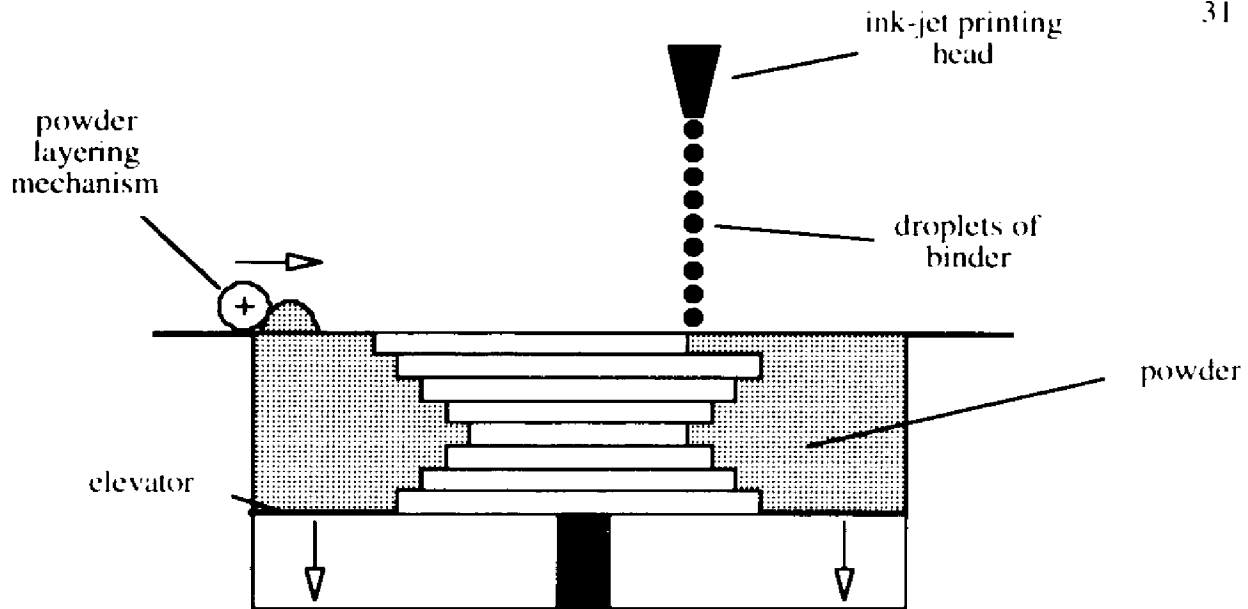


Figure 2.7. Schematic of 3DP process.

Most work done to date with the 3DP process has involved the fabrication of low-density ceramic structures, especially investment casting shells. This is because MIT, the developer of the 3DP process, has chosen to market the 3DP technology through application-specific channels. The first company licensed to sell the 3DP technology is Soligen, Inc., a start-up company located in Northridge, California. Essentially, Soligen manufactures a system which is used to implement their method for investment casting called Direct Shell Production Casting (DSPC). The DSPC process is based on the 3DP process technology. The process fabricates investment casting shell directly from a CAD solid model without the use of patterns. As expected, Soligen's major market is investment casting foundries.

Because MIT has chosen to market its technology in a different way than the other processes described, very little data is available concerning the capabilities of the 3DP process. Soligen and MIT have purposely avoided attempts to benchmark their process against others because they believe that their process is significantly different from other additive processes.

Potential advantages of the 3DP technology include its ability to fabricate in a variety of engineering materials. In addition, this process currently has the best potential for selectively manipulating the micro- and milli-structure of a three-dimensional object. Potential benefits of this micro-constructive feature includes selective material properties throughout the microstructure of the fabricated object. Based on the literature, the 3DP process, as marketed by Soligen, has a reasonably small work envelope (12 x 12 x 12 in. or 30.5 x 30.5 x 30.5 cm), poor surface finish (472 μ in. or 12 μ m), moderate dimensional accuracy (0.005 in. or 0.0127 cm), and a fast build rate (90 in.³ or 1475 cm³) relative to the other additive technologies [UZIE93], [SACH92]. As of late 1993, the Soligen machine was selling for around US\$300,000 though only four beta units had been installed as late as January 1995.

2.2.1.3. Hybrid

Some RP process technologies don't fall neatly into either the additive or subtractive categories outlined above. Because these processes typically use a combination of additive, subtractive, and even formative (in the case of sheet metal bending) process steps, these technologies are considered hybrid. Several hybrid RP processes are described below.

2.2.1.3.1. Laminated Object Manufacturing

Laminated object manufacturing (LOM) employs a laser to cut patterns in multiple layers of polypropylene-backed paper which are then stacked to produce the desired shape. In this sense, the process involves both an additive feature, in that it stacks material layers, and a subtractive feature, in that it cuts the layered material, and so is considered a hybrid process.

A diagram of the process is shown in Figure 2.8. Specifically, the process involves several steps. First, a fresh sheet of paper is rolled onto the working surface. Next, a heated roller is rolled over the surface of the paper to bond the paper sheet to the layer below it. Once the paper sheet has been bonded to the substrate below, the laser is guided in a “cookie-cutter” pattern to “cut-out” the 2D cross-section assigned to that layer. These steps are repeated over and over again to fabricate the proper 3D geometry.

One unique characteristic of the LOM process is the method for extracting the design after fabrication. Measures must be taken to remove the excess paper mass which accumulates around the periphery of the 3D object during the build. Removal of the excess material is handled by drawing a consistent set of cross-hatches in the excess material at each layer. Over many layers, these cross-hatches form the boundaries of 3D blocks which can be readily removed from around the finished prototype. Unfortunately, like the subtractive processes mentioned before, this can result in a great deal of material waste.

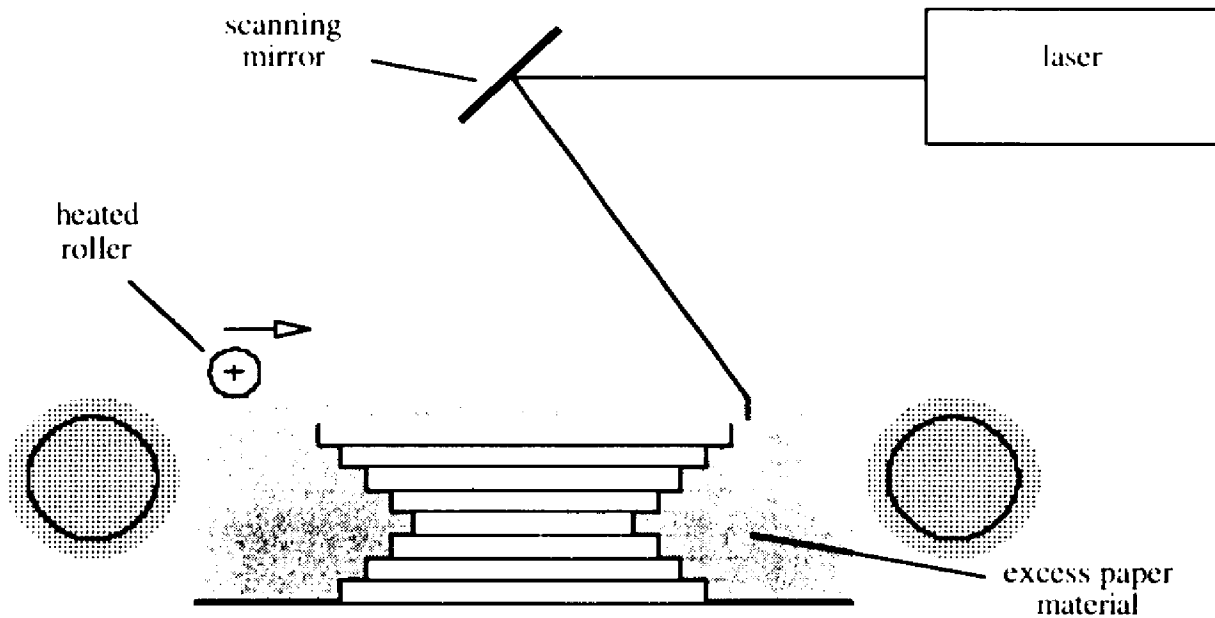


Figure 2.8. Schematic of LOM process.

Like the SLS process described above, a major advantage of the LOM process is that it does not require the fabrication of any specialized supports to be removed after the build. The excess solid material provides a “natural” support of the object while it is being fabricated. Thus, complex cantilevered geometries can be fabricated as easy as any other structure. This makes the LOM process very flexible in terms of its ability to process complex geometries.

However, unlike the SLS process, the LOM process is much more reasonably priced. Quite possibly for this reason, Helisys has chosen to distribute the LOM process through existing job shops and major manufacturers directly rather than organizing independent service bureaus of its own. In addition, materials for the LOM process are much more reasonably priced than the powder and liquid-based SFF processes described above.

A major strength of the LOM process is the diversity of materials to which it can be applied. In the process described above, the properties of the finished material would be similar to those of wood. This is a unique capability among the other major RP equipment vendors. This can be advantageous for mold-makers and benching people who are used to working with wood patterns or for model-makers in wood-working shops. However, in addition to its ability to fabricate in paper, the LOM process currently can fabricate in polyester and has the potential to fabricate in other sheet materials. For example, recent research has been conducted to use the LOM process to fabricate high-density ceramic parts [GRIF94]. A comparison of material properties of ceramic bars fabricated by conventional powder-pressing and the LOM process is shown in Table 2.2.

Table 2.2. Material properties of pressed and LOM-fabricated alumina bars.

| Method | Direction of Test | Flexure Strength MPa | Vickers Hardness GPa | Fracture Toughness MPa*m ^{1/2} | Green Density g/cm ³ | Sintered Density g/cm ³ | Shrinkage % |
|------------------|-------------------|----------------------|----------------------|---|---------------------------------|------------------------------------|-------------|
| LOM | Parallel | 314 | 20.2 | 4.3 | 2.55 | 3.88 | 14.1 |
| | Perpendicular | 311 | 20.1 | 3.9 | | | |
| Pressed | Parallel | 336 | 21.8 | 4.0 | 2.34 | 3.89 | 15.8 |
| | Perpendicular | 325 | 19.8 | 3.7 | | | |
| Commercial Grade | | 379 | 14.1 | 4-5 | | | |

Conceptually, some claim has been made that the sheet-based LOM process has inherent advantages over the previously mentioned powder or liquid-based SFF processes [FEYG89]. For example, it is suggested that the process should be significantly faster because only the surface of the object is fabricated though some of this time savings is lost to the need for cross-hatching. However, in benchmarking studies, the LOM process consistently places in the back of the pack concerning build speed. Some of these discrepancies may be accounted for in that speed advantages are more pronounced for the LOM process as the part volume increases.

Further, since the material does not go through a phase change (e.g. liquid to solid), residual stresses are reduced resulting in less warpage and better dimensional stability. The process cannot currently achieve tolerances much better than about 0.01 in. (0.0254 cm) leaving considerable room for improvement. However, since the paper material does not undergo a phase change, the LOM process can hold this tolerance over the entire work envelope providing possibly the best dimensional control at larger scales.

2.2.1.3.2. Other Hybrid Processes

Over the past 15 years, several automated sheet metal shearing and bending processes have been developed [BURN93]. These processes take stacks of sheet metal and convert them into desk drawers, refrigerator body panels, or heating and ventilation

ductwork. While these processes are not used for RP applications, they exemplify the ultimate goal of the RP industry: rapid design-to-manufacturing transition.

One process was developed by Salvagnini in the late 1970's and is targeted for factory production of sheet metal products. Claimed positioning accuracies for bending are 0.1 mm (0.004 in.) with a 1° bending angle accuracy. Average throughput for this process is less than one minute with the average changeover time less than two minutes. The shearing process contains more than 112 punching tools available for immediate changeover. Overall, the system can be installed in modules and with specific modules selling for more than a million US dollars.

More recently, another process has been developed in the US by Iowa Precision. This process is targeted very specifically for the fabrication of ductwork used in the heating, ventilation, and air conditioning industry. Claimed accuracies for the shearing operations in the Iowa Precision process are 0.5 mm (0.02 in.). The system is configurable and sells for several hundred thousand US dollars.

2.2.2. Applications

Many applications for RP systems have evolved in the ten years since the first SLA system was introduced. Early on the RP industry was typified by SLA models which were brittle and rather rough with mediocre dimensional control at best. Consequently, the original SLA models were used mainly for visualization and verification of product designs. This capability enabled product designers to uncover basic errors in design which previously might have been overlooked when reviewing abstract two-dimensional drawings. Since then, many new RP processes have been introduced and along with them, many improvements have been made in the dimensional accuracies, surface finishes, and material properties associated with RP technologies. Below a few RP applications are discussed.

2.2.2.1. Functional Testing

As aforementioned, the name *rapid prototyping* better describes an application than a technology. Prototyping was the first major market addressed by RP technology. Manufacturers use prototypes for various reasons: design visualization, bid requests, and marketing demonstrations. Yet, the overriding reason for prototyping is to know whether a product is functional. As such, functional testing has become a big market for RP technology.

The use of RP technology in functional testing has been implemented at several levels. The first level involves the testing of *form*. Issues involving aesthetics and ergonomics of the product can be dealt with at this level. Most mechanical products can take advantage of RP technology at this level. The second level involves the testing of *fit*. Many designs are prototyped to check if individual design pieces fit together or to check the design-for-assembly. Automotive companies use prototypes to check the fit in cramped compartments such as the engine compartment.

Finally, RP technology can be used to test the *functionality* of the product to be developed. For example, at AMP, Inc., product developers are constantly looking for ways to prototype new connectors with mechanical properties identical to those produced in high-volume production. In dealing with customers, AMP must provide samples of finished products which are evaluated for product performance. Many times customers will not accept RP models as product verification because they are made out of different materials or have been fabricated in a different manner, both of which can alter mechanical properties of the connector. As a result, AMP is constantly looking for new ways to reduce the cost and time needed to produce end-product-quality prototypes. Other examples of functional testing using RP part include fluid flow testing of intake manifolds within the automotive industry.

2.2.2.2. Tooling

Many attempts have been made in the past five years to use RP models as patterns or molds for basic manufacturing processes. The use of RP technology in the rapid development of such mechanical tooling has become known as *rapid tooling*. Rapid tooling is an excellent application for RP technology for several reasons:

1. Mechanical tooling is critical to most manufacturing technology and, therefore, rapid tooling can be applied universally across many industries.
2. Mechanical tooling is typically a low-volume, one-of-a-kind commodity.
3. Mechanical tooling typically has an associated long leadtime and high cost and, therefore, requires a high production volume to be justified.

As a rapid source of relatively low cost yet effective tooling, RP technology has the potential to redefine manufacturing competitiveness. Future companies may be able to justify die casting, stamping, or injection molding runs of a few hundred or a few thousand in an attempt to satisfy fleeting market niches or to minimize the risks associated with product development.

Several levels of rapid tooling have begun to appear in industry. The most basic level of rapid tooling involves the use of RP models as patterns for metal casting [BACK92]. Most prevalent have been the attempts to use RP processes to produce permanent patterns for sand or plaster molds [HOWA93], [MUEL92A]. In addition, many attempts have been made to use RP models as expendable patterns using the investment casting process [SARK94]. In this process, patterns are first placed in a *flask* and surrounded by an investment mold slurry or coated with a ceramic slurry. Subsequently the slurry is hardened by heat and the pattern is then “burned-out” or melted out producing either a solid investment mold or investment *shell*. Investment casting

patterns produced on the SLA, LOM, and SGC processes have all been used in this manner [MUEL92B] , [INVE94].

Problems using SLA models as investment patterns have resulted from the volumetric expansion of the SLA epoxy model during “burn-out” resulting in the fracture of the investment shell. Solutions to this problem have been found through the application of new photopolymers and new build styles resulting in a commercial offering known as QuickCast [ARON93]. This technique builds patterns with an internal honeycomb structure which reduces the volumetric expansion during “burn-out”. After a pattern is built, the remaining liquid photopolymer is drained out leaving the internal honeycomb structure. Other problems associated with using SLA models as investment patterns include surface defects caused by the removal of supports and cracking of thin features in investment shells due to poor drainage of the QuickCast fluid after processing.

Other methods have been used for producing investment wax patterns for producing investment casting shells. In particular, SLS and FDM have been used to directly create investment wax patterns for investment casting [SARK94]. Overall, Table 2.3 provides an overview of the advantages and disadvantages of using RP parts from several different RP processes as investment-casting patterns [SARK94].

The next level of tooling involves the fabrication of prototype molds for processes like injection molding and die casting. RP patterns have been used to create rubber or epoxy molds for use in casting investment wax patterns. Prototype tooling for low temperature alloys have been created using permanent patterns produced on RP processes. In one procedure, a silicone rubber mold was initially produced using an SLA model as a pattern. This low temperature mold is then used to spin cast a pewter pattern. This pewter pattern is then used as a permanent pattern to develop a heat-cured silicone rubber mold in a vulcanizing press. The heat-cured mold can withstand temperatures on the order of 550° C and has been used to cast up to 25 zinc alloy parts [SCHA93].

Table 2.3. Comparison of RP processes for producing investment-casting patterns. 40

| Property | SLA (solid acrylic) | SLA (QuickCast) | SLS (wax) | SLS (polycarb.) | LOM (paper) | FDM (wax) | SGC (solid acrylic) |
|--|------------------------|---------------------|---------------------|---------------------|---------------------|---------------------|------------------------|
| Compatibility with investment casting | low | moderate/ good | excellent | good | moderate/ good | good/ excellent | low |
| Casting method | flask mold only | flask or shell mold | flask or shell mold | flask or shell mold | flask or shell mold | flask or shell mold | flask mold only |
| Pattern accuracy | excellent | excellent | fair | good | good | - | - |
| Thermal expansion before melt out/burn out | high | high | negligible | moderate/ low | low | negligible | high |
| Melt out/ burn out time | slow | moderate/ fast | fast | fast | slow | fast | slow |
| Residue after melt out/ burn out | moderate / high | low | none | low | high | none | moderate / high |
| Surface finish | good | good | poor | fair | fair | poor | good |

Beyond prototype molds, the next level of rapid tooling involves the indirect fabrication of permanent molds. At Ford, several procedures have been conducted in which wax or resin replicas of molds have been fabricated using an RP process and then used to investment cast a metal mold. In one particular application, a die casting mold for a metal bracket on an automobile bumper was produced in A2 tool steel using an FDM model [ABRA93]. The turnaround on the mold was in half the time (5 weeks) at less than half the quoted price (\$4000) for a mold produced by CNC machining. The final mold was considered to be production quality and was used to produce several hundred die cast parts. In another instance, a plastic injection mold for a wiper module cover was produced in A2 tool steel from an SLA model [DENT94]. Problems with the mold included poor surface finish and poor dimensional accuracy of small features. The resultant mold was used to injection mold several plastic wiper module covers which were used for water leakage testing.

Other attempts to produce metal tooling using RP technology have involved the fabrication of metal shells for engineering tooling assemblies (ETAs). As shown in Figure 2.9, ETAs are typically made up of three parts: the metal shell (i.e. the contoured mold surface), a metal frame, and a backing material. The ETA is assembled by fabricating a metal shell typically on the order of 1 cm in thickness. Processes used to fabricate these shells include electroforming or chemical vapor deposition to deposit a pure metal on a substrate (or mandrel) in the shape of the desired mold surface [SHEP93]. The resulting metal shell is then separated from the mandrel and attached to a hollow metal frame which is reinforced with a backing material such as a chemically-bonded ceramic. Thermal

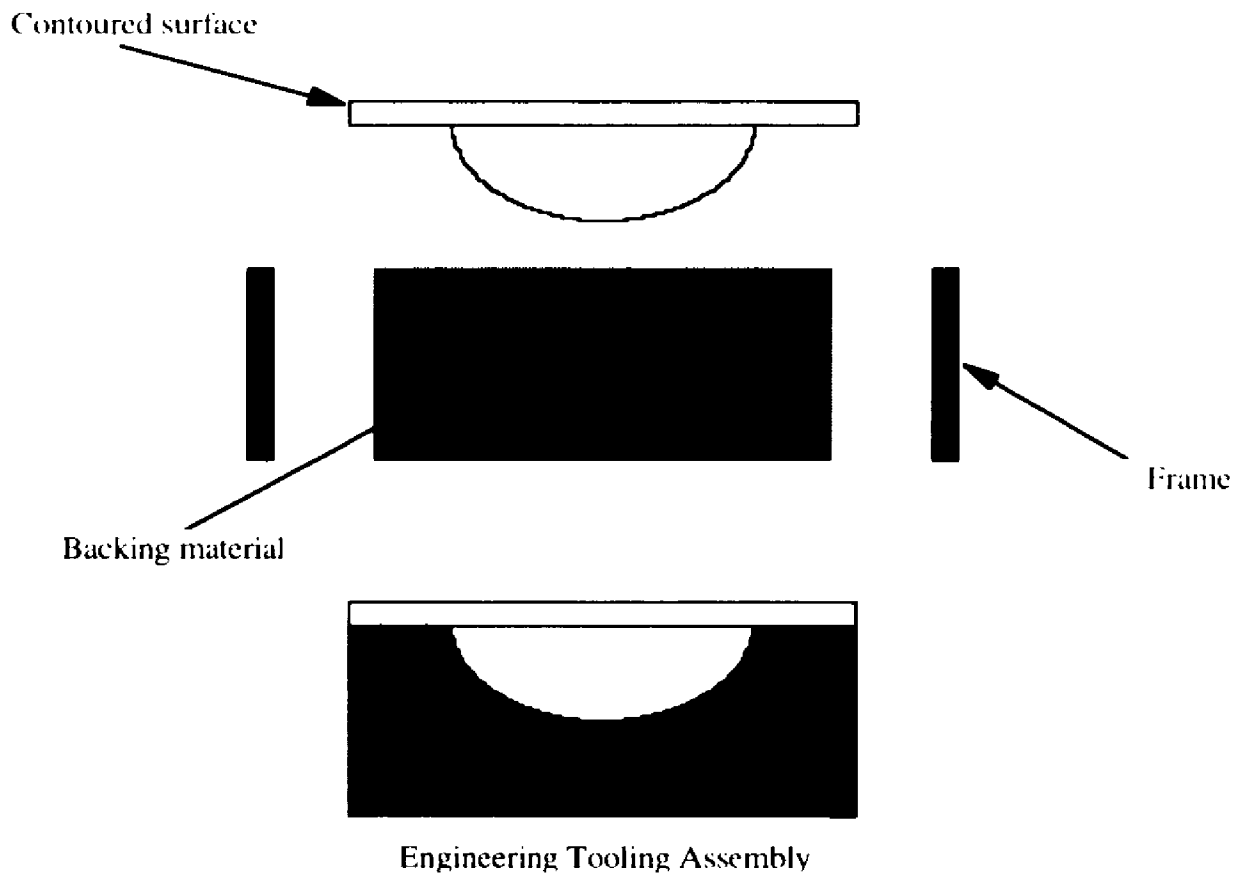


Figure 2.9. Components of an engineering tooling assembly.

spraying techniques for fabricating molds for investment wax patterns [WEIS90] have also been used to fabricate metal casting shells for ETAs. To provide an idea of the durability of these molds, production runs in excess of 5,000 have been made on a plastics compression molding machine using an ETA with a pure Ni shell backed with chemically-bonded ceramics [WISE93].

A proprietary process being marketed by KelTool, Inc. (St. Paul, MN) is available for making hard molds withstanding millions of shots for injection molding [BURN93]. The KelTool process involves molding a form over a SFF pattern, binding a fine powder metal over this form, sintering the powder, and infiltrating the porosity with a molten metal alloy. Three materials are currently available including a cobalt-chromium alloy, A6 tool steel combined with tungsten carbide, and a copper-tungsten alloy for use in electrical-discharge machining electrodes. The work envelope for the process is best suited to a 10 x 10 x 10 cm volume. Mold delivery is within four weeks after submitting a pattern.

The ultimate level of rapid tooling involves direct fabrication of permanent molds. As previously mentioned, Soligen, a start-up company in Northridge, California, is using the 3DP process developed at MIT to directly fabricate ceramic shells and cores as an alternative to shell investment casting [ASHL92]. In one experiment conducted at MIT, a 320-mesh alumina powder ranging from 25 to 50 μm in diameter and a colloidal silica binder with 30 wt% SiO_2 were 3D printed and fired in a kiln at 900°C for two hours. Results showed dimensional control around 0.05%, surface roughness around 12 μm , and a four point bending strength around 15 MPa [SACH92].

More recently, the DTM Corporation has made its RapidTool™ release on the Sinterstation 2000. The target market for the DTM RapidTool™ the direct fabrication of injection molds. In general, the system binds together metal powder in the shape of the mold. After debinding the green mold, it is infiltrated with copper to produce a fully dense mold. Typical surface roughness values produced via this process are about 6 μm (235

μm .) in the xy-plane and $12\ \mu\text{m}$ ($470\ \mu\text{m}$.) across the laminates (i.e. along the z-axis). A comparison between the various mechanical properties of a metal fabricated by the RapidTool™ system and those of standard aluminum and tool steel is shown in Table 2.4.

Table 2.4. Comparison of metal properties for DTM RapidTool™.

| PROPERTIES | UNITS SI (English) | ASTM Test Method | DTM RapidTool | 7075 T6 Aluminum | P20 Tool Steel |
|--|--|------------------------|------------------|---------------------|----------------------|
| PHYSICAL | | | | | |
| Density 23°C | g/cm^3 (lb/in ³) | D792 | 0.296 (8.23) | 0.101 | 0.282 (7.8) |
| THERMAL | | | | | |
| Thermal Conductivity 100°C (212°F) | $\text{W/m}^2\text{C}$ (BTU ft/hr ft ² °F) | E457 | 184 (107) | (80) | 29 |
| 200°C (392°F) | | | 91 (53) | | 29.5 |
| Coefficient of Thermal Expansion -51°C to 232°C | $\text{m/m/}^{\circ}\text{C}$ (in/in/°F) | E831 | 14.4 (7.99) | (12.6) | (7.0) |
| MECHANICAL | | | | | |
| Yield Strength | MPa (ksi) | E8 | 255 (37) | 503 | 990 (143) |
| Tensile Strength | MPa (ksi) | E8 | 475 (69) | 572 | 1080 (156) |
| Elongation | % | E8 | 15 | 11 | 12 |
| Young Modulus | GPa (Msi) | E8 | 210 (30) | 72 | 210 (30) |
| Hardness | R_b | E18 | 75.3 | 90 | 32 R |

2.2.2.3. Bio-Medical

The field of medicine is particularly well suited for application of RP technology. Each patient is unique. Therefore, surgeons preparing for an operation can use RP technology to turn the data from computed tomography and nuclear-magnetic resonance scans into models of the patient's internal structure. Further, bio-medical suppliers can use

RP technology to fabricate custom surgical implants and artificial limbs which fit the individual needs of the patient. In addition, bio-medical suppliers generally do not require tight tolerances, so many of the current dimensional capabilities offered by RP technology are adequate for production.

Some work has been conducted at the Northwestern University Medical School for fabricating prostheses [ROVI94]. An RP system was developed for the high-speed production of sockets for artificial limbs which were subsequently used in clinical tests. The system involves plastics extrusion onto a turntable accomplished by a small-scale, rotating screw extruder typical for industrial plastics processing. A thermoplastic homopolymer can be supplied to the extruding head in the form of either a continuous plastic rod or discrete plastic pellets. The material is melted as it is fed by the screw down the length of the extruder barrel. A constant temperature is maintained at the head of the barrel and the extruded flow is controlled by the rotation of the screw.

Results from a clinical trial have shown that a polypropylene socket has had good enough mechanical properties to withstand over three weeks of use without any observable signs of wear. Total fabrication time for the socket was 2 hours and 26 minutes. An interesting aspect of this system is that it has been optimized for a specific application. That is, most RP systems are general-purpose devices capable of producing any geometry, while this system is oriented toward building only prostheses permitting faster build rates and cheaper equipment costs.

Other organizations have focused on using RP technology in the fabrication of surgical implants. DePuy, Inc., of Warsaw, Indiana, is a leading orthopedic manufacturer which designs and manufactures replacement joints and implants for the musculoskeletal system of the human body. Implants are produced as a family in a range of sizes that can be selected at surgery to match the patient requirements, or, if desired, can be provided on a custom prescription basis. DePuy uses SLA technology to fabricate sculpted surfaces for

custom hip, knee, shoulder, ankle, elbow, and wrist implants which are used as prototype tooling masters for producing investment wax patterns. Actual projects launched at DePuy to develop new product families have used urethane tooling produced using SLA masters to generate wax patterns for investment casting. This allowed DePuy to proceed with new product sales as an extension of the development process.

2.2.2.4. Microfabrication

As mentioned above, the miniaturization of mechanical systems has begun to be of interest. A new alternative to net-shape micro-mechanical fabrication is a micro-freeform fabrication process being developed in Japan which employs StereoLithography-like technology at the micro-scale [IKUT93], [IKUT94], [TAKA93]. Advantages of this process include the ability to fabricate high-aspect-ratio, freeform geometries without specialized tooling. However, this process suffers from limited resolution resulting in parts with poor surface textures. The dimensional resolution of the process is limited by the UV wavelength of light. Also, like many micro-mechanical fabrication processes, this process suffers from a small processing capacity with current cycle times at 30 minutes for a 100 x 100 x 1000 micrometer part volume.

Other opportunities exist for RP technology at the micro-scale. One significant challenge for micro-mechanical fabrication will be the coupling of force between individual components of the system. Future micro-mechanical systems will need to consist of circuits, actuators, sensors, power sources, manipulators, end effectors, and other components integrated onto a single chip. While much progress has been made in fabricating integrated circuits with on-chip mechanical sensors or in fabricating individual actuators, little success has been made in fabricating integrated micro-devices consisting of multiple electrical, optical, or mechanical components.

One approach to simplify the coupling of micro-mechanical parts is that of single-step, *in situ* fabrication methods. Such methods must be capable of fabricating complex, pre-assembled mechanical structures consisting of integrated moving parts. At normal-scales, RP technologies provide the only fabrication method capable of producing *in situ* pre-assemblies. In particular, the SGC process is specifically adept to pre-assembly. Its unique ability to fabricate pre-assemblies with reasonably good tolerances is largely due to the backfilling of uncured photo-resin with solid wax after exposure under the photo-mask. Thus, each layer is fabricated upon a solid substrate and does not require supports to fabricate hard-to-build geometries such as cantilevers. After the part is fabricated, the solid cube of resin and wax can be washed with hot water to remove the wax. This process has been used to fabricate pre-assembled mechanical devices such as universal joints and three-dimensional gear meshes [BURN93]. The implementation of such a process at the micro-scale could have profound effects on the future of micro-mechanical fabrication.

2.2.3. Technological Issues

While the applications of RP technology to date are significant, improvements are needed to propagate many more potential applications of RP technology. Issues range from build speed to dimensional accuracy and surface finish to material properties to work envelope size. Below, these issues are discussed at greater length.

2.2.3.1. Voxel Geometry

Because most additive processes involve some type of scanning technique (see Figure 2.1), the technological issues associated with RP can be better understood by the concept of a *voxel geometry*. The term *voxel* is derived from the phrase *volume element* and is to 3D geometries what the term pixel (derived from picture element) is to 2D images.

The voxel is the fundamental building block of an additive, scanning process resulting from the material-process interaction. The shape of the voxel, or voxel geometry, is useful in that it determines the thickness of layers and distance between adjacent scans. For an additive, scanning process, it is important to understand how the material and process parameters of a process affect the voxel geometry.

An example of the importance of the voxel geometry can be found by reviewing voxel geometry models for the SLA technology. A picture of the voxel geometry formed by the interaction of a scanning laser on the surface of a liquid photo-monomer is shown in Figure 2.10. A derivation for this geometry has been developed [JACO92]. The working curve equation for describing this geometry in the yz-plane is shown in Equation 2.1:

$$y = \sqrt{\left(\frac{W_0^2}{2}\right) \cdot \left[\ln\left(\sqrt{\frac{2}{\pi}} \cdot \left[\frac{P_t}{(W_0 \cdot V_s \cdot E_c)}\right]\right) - \left(\frac{z}{D_p}\right) \right]} \quad (2.1)$$

where y is the linewidth, W_0 is the $1/e^2$ Gaussian half-width of the laser beam, P_t is the power of the laser, V_s is the scan velocity, E_c is the critical exposure of the resin, z is the

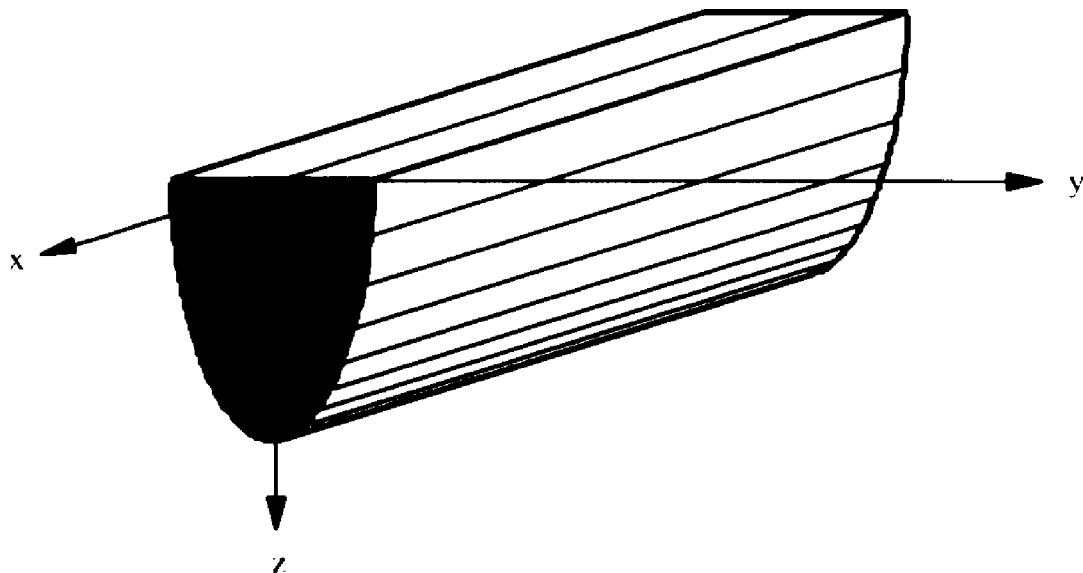


Figure 2.10. Schematic view of the SLA voxel geometry.

layer thickness, and D_p is the depth of penetration of the resin. From this formula, it is clear that the linewidth is inversely proportional to the scan velocity. Thus, it should be obvious that increasing the material addition rate (MAR) is not simply a matter of increasing the scan speed.

2.2.3.2. Material Addition Rate

Because a major motivating factor for developing RP technology has been accelerating product development, build time is a major concern. Build time consists of three major components: pre-processing, fabrication, and post-processing. While variations among pre-processing and post-processing times exist among all RP processes, the largest component of build time is the actual time required to fabricate the model. In general, for additive RP equipment, the fabrication time is further made up of two major components: layering and forming. By and large, the MARs associated with the forming step of the fabrication time are most representative of the speed at which models can be made on a particular process. The MAR can be defined as the volume of material added per unit time.

Using the concept of the voxel geometry, the MAR for additive, scanning RP processes can be computed by the following equation:

$$\text{MAR} = V_s \cdot A \quad (2.2)$$

where V_s is the scan rate (velocity) and A is the cross-sectional area of voxel geometry.

For non-scanning or hybrid, additive RP processes, the maximum MAR can be approximated by:

$$\text{max(MAR)} = \text{max}(V_f) / t_f \quad (2.3)$$

where V_f is the volume formed per layer and t_f is the forming time per layer. Table 2.5 shows some MARs calculated based on claims made by various RP equipment vendors.

Table 2.5. Material addition rates (MARs) calculated for various RP vendors.

| Method | Equipment | Scan Rate (mm/s) | Voxel Geometry* | | | MAR (mm ³ /s) |
|--------|--------------------|------------------|-----------------|-----------------------|----------------------------------|--------------------------|
| | | | Width (mm) | Depth (mm) | Cross-section (mm ²) | |
| FDM | FDM 1000 | 5-25 | 2.1 | 0.76 | 1.6 | 8-40 |
| | FDM 1500 | " | " | " | " | " |
| | FDM 1600 | " | " | " | " | " |
| | 3D Modeler | " | " | " | " | " |
| SGC | Solider 4600 | - | - | 0.1-0.2 [†] | - | 33 |
| | Solider 5600 | - | - | 0.1-0.2 [†] | - | 80 |
| SLS | Sinterstation 2000 | 1,000 | 0.38 | 0.08-0.5 | 0.02-0.125 | 20-125 |
| LOM | LOM 1015 | 380 | - | 0.05-0.4 [†] | - | ~330 |
| | LOM 2030 | 610 | - | " | - | 530 |
| SLA | SLA-190 | 762 | 0.2-0.29 | 0.1-0.9 | 0.02-0.261 | 15-200 |
| | SLA-250 | " | " | " | " | " |
| | SLA-400 | 4,160 | 0.2-0.25 | " | 0.02-0.225 | 80-900 |
| | SLA-500/20 | 1,780 | " | " | " | 35-400 |
| | SLA-500/30 | 5,080 | " | " | " | 100-1150 |

At first glance, it appears that the LOM and SLA processes are the dominate processes in terms of MAR. However, in most processes the MAR can be increased simply by increasing laminate thickness during the build cycle. As such, to allow for fair comparison of forming rates, the MARs must be standardized. One method for doing this is to compute the MAR using the same-sized voxels and the same laminate thicknesses. A comparison of MARs using this method of standardization is given in Table 2.6.

As a result, it is shown that the LOM and SGC processes probably have the greatest potential for forming rate. Of course, this is dependent upon the size of the object being produced. For large objects with large cross-sections, it would appear that the LOM and SGC processes have the fastest build times. For smaller cross-sections, the SLA machines would probably prevail. Further, the total build time is also dependent upon the number of items fabricated per batch. For example, the SGC process can fabricate many more small

* For the SLA, SLS, and FDM processes, these values were calculated by dividing the build rate by the scan rate to find the voxel cross-section and then using typical values for linewidth and linedepth which together represented the cross-section.

† These are typical values for the layer thickness in these processes.

Table 2.6. Comparison of material addition rates when using the same layer thickness (0.1 mm). For scanning based RP systems, the same sized voxel was used (0.02 mm³).⁵⁰

| Method | Equipment | Scan Rate (mm/s) | Quoted MAR (mm ³ /s) | Standardized MAR (mm ³ /s) |
|------------------|--------------------|------------------|---------------------------------|---------------------------------------|
| FDM | FDM 1000 | 5-25 | 40 | 0.1-0.5 |
| | FDM 1500 | " | " | " |
| | FDM 1600 | " | " | " |
| | 3D Modeler | " | " | " |
| SLS | Sinterstation 2000 | 1,000 | 20-125 | 20 |
| SLA | SLA-190 | 762 | 15-200 | 15 |
| | SLA-250 | " | " | 15 |
| | SLA-400 | 4,160 | 80-900 | 80 |
| | SLA-500/20 | 1,780 | 35-400 | 35 |
| | SLA-500/30 | 5,080 | 100-1150 | 100 |
| SGC | Solider 4600 | - | 33 | ~200 |
| | Solider 5600 | - | 80 | ~300 |
| LOM [†] | LOM 1015 | 380 | 530 | 330 |
| | LOM 2030 | 610 | ~800 | ~530 |

items per batch than the SLA machines simply because it doesn't require in-process supports.

In defense of the standardized MAR for the FDM process, this process does not require the layering required of all other additive processes. In this respect, the FDM process is similar to subtractive processes. Consequently, the FDM process while slow in the forming step is actually a faster process than indicated in the table. Overall, however, the FDM process is still considered a slower process than many of the other processes.

Further, the forming time per layer for the SGC process includes the time needed to remove uncured resin and backfill with wax. This suggests that the actual time needed to form the cross-section is probably very short (~5 seconds) and subsequently the MAR must be very large. However, since this process does have such a long time component due to layering, it is probably only fair to consider this in the MAR calculation. Similarly,

[†] These SGC build rates were calculated by taking the maximum exposed area in the work envelope by a 0.1 mm layer thickness and dividing by 60 seconds. This is based on a claimed throughput of about 1 layer per minute.

[‡] Assumes paper thicknesses on the order of 0.1 mm.

the MAR for the LOM process probably includes the average MAR including both layering and forming which, if removed, would increase its MAR.

2.2.3.3. Surface Finish and Texture

Surface finish and surface texture are great concerns in many RP applications such as those involving the use of RP parts as investment casting patterns or as aerodynamic test models. Because not all RP processes produce finished parts, additional secondary processes such as grinding or polishing may be necessary. These additional process steps can add additional time and cost to prototyping efforts. Because a goal of RP technology is to produce finished models quickly and cheaply, improvements in the surface finish and texture of RP parts becomes important.

Currently very little data exists concerning the surface finish and texture which can be expected of various RP processes. In general, it is expected that the powder-based RP processes will produce worse surface finishes than the photopolymer-based RP processes. And, further, it is expected that the surface finish and texture across the laminates (z-axis) is worse than the surface finish and texture of a laminate surface (x and y-axes). On one extreme using the SLA process, mirror finishes (less than 16 $\mu\text{in.}$ or 0.4 μm) have been achieved for surface roughness in the xy-plane. On the other extreme using the SLS and 3DP processes to process metal and ceramic powders, finishes on the order of several hundred micro-inches are typical.

By and large, the most dominant surface feature in most RP models is the “stair-stepped” surface texture caused by orienting a sloped or contoured surface parallel to the xy- (or slice) plane. This “stair-stepping” effect, as illustrated in Figure 2.11, is common to all current additive RP processes. In general, higher resolution of contoured surface can

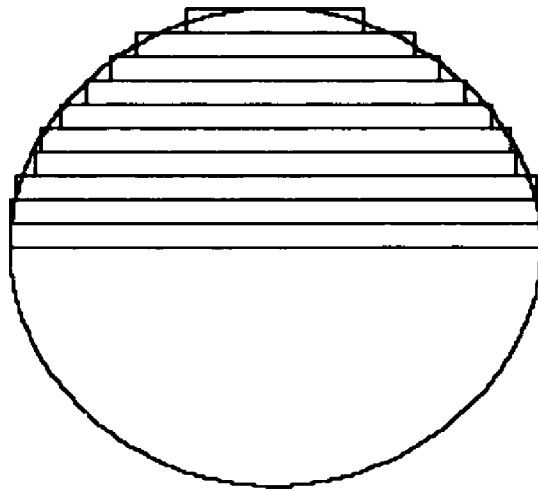


Figure 2.11. Stair-stepping effect due to additive freeform fabrication of a curved surface.

be obtained by orienting the perpendicular to the slice plane. Higher resolutions can also be obtained by reducing the laminate thickness during the build cycle. However, as shown in Table 2.7, a trade-off exists between the build speed of the machine and the laminate thickness.

Table 2.7. Extrapolated effect of layer thickness on build rates for the SLA -500/30.

| Max. Scan Rate (mm/s) | Width (mm) | Depth (mm) | Cross-section (mm ²) | Build Rate (mm ³ /s) |
|--------------------------|---------------|---------------|-------------------------------------|------------------------------------|
| 5,080 | 0.25 | 0.1 | 0.025 | 127 |
| | | 0.3 | 0.075 | 381 |
| | | 0.5 | 0.125 | 635 |
| | | 0.7 | 0.175 | 889 |
| | | 0.9 | 0.225 | 1143 |

2.2.3.4. Dimensional Accuracy

Table 2.8 provides a general sense for the part accuracies which a new user could expect in purchasing an RP system. This table is by no means comprehensive. The accuracies specified in the above table were formed as a result of contacting vendor organizations and reviewing product and technical literature. It was decided that the most uniform standard for dimensional accuracy would be over the entire work envelope. The above columns showing accuracy over the work envelope can be used for general comparison between processes.

Also note that many different vendor's products are not listed on Table 2.8. Therefore, the table better represents the difference in accuracy between various *processes*

Table 2.8. Dimensional accuracies claimed by various RP vendors.

| Method | Part Accuracy | | | |
|--------|-----------------------------|--------------------------|----------------------------|---------|
| | over Work Envelope | | over 0.635 cm [†] | |
| | XY mm (in.) | XY % | XY mm (in.) | XY % |
| SGC | 0.5 (0.02) | 0.1 | <0.1 (<0.004) | <1.6 |
| SLS | 0.4 (0.016) | 0.1 [†] | 0.053 (0.0021) | 0.83 |
| FDM | 0.127 (0.005) | 0.042 [†] | <0.127 (<0.005) | <2.0 |
| LOM | 0.25 (0.01) | 0.03 [†] | ~0.25 [‡] (~0.01) | ~4.0 |
| SLA | 0.125 - 0.25 (0.005 - 0.01) | 0.02 - 0.04 [†] | <0.05 (<0.002) | <0.8 |

^{*} This is the ultimate part accuracy over the entire work envelope as quoted per marketing and technical literature. However, as shown in the next column, better accuracies can be achieved over smaller dimensions for many processes.

[†] Most of these figures are rough estimates of the accuracy at 0.25 inches based on product literature and published case studies. They may be best used as a representation of the much improved accuracies which can be achieved at smaller scales for certain processes.

[‡] Calculated by dividing the claimed part accuracy over the envelope by the maximum dimension within the work envelope of the largest machine.

[§] Unlike many of the other processes material fabrication within the LOM process does not involve phase transformations. Thus, the assumption here is that the accuracy of the LOM process does not vary with dimensional proportion.

rather than between different *machines*. For example, it can be surmised from the Table 2.8 that curing of photo-polymers by laser tends to be a more accurate process than robotic extrusion of thermoplastics.

Several points must be considered when evaluating the accuracy of RP processes. First, and most important, is that operating conditions greatly affect the dimensional accuracy of RP parts. That is, a part fabricated under one set of processing conditions may have a different overall accuracy than a part built under another set of conditions. Build rate, part geometry, pre-processing, post-processing, material, and, to some degree, even ambient temperature and humidity can all affect the accuracy of RP processes. Therefore, it is difficult to specify a precise dimensional tolerance which will be met under all operating conditions. The numbers in Table 2.8 provide a starting point for comparing the dimensional accuracy of RP processes.

Another point to consider is the size of the parts to be fabricated. As shown in Table 2.8, for most processes, the part accuracy greatly improves as the measured dimension decreases. This is largely due to phase changes in the material as a result of processing. For example, most photo-resins have between 2 and 5 percent volumetric shrinkage upon polymerization. This shrinkage can result in internal residual stresses within the part which can ultimately cause part warpage, diminishing part accuracy. Similarly, shrinkage can occur in melting and fusing thermoplastics and sintering powder. Interestingly enough, no phase changes occur in the LOM process. As a result, the dimensional accuracy remains roughly the same regardless of the dimension size being measured. Thus, it might be surmised that if dimensional accuracy was important, the LOM process would be better for large parts while the SLA process might be better for small parts or parts with fine detail.

If dimensional accuracy is important, other factors may need to be considered as well. For example, a major limitation in seeking closer tolerances within many systems is

machine vibration. This is particularly important in many of the systems requiring vats of liquid because liquid is much more likely to be affected by vibration than solid material. Further, considerations need to be made for the expertise needed to minimize dimensional warpage caused by improper pre- or post-processing. For example, the placement of supports in the pre-processing of many RP parts can affect dimensional accuracy. In addition, the drawing style (e.g. sequential vs. random raster scan) selected in many SLA processes can also affect the dimensional outcome.

In summary, assessment of RP dimensional accuracy is very confusing. There are many different methods for collecting and synthesizing data used in measuring dimensional accuracy. As a result, it is difficult to know how a particular vendor arrived at the number quoted in the product literature. Overall, SLA probably has the best dimensional accuracy of the five processes listed. The reason for stating this is that the SLA process has the most rigorous testing standards for measuring dimensional accuracy. For example, at the 1994 Dayton Rapid Prototyping Conference, Paul Jacobs, Director of Research and Development for 3D Systems, Inc., maker of the SLA, claimed an e(90) accuracy of 0.003 inches (0.0076 cm). The e(90) metric is derived from measuring dimensions on the famed "User-Part", a standard test part developed in 1990 by a consortium of about 150 SLA users. This claimed accuracy suggests that over 90% of the measurements taken on User-Parts fabricated in an SLA will have tolerances of 0.003 inches (0.0076 cm) or less. As a result, prospective buyers of the SLA equipment have a much better idea of what they will be getting in terms of dimensional accuracy.

At the same time, the potential part accuracy of the LOM process may be higher than any others. First, the process uses very thin layers. Second, variations in layer thickness are compensated for by measuring the part thickness at various intervals and adjusting the slice plane within the software. Third, the material does not undergo any major phase changes. Fourth, the process does not require the production of in-process

supports. Thus, variation in accuracy due to placement of supports is not an issue. Fifth, the material in the LOM is solid and less vulnerable to vibration. Finally, much work is left to be done to select materials and methods which minimize distortion and warpage caused by non-uniform heat transfer during lamination though some work in this area has begun [PAK94].

Several disclaimers must be made for specific entries in Table 2.8. Much of the product literature for the SLS process claims a part accuracy of 0.25 mm (0.01 in.) for the first run and 0.125 mm (0.005 in.) on subsequent runs after adjusting process parameters. However, after direct contact with the vendor, a final figure of 0.4 mm (0.016 in.) was quoted over the entire work envelope.

2.2.3.5. Material Properties

In Table 2.9, various material properties are shown for some of the materials fabricated by the various additive RP machines. Notice that the properties given in Table 2.9 are not reflective of the anisotropic nature of material properties in additively fabricated models. In general, material properties are worse in the z-axis. Notice also that the material cost per unit volume is cheapest for the LOM machine.

As shown in the Table 2.9, the properties for many of the photo-resins have improved remarkably over when the first SLA was introduced. Most markedly, many of the photo-polymers are much tougher (less brittle) than the earlier resins. Many of the resin manufacturers have designed various resins for specific applications. For example, the DuPont Somos 5100 resin was developed for high accuracy applications while the 3100 resin was designed for applications requiring tough, transparent models.

2.2.3.6. Equipment Size and Work Envelope

In some industries, the size of additive RP fabricators are a problem. Table 2.10 shows some of the dimensions for current additive RP processes. Work envelope refers to the maximum volume which can be built within the machine. Of significance in this table is that the largest linear dimension is just under 3 feet. This can be a problem in industries such as aerospace which require large full-scale models.

Table 2.10 also denotes a market differentiation between large and small machines. At 4.5 metric tons, the largest SGC machine cannot be used as a desktop model. Conversely, the smallest FDM machine (at less than a meter cubed in volume) cannot be used for fabricating most production tooling. In general, the new FDM machines have been developed for the desktop markets while the remainder of the machines were

Table 2.9. Material properties claimed by various RP material vendors.

| Method | Material | Hardness Shore D | Tensile Stiffness GPa | Tensile Strength MPa | Tensile Ductility % elong. | Impact Strength (Izod) kJ/m ² | Material Cost US\$/dm ³ |
|--------|-------------------------------|------------------|-----------------------|----------------------|----------------------------|--|------------------------------------|
| FDM | Invest. Casting Wax | 33 | 0.28 | 3.5 | > 10.0 | - | 172 |
| | Machinable Wax | 40 | 0.48 | 7.7 | 6.65 | - | 172 |
| | Nylon | 70 | 0.55 | 12.2 | 3.48 | 13 | - |
| | Fine Nylon | 58 | 0.62 | 9.1 | 4.68 | 9 | 255 |
| | ABS | 105 | 0.25 | 34.5 | 50.0 | - | - |
| SLA | Ciba-Geigy Cibatool SL 5081-1 | 87-91 | 2.5-3.5 | 50-70 | 2-3 | 3 | 137 |
| | SL 5154 | 78 | 1.1-1.2 | 35 | 11-19 | 20-25 | - |
| | SL 5170 | 85 | 2.4-2.5 | 50-60 | 8-14 | 80-90* | - |
| | DuPont Somos 5100 | 97 | 0.88 | 22 | 10 | 14 | 168 |
| | DuPont Somos 3100 | 80 | 0.81 | 21 | 9.2 | 15 | 155 |
| | DuPont Somos 2100 | 41 | 0.037 | 7.1 | 46 | 150 | 160 |
| | SLS | Polycarbonate | - | 1.21 | 23.3 | 4.6 | 37.5 |
| | Nylon | - | 1.39 | 32.9 | 31.8 | 70 | 146 |
| SGC | Coates/Solimer Type F | - | 0.23 | 13 | 55 | - | - |
| | Type G | - | 0.88 | 35 | 16 | - | ~71 |
| LOM | Paper | - | 6.7 | 57 | 2 | 104 | 4 |

* After setting for 3 weeks.

Table 2.10. Equipment size, weight, and work envelope of various RP machines. 58

| Method | Equipment | Machine Size (W x L x H) m (ft) | Machine Weight kg (lbs.) | Work Envelope (W x L x H) cm (in.) |
|--------|-----------------------|---|-----------------------------|--|
| FDM | FDM 1000 | 0.66 x 0.86 x 0.86 (2.2 x 2.8 x 2.8) | 113 (250) | 25 x 25 x 25 (10 x 10 x 10) |
| | FDM 1500 | 0.66 x 0.93 x 0.86 (2.2 x 3.0 x 2.8) | 160 (350) | 25 x 25 x 25 (10 x 10 x 10) |
| | FDM 1600 | 0.66 x 0.93 x 0.86 (2.2 x 3.0 x 2.8) | 113 (250) | 24 x 24 x 24 (9.5 x 9.5 x 9.5) |
| | 3D Modeler | 0.76 x 0.91 x 1.7 (2.5 x 3.0 x 5.6) | 340 (750) | 30 x 30 x 30 (12 x 12 x 12) |
| SLS | Sinterstation 2000 | 3.0 x 1.5 x 2.0 (9.8 x 4.9 x 6.6) | 2,770 (6100) | 30 dia. x 38 (12 x 15) |
| SGC | Solider 4600 | - | - | 35 x 35 x 35 (14 x 14 x 14) |
| | Solider 5600 | 1.8 x 4.2 x 2.5 (5.7 x 13.6 x 8.2) | 4,500 (9,900) | 50 x 35 x 50 (20 x 14 x 20) |
| SLA | SLA-190 | 0.91 x 1.4 x 1.8 (3.0 x 4.7 x 6.1) | 272 (600) | 19 x 19 x 25 (7 x 7 x 10) |
| | SLA-250 | 0.91 x 1.4 x 1.8 (3.0 x 4.7 x 6.1) | 295 (650) | 25 x 25 x 25 (10 x 10 x 10) |
| | SLA-500 | 1.8 x 3.5 x 2.0 (6.0 x 11.3 x 6.7) | 932 (2,056) | 50 x 50 x 60 (20 x 20 x 24) |
| LOM | LOM 1015 | 1.0 x 1.1 x 1.2 (3.3 x 3.7 x 3.8) | 410 (900) | 25 x 34 x 38 (10 x 13.5 x 15) |
| | LOM 2030 | 2.1 x 1.3 x 1.3 (6.8 x 4.4 x 4.3) | 1500 (2,400) | 51 x 75 x 51 (20 x 30 x 20) |

developed for more general-purpose markets. Future market segmentation should be expected as further applications are developed for RP technology.

Table 2.11 shows an analysis of the equipment cost per unit work envelope for the additive RP machines. As shown, the LOM process provides the best cost per volume ratio indicating its compatibility with large products. Further, the FDM process would provide the best cost per volume ratio for small products.

Table 2.11. Analysis of equipment cost to work envelope for several RP systems. 59

| Method | Equipment | Machine Cost US\$ | Work Envelope cm ³ | Mach. Cost per unit Volume US\$/cm ³ |
|--------|--------------------|----------------------|----------------------------------|---|
| LOM | LOM 2030 | 199,000 | 195,075 | 1.0 |
| | LOM 1015 | 100,000 | 32,300 | 3.1 |
| FDM | FDM 1000 | 50,000 | 15,625 | 3.2 |
| | FDM 1500 | 62,000 | 15,625 | 4.0 |
| | 3D Modeler | 140,000 | 27,000 | 5.2 |
| | FDM 1600 | 80,000 | 13,824 | 5.8 |
| SGC | Solider 5600 | 550,000 | 87,500 | 6.3 |
| | Solider 4600 | 325,000 | 42,875 | 7.6 |
| SLS | Sinterstation 2000 | 340,000 | 26,861 | 12.6 |
| SLA | SLA-500 | 495,000 | 150,000 | 3.3 |
| | SLA-250 | 215,000 | 15,625 | 13.8 |
| | SLA-190 | 135,000 | 9,025 | 15.0 |

2.3. Electron Beam Processing

An electron beam is a highly collimated stream of electrons which are accelerated across an electric field towards a target. Electron beams are used throughout industry for various applications most notably within cathode ray tubes and electron microscopes. Electron beams must be transmitted in vacuum because the electrons will scatter upon interaction with gas molecules. The major difference between electron beams and other energetic rays such as lasers is that the constituent elements in an electron beam (i.e. the electrons) have mass and charge and, therefore, scatter upon interaction with the atoms and molecules of the target material. Understanding this scattering phenomenon is essential to the use of low-energy (less than 100 keV) electron beams in material processing. Below, several material-process interactions are discussed for electron beam processing along with some pertinent examples of models used in predicting material-process interactions within various industries.

2.3.1. Scattering

Electron scattering takes place through both elastic and inelastic scattering events. Elastic scattering events are characterized by large scattering angles with little energy transfer to surrounding atoms while inelastic events involve smaller scattering angles and energy loss. Thus, as the beam of electrons penetrates the material, the beam dilates and the electrons slow down releasing their kinetic energy to the material. Eventually, the electrons come to rest where they may be absorbed into the surrounding atoms of the material. The electron deceleration caused by inelastic scattering events ultimately limits the length of the electron path within the material. The ultimate path length of an electron within a material is dependent upon its initial, incident energy, E_0 , and the density of the target material and is known as the electron range.

Within an interaction volume between an electron beam and a substance, beam spreading is dominated by the elastic scattering events while energy loss is dominated by the inelastic events. Among the electrons scattering elastically within the material, a distinction may be made between forward-scattered, backward-scattered, and secondary electrons. Forward-scattered electrons are those electrons which have a cumulative angle of scatter less than 90 degrees to the direction of the incident beam. Logically, those electrons with a cumulative scattering angle greater than 90 degrees are called backward-scattered (backscattered) electrons. Secondary electrons are those electrons which are displaced from atoms in the material as a result of inelastic collisions with the primary (forward- or backward-scattered) electrons. Mathematical treatments for calculating the energy deposition due to forward-scattered and backscattered electrons are different. Typically, energy deposition models of forward-scattering and backscattering electrons include the effect of secondary electrons.

As mentioned, inelastic events result in energy transfer to the target material. The energy dissipation ($-dE/dz$) due to inelastic scattering events can be estimated by using Bethe's continuous slowing down approximation (CSDA) [BROD82]:

$$-\frac{dE}{dz} = \frac{N_A e^4}{2\pi\epsilon_0^2} \cdot \frac{Z\rho}{A} \cdot \frac{1}{E} \ln\left(\frac{1.66E}{J}\right) = -7.85 \times 10^4 \cdot \frac{Z\rho}{AE} \ln\left(\frac{1.66E}{J}\right) \quad (2.4)$$

where dE is the change in energy of the electron of energy E (keV) while traversing a path of length dz (cm), Z is the atomic number, A is the atomic weight, ρ is the material density, and J is the mean ionization energy. This energy loss per electron per unit path length in a material is known as the material stopping power, S_e . At lower electron energies (less than 10 keV), Bethe's CSDA gives negative values. Parabolic extrapolations for the CSDA have been proposed by Rao-Sahib and Wittry [RAO74] and Love, et al. [LOVE78], at lower electron energies.

While the stopping power is a good estimate of the energy deposition within a material, the actual energy absorbed by a material due to inelastic collisions is not linear over the entire electron range. Rather, as shown in Figure 2.12, the material experiences a maximum energy absorption at approximately 40% of the electron range [SPEN55]. It has been theorized that this maximum is due primarily to the cascading of secondary electrons within the material. The curve in Figure 2.12 is termed the depth-dose curve and shows the relative stopping power of a material over the electron range.

Several empirical and analytical formulas have been developed for estimating the electron range within a material. The Bethe range, R_b , can be estimated by integrating Equation 2.4 above as a function of the electron energy over the interval E_0 to zero. However, this range overestimates the ultimate penetration into the material since the path of the electron is not straight. The Grun range, R_g , is a better estimate of the ultimate electron penetration within a material and can be found by extrapolating the linear portion of

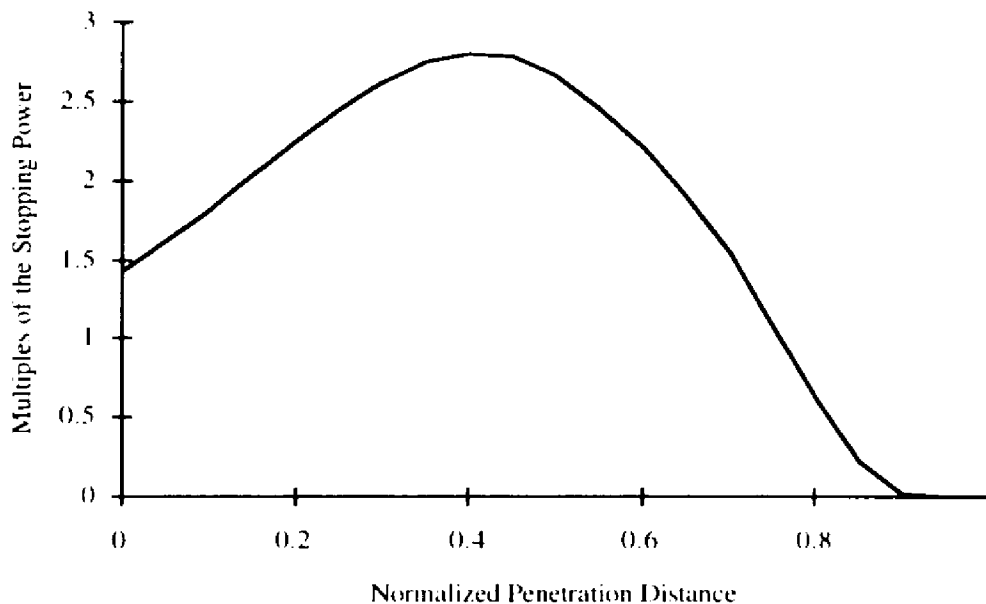


Figure 2.12. Depth-dose curve for 25 keV electrons in carbon.

the depth-dose curve to the x-axis. Between the electron energies of 5 keV and 25 keV, R_q can be estimated by the following empirical formula [EVER71]:

$$R_q = 4.0 \cdot E_0^{1.75} \quad (2.5)$$

Overall, the dimensions of the interaction volume between the beam and the material is bounded by the electron range in the material. Due to the elastic scattering of electrons within the material, the shape of the interaction volume can be characterized as a pear for materials with low atomic numbers at high electron energies and as a plum for materials with high atomic numbers at low electron energies [REIM79].

2.3.2. Polymerization

Exposure of a material to an electron beam produces various ionizing effects within the material. Within certain monomeric materials, these ionizing effects can result in free-radical and ionic polymerization. In fact, electron-beam (EB) polymerization has been used throughout various polymer coating industries to accelerate the curing of protective and

aesthetic coatings [HOFF73]. Of key significance to EB polymerization is the energy dose, D_g , at which the liquid monomer is transformed into a solid polymer.

For thermoset resins, the point at which the monomer becomes polymer is termed the gel point. In the special case where all original molecules are of the same size (e.g. monomer units), gel formation begins when there is one cross-link for each two molecules originally present [WILS74]. Thus, an estimate for D_g can be made by halving the number of monomer units per gram and multiplying the result by the energy needed to create a polymer unit. Given a sample of monomer of molecular weight, M_o , the number of molecules per gram of material can be found by:

$$N_o/M_o \quad (2.6)$$

where N_o is Avogadro's number. Further, the energy needed to initiate polymerization can be expressed in terms of the G-value for creating polymer chain units, G_p , the number of polymer units produced per 100 eV absorbed energy [SENI84]. Thus, an estimate for D_g can be made by:

$$D_g = N_o/M_o * 1/2 * 1/G_p = N_o/(2*M_o*G_p) \quad (2.7)$$

Adjusting for units, D_g (in rads) is expressed by [WILS74], [GUIL85].

$$D_g = 4.826*10^{11}/(M_o*G_p) \quad (2.8)$$

where M_o is in grams and G_p is in polymer units produced per 100 eV.

2.3.3. Cross-Linking and Chain Scission

The exposure of polymers to an electron beam can result in different ionizing effects including cross-linking and chain scission. Cross-linking results when a chemical bond is formed between the monomer units of different polymer chains. Because of cross-linking, the polymer chains become more resistant to dissolution in a solvent. Alternatively, ionizing radiation can result in chain scission where an initial polymer chain is separated into two smaller chains. Chain scission causes a polymer to become more soluble in a

solvent. In general, the chemical structure of a polymer determines which of the two ionizing effects predominate.

Because of these ionizing effects, electron beams are used within the microelectronics industry to produce micro-lithography masks for integrated circuit fabrication. In electron-beam micro-lithography, a polymer resist is layered onto a substrate and selectively exposed to an electron beam (EB). Subsequent development in a solvent produces a pattern where the polymer was exposed to the electron beam. Those polymers in which cross-linking predominate are called negative EB resists. EB exposure and development of a negative resist results in the dissolution of the unexposed resist in the solvent. Those polymers in which chain scission predominate are called positive EB resists. Development of an EB exposed positive resist results in its dissolution in a solvent.

The effects of ionizing radiation in matter are dependent upon the energy dose delivered by the radiation. For electron beam irradiation, the degree of cross-linking and chain scission is sensitive to the energy dose delivered. For EB resists, this sensitivity is typically measured in charge per unit area (e.g. $\mu\text{C}/\text{cm}^2$). As shown in Table 2.12, the sensitivity of EB resists is dependent upon many factors [BEDN93]. For positive resists, Herzog, et al., [HERZ71] developed the following equation quantitatively relating many of these factors to resist sensitivity:

$$\rho = \left[\frac{100 \cdot q \cdot \rho_r \cdot A_n}{E \cdot G(s)} \right] \cdot \left(\frac{1}{\overline{M}_f} - \frac{1}{\overline{M}_n} \right) \quad (2.9)$$

where ρ is the resist sensitivity (C/cm^2), q is the electronic charge ($1.6 \cdot 10^{-19} \text{ C}$), ρ_r is the density of the resist (g/cm^3), A_n is Avogadro's number, \overline{M}_n is the number average gram molecular weight of the original polymer, \overline{M}_f is the number average gram molecular weight of the fragmented (scissioned) polymer, E is the energy loss per centimeter for the electron

Table 2.12. Parameters affecting resist sensitivity.

| Parameter Type | Parameter |
|----------------|---|
| Material | Chemical composition Molar mass Molar mass distribution Temperature of glass transition (T _g) Density Average value of proton number |
| Process | Development conditions Developer composition Prebaking and postbaking |

traversing the resist, and $G(s)$ is the radiation chemical yield for scission events defined as the number of chemical events per 100 eV of energy absorbed by the resist.

The sensitivity of a polymer to EB irradiation is typically measured with the use of a characteristic curve for that polymer. Figure 2.13 shows a typical characteristic curve for a positive EB resist [BEDN93]. This curve shows that the time needed to dissolve the resist within a solvent decreases with increasing exposure and absorbed dose. Thus, for a given solvent, the extent of development within EB resists requires knowledge of the absorbed dose within the resist as well as the development time.

2.3.4. Process Models

Several EB process models are pertinent to the model development conducted within this thesis. In polymer coating industries, electron beams are used to accelerate the curing of printing inks, paints, and other polymeric coatings. In the microelectronic industry, electron beams are used in direct-write-on-wafer lithography, in addition to its more common application of maskmaking. Below, some process models used in controlling these processes are discussed.

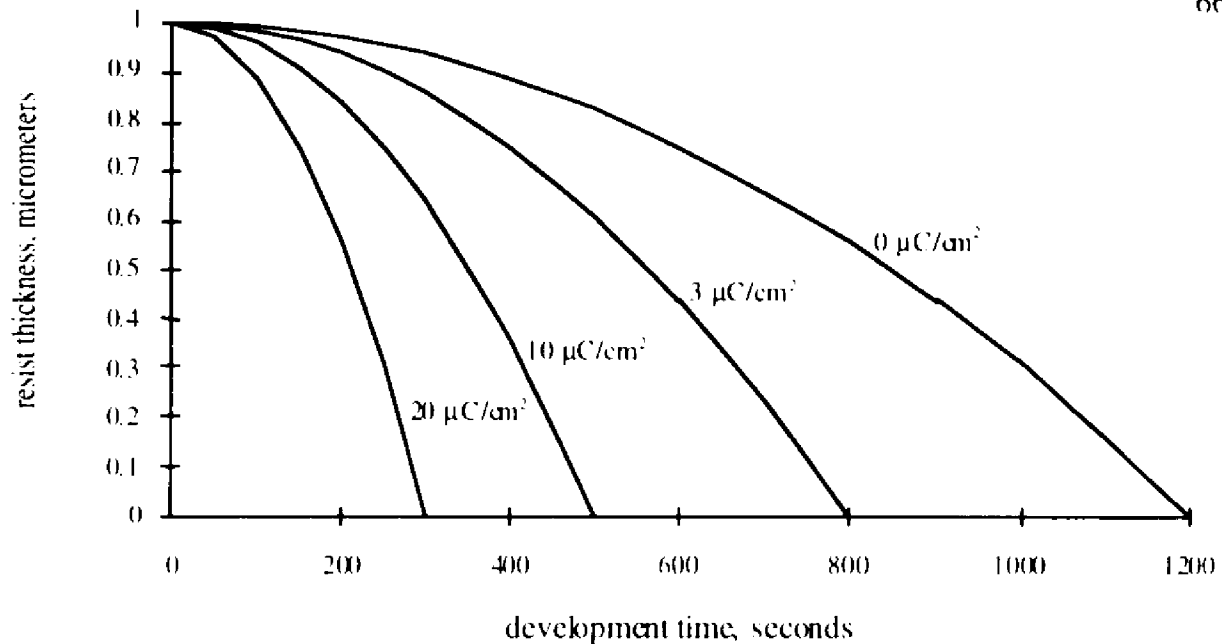


Figure 2.13. Kinetic curves of dissolution as a function of dose for a positive EB resist. Four curves represent four different exposure doses.

2.3.4.1. Polymer Coating Models

A typical production environment for the EB curing of coatings involves the conveyance of work to be processed past the window of a scanned-beam EB device. In such an environment, a narrow electron beam is scanned electro-magnetically over the work surface perpendicular to the conveyor's direction of travel. Given this configuration, a manufacturing engineer must understand the interaction among several different processing parameters including conveyor speed, accelerating voltage, and beam current in order to produce high volumes of quality parts.

Assuming that the energy dissipation of electrons entering the coating follows the relationship shown in Figure 2.12, the total energy (per incident electron) dissipated at a depth, z , in an interval, Δz , in the coating including all secondary particles is given by [CLEL76]:

$$\Delta E = S_{e_0} \cdot J(Z) \cdot \Delta z \quad (2.10)$$

where S_{e_0} is the stopping power of the incident electrons of energy E_0 , $J(Z)$ is the normalized energy dissipation function established by Spencer [SPEN59], $\Delta z = \rho \Delta t$ is the interval over which the energy is dissipated in g/cm^2 , Δt is the interval over which the energy is dissipated in cm, and $Z = z/r_0$ is the depth, z , into the coating expressed as a fraction of the maximum range, r_0 . This can be expanded as follows by multiplying both sides by (I/e) , the number of electrons entering the coating per second:

$$\left(\frac{I}{e}\right)\Delta E = I[S_{e_0} \cdot J(Z)/e]\Delta z \quad (2.11)$$

where I is the beam current in milliamps and e is the electronic charge in coulombs/electron. The absorbed dose rate at depth, z , in the differential volume, $A \Delta t$, can be found by dividing both sides of the equation by the differential mass element, $\Delta M = A \Delta z$:

$$\left(\frac{I}{e}\right)\frac{\Delta E}{\Delta M} = I\frac{[S_{e_0} \cdot J(Z)/e]}{A} \quad (2.12)$$

If the electron current, I , is expressed in milliamps and the stopping power, S_{e_0} , is given in $\text{MeV}\cdot\text{cm}^2/\text{g}$, the units of Equation 2.12 are kW/g . This can be further reduced as follows to obtain a value for the absorbed dose (in Mrad) as a function of the percentage of the penetration range, Z :

$$D(Z) = 36I\frac{[S_{e_0} \cdot J(Z)/e]}{(A/T)} \quad (2.13)$$

where I is in milliamps, S_{e_0} is in $\text{MeV}\cdot\text{cm}^2/\text{g}$, A is in m^2 , and T is in hours. For polymer coating applications, A/T represents the area throughput rate which is a function of the width and speed of the conveyor. This equation assumes that all of the current from the beam is productively used within the coating.

Equation 2.13 suggests that the absorbed energy dose within the coating is directly proportional to the beam current density (I/A) and beam accelerating voltage [via $J(Z)$].

Given the gel dose of the coating, this equation can be used by a manufacturing engineer to determine whether the exposure dosage is great enough to cure the entire coating thickness.

2.3.4.2. Micro-Lithography Models

In EB lithography, an electron beam is scanned over a layer of polymeric electron resist. After being patterned by the beam and developed in a solution, the remaining resist (named such for its ability to resist chemical etching) is used to allow the selective etching of the underlying substrate. Much research has been conducted within the microelectronics industry to determine the profile shape produced by scanning an electron beam over the surface of an EB resist. This understanding is critical for optimizing resist linewidths and, ultimately, circuit densities.

The accelerating voltages used within EB lithography are much less than those used in polymer coating applications. In polymer coating, electron beam parameters are tailored so that the depth of curing is just greater than the thickness of the polymer coating. In microlithography, the electron penetration is many times greater than the thickness of the resist. The reason for this is shown graphically in Figure 2.14. Notice that as the beam penetrates the solid matter it becomes increasingly more diffuse. To minimize linewidths, EB lithography is normally conducted at electron energies high enough to restrict the electrons to only a few elastic scattering events within the resist.

Efforts to model the effects of electron scattering on EB lithography have employed both Monte Carlo techniques [JOY88], [KYSE74] as well as analytical models. Monte Carlo techniques require the calculation of several thousand electron trajectories in order to estimate the energy dissipation of a beam within a resist implying a great deal of computer time. Sensitivity analysis, involving the alteration of model parameters such as resist density or beam accelerating voltage, requires computation of several thousand more

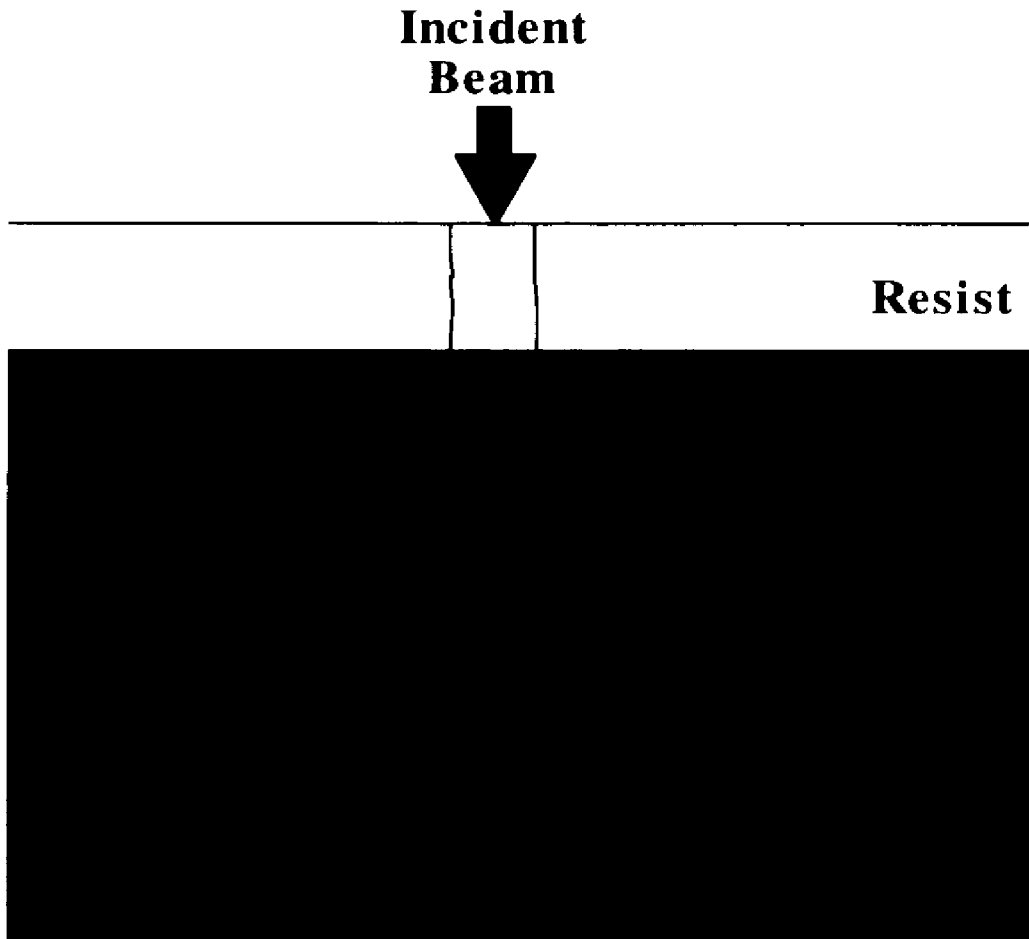


Figure 2.14. Schematic of EB lithography process showing the scattering of the electron beam and its interaction with both the electron resist and the resist substrate.

trajectories. For practical reasons, analytical models for predicting electron energy dissipation can be useful.

As suggested, in EB lithography, it is convenient to characterize scattering in thin films by the average number of elastic events, p_e , which an electron suffers in passing through the resist. When energy loss is neglected, p_e is obtained by multiplying the total elastic scattering cross section for a single scattering center by the density of scattering centers [GREE74] as follows:

$$p_e = \frac{(\pi \cdot Z^2 \cdot e^4 \cdot N_a \cdot \rho)}{A} \cdot \frac{T}{(E_e^2 \cdot \theta_e^2)} \quad (2.14)$$

where T is the resist thickness and θ_0 is the screening parameter which characterizes the screening of the nuclear charge by the atomic electrons. According to Cosslett and Thomas [COSS64] the theoretical scattering regime for modeling the scattering behavior changes as p_c changes. For a p_c less than 20, the scattering behavior can best be modeled by a “plural” scattering regime. Between 20 and about 50 elastic scattering events, a “multiple” scattering regime dominates. Above 50 elastic scattering events, a “diffusive” scattering regime exists.

For the most part, analytical models for predicting resist profiles have been based primarily on plural and multiple scattering theories for electron scattering. Most notable has been the work of Greeneich and Van Duzer [GREE74] based on plural scattering which has been found to be accurate over a wide range of accelerating voltages and resists. Their success has been mainly due to the fact that the p_c for a typical resist layer under normal EB lithography accelerating voltages is in the range of 3 to 20. Nosker [NOSK69] and Hawryluk, et al. [HAWR74], [HAWR72], have developed analytical models for predicting electron beam exposure profiles in polymer resists based on multiple scattering theory. The results of plural and multiple scattering models have been compared [HAWR74] and the plural scattering regime has been shown to be superior for typical EB lithography settings.

More recently, advances in EB lithography have been made by using lower accelerating voltages to obtain smaller linewidths [SUGI88], [MCCO92]. The primary advantage of low-energy EB lithography is the virtual elimination of electron proximity effects. Proximity effects are caused by forward and backward-scattered electrons in the resist which partially expose the resist up to several micrometers from the point of impact. As a result, variations in exposure dosages under the scanning pattern occur when pattern geometries fall in the submicrometer range. Electron proximity effects are a function of the electron range within the material which is a function of electron accelerating voltage. As shown in Figure 2.15, the scattering range of low-energy electrons is restricted to a small

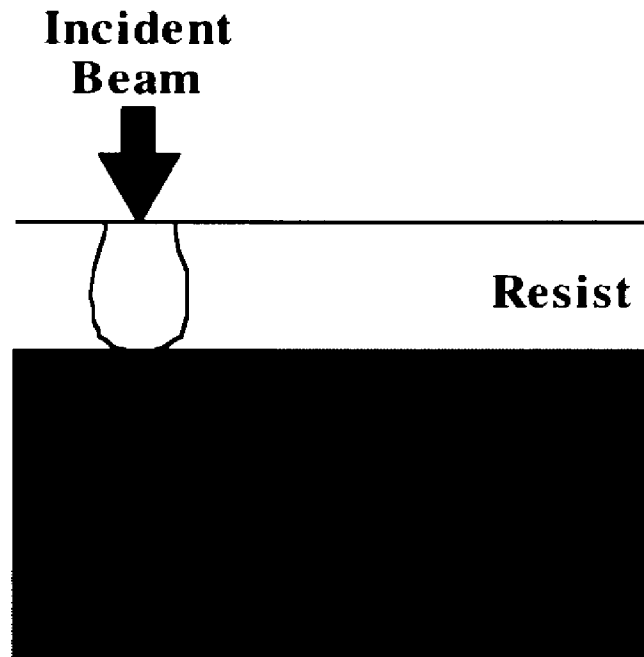


Figure 2.15. Schematic of low-energy EB lithography process showing a much smaller interaction with both the electron resist and the resist substrate.

region around the initial point of penetration, thus reducing the proximity effect. Because of this, low energy EB lithography results in much better pattern resolution.

Also shown in Figure 2.15, low-energy EB lithography results in the loss of electron energy almost entirely within the resist. As such, analytical models for predicting the interaction profile must take into account diffusive scattering. Glezos, et al. [GLEZ92], [GLEZ94], and Raptis, et al. [RAPT93A], [RAPT93B], have developed an analytical approach for evaluating the electron energy deposition for a point beam incident vertically over a semi-infinite, composite substrate based on the diffusion approximation of the Boltzmann transport equation. In their approach, an electron probability distribution function is calculated and multiplied by the incoming electron density and material stopping power. A one-dimensional electron probability distribution function, $\rho(z,E)$, is found first by solving the Boltzmann transport equation using the diffusion approximation and

appropriate boundary conditions [BETH38]. The total electron probability distribution function, $\rho(r,z,E)$, can be found by:

$$\rho(r,z,E) = \rho(z,E) \left[\rho_f(r/z,E) + \rho_b(r/z,E) \right] \quad (2.15)$$

where the indices f and b stand for forward scattering and backscattering, respectively. The vertical bar denotes conditional probabilities. The forward scattering portion is calculated following the known multiple scattering model.

Jacob [JACO74] has developed a more accurate solution to the diffusion approximation of the Boltzmann transport equation for materials with an atomic number less than 30. A solution for the one-dimensional electron probability distribution function, $\rho(z,E)$, was developed for a planar electron beam source.

3. STATEMENT OF PROBLEM

Based on the review of recent micro-mechanical fabrication research, it has been established that micro-scale mechanical assembly is a problem limiting the high-volume production and proliferation of many actuator-based micro-mechanical applications. Further, based on the review of current freeform fabrication methods, it has also been established that certain freeform fabrication methods are capable of fabricating *pre-assembled* mechanical systems complete with moving components. Therefore, it is proposed that a micro-scale freeform fabrication technique capable of pre-assembly would be of benefit in the fabrication of actuator-based, micro-mechanical systems.

Current micro-scale freeform fabrication techniques are not capable of pre-assembly. In addition, these techniques provide limited resolution resulting in poor surface texture, dimensional accuracy, and aspect ratio. The following technological challenges must be addressed in the development of a micro-scale freeform fabrication technique capable of pre-assembly:

- improved resolution and precision
- eliminate need for material supports
- easy removal of excess material

The fabrication approach proposed within this research is to fabricate pre-assembled micro-mechanical systems layer-by-layer using electron-beam lithography methods.

Specifically, the approach is an additive freeform fabrication method involving:

1. layering an electron resist by spin coating;
2. selectively patterning the resist with a low-energy (less than 10 keV) electron beam;
3. repeating steps one and two until the three-dimensional geometry is complete; and

4. when finished, dissolving away any uncured resist in a development solvent.

3.1. Thesis Statement

Direct application of electron beam energy will provide superior dimensional resolution (voxel size and shape) over existing micro-scale freeform fabrication technologies. Direct application includes additive processes such as polymerization or fusion and subtractive processes such as polymer scission. In addition, direct application of electron beams in certain solid material systems will provide the additional advantage of pre-assembly. Solid material systems of particular interest include electron-sensitive polymers and fine powder metals because of their ability to be removed after processing. These advantages can be demonstrated in a positive electron resist used in electron beam microlithography.

3.2. Objectives of the Proposed Research

Critical to using the proposed process in micro-mechanical fabrication is the control of the electron penetration profile (voxel geometry) dimensions created by taking a single electron beam scan across the surface of an electron resist. Current polymer coating and microlithography models for calculating electron beam penetration (linedepth) and scatter (linewidth) are inadequate for the proposed process since it will operate at low electron accelerating voltages (i.e. < 5 keV).

The objective of this model can be stated as follows: given a low-energy beam (accelerating voltage, current density, beam radius, and scanning speed) normally incident upon a positive electron resist (density, atomic number, atomic weight, and critical dosages for dissolution), determine the width and depth of the line produced by scanning the

electron beam over the surface of the resist. The objectives of this model are shown graphically in Figure 3.1.

In order to validate this model, linewidth and linedepth data from the literature is compiled along with experimental data collected by scanning an electron beam over a polymethyl methacrylate (PMMA) resist within an environmental scanning electron microscope (ESEM). In addition, a multi-layer microstructure will be fabricated to prove feasibility of the fabrication approach.

In summary, the objectives of the proposed research are as follows:

1. to compare the dimensional resolution (voxel size and shape) of the proposed process with existing UV-based micro-scale freeform fabrication technologies;
2. to develop an analytical model which predicts the width and depth of the dissolved line formed by scanning a low-energy (less than 10 keV) electron beam over the surface of a positive electron resist;

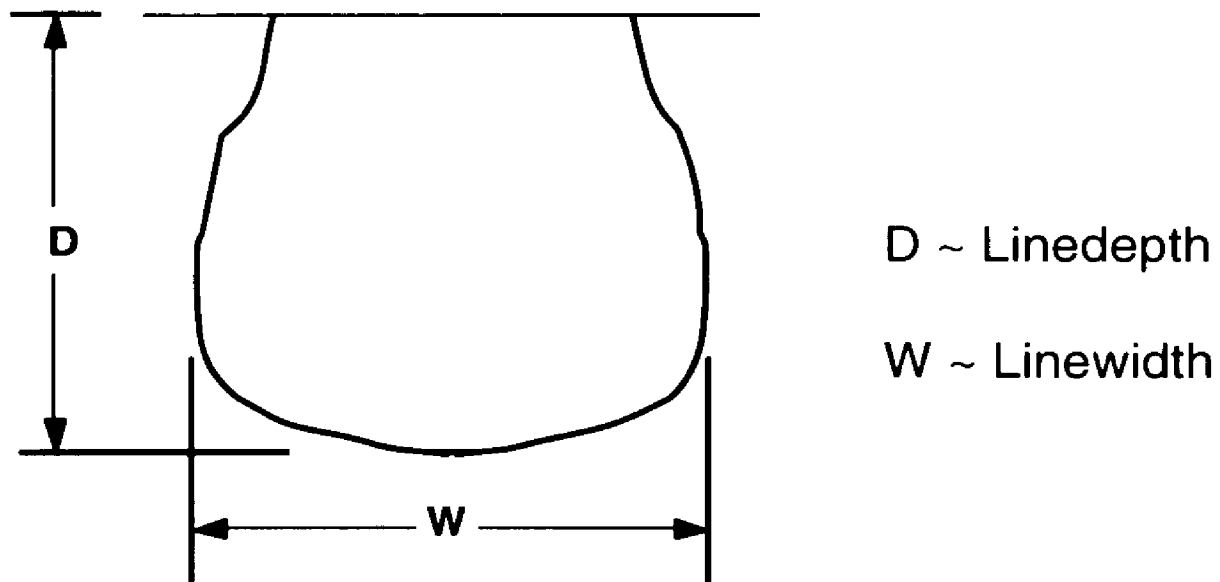


Figure 3.1. Graphical depiction of the model objectives.

3. to test the validity of the model using experimental data; and
4. to test the feasibility of the proposed microfabrication approach.

4. PRELIMINARY INVESTIGATION

A preliminary, proof-of-principle investigation was performed to determine the feasibility of using an electron beam and electron-sensitive material to fabricate micro-mechanical structures. In this investigation, efforts were made to fabricate a multi-layer micro-structure. This was accomplished by developing a simple electron energy dissipation model to define the experimental parameters needed to prove feasibility, selecting an experimental setup for proving feasibility, and conducting proof-of-principle experiments. It was determined that an initial investigation could be undertaken within the specimen chamber of an environmental scanning electron microscope (ESEM). Using the ESEM, a styrene monomer vapor was condensed onto a temperature-controlled sample holder. These preliminary efforts are described in more detail below.

4.1. Simple, Electron Energy Dissipation Model

In order to define the experimental parameters needed to show process feasibility, a model was needed relating the material and process variables to the fundamental, profile geometry created by taking a single EB scan across the surface of an electron sensitive material. This profile geometry, termed the voxel (volume element) geometry, is important in that it represents the “building block” of the technology. That is, voxels can be used to make lines, lines can be used to make planes, and planes can be used to make three-dimensional geometries such as cubes.

The model developed below parallels the model development of Cleland, et al. [CLEL76], for EB-cured polymer coating and Jacobs [JACO92] for the StereoLithography process. Consider a Gaussian electron beam being scanned in a straight line at a constant velocity, V_x , over the surface of a liquid resin, as shown in Figure 4.1. For this setup, the following coordinate system will be adopted:

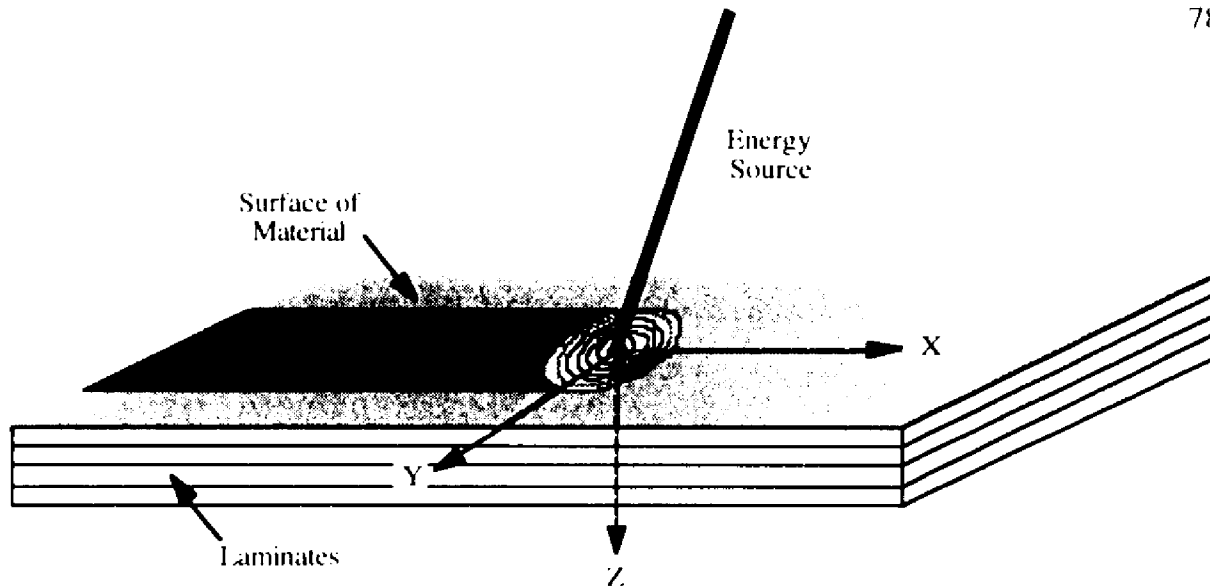


Figure 4.1. Coordinate system for the approach used in the preliminary investigation.

1. The xy plane is coincident with the liquid surface,
2. The x axis is coincident with the centerline of the scanned beam, with positive x in the direction of the beam scan, and
3. The z axis is normal to the resin surface, with positive z directed downward into the resin.

In this model, it is assumed that the scan is from $x = -\infty$ to $x = +\infty$, at a constant scan velocity, V_s . It is also assumed that the absorption of electron energy within the resin follows the simplified energy dissipation function as specified by Spencer [SPEN59] for planar sources. Under these conditions, the total energy dissipated (per incident electron), ΔE , at a depth z in an interval Δz , in an absorber is given by [CLEL76]:

$$\Delta E = S_0 J_0(\zeta_0) \Delta z \quad (4.1)$$

where $S_0 = S(E_0)$ is the stopping power of the absorbing material given an incident electron energy of E_0 ; $J_0(\zeta_0)$ is the normalized energy dissipation function of an electron established by Spencer [SPEN59]; $\zeta_0 = z_0/r_0$ is the depth, z_0 , in the absorber expressed as a fraction of the Grun range, r_0 ; $\Delta z = \rho \Delta t$ is the interval over which the energy is dissipated in g/cm^2 ; and Δt is the interval over which the energy is dissipated in cm.

Let I_b be the electron beam current; then, (I_b/e) is the number of electrons per second where e is the electronic charge. Multiplying Equation 4.1 by (I_b/e) gives the energy absorbed per second in the material:

$$\left(\frac{I_b}{e}\right) \cdot \Delta E = I_b \cdot \frac{S_0 J_0\left(\frac{\rho \cdot z}{r_0}\right)}{e} \cdot \Delta z \quad (4.2)$$

The differential mass element exposed to the electron beam, ΔM , is defined [CLEL76]:

$$\Delta M = A \cdot \Delta z \quad (4.3)$$

where ΔM is the finite mass element in which the total energy of the electron beam is dissipated in grams, A is the cross-sectional area exposed by the electron beam at that instant of time in cm^2 , and Δz is the interval over which the energy is dissipated in g/cm^2 .

The absorbed dose (energy per unit mass) rate is obtained by dividing Equation 4.2 by Equation 4.3:

$$\left(\frac{I_b}{e}\right) \cdot \left(\frac{\Delta E}{\Delta M}\right) = \frac{I_b \cdot \frac{S_0 J_0\left(\frac{\rho \cdot z}{r_0}\right)}{e}}{A} \quad (4.4)$$

The left side of Equation 4.4 is equal to the dose rate of the electron beam in the material, $D(\zeta_0)/t$, expressed in kW/g. Recognizing that $1 \text{ kW/g} = 100 \text{ Mrad/s}$ and that (I_p/A) is the average current density, j , Equation 4.4 reduces to:

$$\frac{D(z)}{t} = 100 \cdot j \cdot \frac{S_0 J_0 \left(\frac{\rho \cdot z}{r_0} \right)}{e} \quad (4.5)$$

where $D(\zeta_0)/t$ is the dose rate of the electron beam in the material as a function of depth in Mrad/s; j is the average current density of the electron beam in mA/cm²; S_0 is the stopping power of the absorbing material at an incident electron energy of E_0 ; $J_0(\zeta_0)$ is the normalized energy dissipation function of an electron as a function of the electron penetration ζ_0 ; and e is the electronic charge.

Further let:

$$D(z) = \int_{-\infty}^{\infty} \frac{D(z)}{t} dt \quad (4.6)$$

Then, combining Equations 4.5 and 4.6:

$$D(z) = 100 \cdot \frac{S_0 J_0 \left(\frac{\rho \cdot z}{r_0} \right)}{e} \cdot \int_{-\infty}^{\infty} j dt \quad (4.7)$$

Given that a low perveance gun is being used (i.e., $I_p/(E_0)^{1.5} < 10^{-8} \text{ A} \cdot \text{V}^{-1.5}$), the electron beam is assumed to be monoenergetic with a Gaussian beam current density as follows [SCHI82]:

$$j(r) = j_{\max} \cdot \exp\left(-\frac{r^2}{r_b^2}\right) \quad (4.8)$$

where $j(r)$ is the current density on the resin surface at distance, r , from the center point of the beam in mA/cm²; r_b is the radius of the beam on the resin surface (i.e. the radius at which the current density is $1/e = 37\%$ that of the center); and j_{\max} is the maximum current

density incident upon the resin surface corresponding to the current density at the center of the beam. Using the coordinate scheme introduced earlier, several facts are true during the scan:

$$r^2 = x^2 + y^2 \quad (4.9)$$

$$y \sim \text{constant}$$

$$V_s = dx/dt$$

$$dt = dx/V_s \quad (4.10)$$

where V_s is the scan velocity of the electron beam. Given Equation 4.9, the following is true:

$$\exp\left(-\frac{r^2}{r_b^2}\right) = \exp\left(-\frac{x^2}{r_b^2}\right) \cdot \exp\left(-\frac{y^2}{r_b^2}\right) \quad (4.11)$$

Substituting Equations 4.8, 4.10, and 4.11 into Equation 4.7 gives:

$$D(y, z) = 100 \cdot \frac{S_o J_o \left(\frac{\rho, z}{r_o}\right)}{e} \cdot \frac{j_{\max} \cdot \exp\left(-\frac{y^2}{r_b^2}\right)}{V_s} \cdot \int_{-\infty}^{\infty} \exp\left(-\frac{x^2}{r_b^2}\right) dx \quad (4.12)$$

Solving the integral by substitution, define [JACO92]:

$$u^2 = x^2/r_b^2 \quad (4.13)$$

$$u = x/r_b$$

$$du = dx/r_b$$

$$dx = r_b \cdot du \quad (4.14)$$

Substituting Equations 4.13 and 4.14 into Equation 4.12 gives:

$$D(y, z) = 100 \cdot \frac{S_o J_o \left(\frac{\rho, z}{r_o}\right)}{e} \cdot \frac{j_{\max} \cdot \exp\left(-\frac{y^2}{r_b^2}\right) \cdot r_b}{V_s} \cdot \int_{-\infty}^{\infty} \exp(-u^2) du \quad (4.15)$$

Realizing that the Gaussian distribution is the same above zero as below zero:

$$D(y, z) = 100 \cdot \frac{S_0 J_0 \left(\frac{\rho \cdot z}{r_0} \right)}{e} \cdot \frac{j_{\max} \cdot \exp\left(-\frac{y^2}{r_b^2}\right) \cdot r_b}{V_c} \cdot 2 \cdot \int_0^{\infty} \exp(-u^2) du \quad (4.16)$$

Using integral calculus tables [JACO92]:

$$\int_0^{\infty} \exp(-u^2) du = \frac{\sqrt{\pi}}{2} \quad (4.17)$$

Thus,

$$D(y, z) = 100 \cdot \frac{S_0 J_0 \left(\frac{\rho \cdot z}{r_0} \right)}{e} \cdot \frac{j_{\max} \cdot \exp\left(-\frac{y^2}{r_b^2}\right) \cdot r_b \cdot \sqrt{\pi}}{V_c} \quad (4.18)$$

For EB curable polymers, when the absorbed dose is less than some critical value, D_c , the resin remains liquid [GUIL85], [WILS74]. For thermoplastic monomers, D_c is defined as the energy dose needed to raise the glass transition temperature above the process temperature. This point is known to happen when the percent conversion within a polymer reaction has reached a critical value, X . When a thermoplastic monomer is exposed to irradiation, free radicals are formed. The energy needed to form these radicals can be expressed in terms of the G-value for radical formation, G_r [CHAR60]. Some percent of these radicals, F , will actually form polymer chains while the remainder will recombine with other radicals to terminate polymerization. Thus, in the polymerization of thermoplastic monomers by free radical mechanisms, an estimate for D_c can be made by:

$$D_c = \left[\left(\frac{X}{F} \right) \cdot \left(\frac{N_0}{M_w} \right) \right] \cdot \frac{1}{G_r} \quad (4.19)$$

where M_w is the weight-average molecular weight of the polymer after conversion.

Adjusting for units, this expression becomes:

$$D_c = \frac{9.65 \cdot 10^{11} \cdot X}{F \cdot M_w \cdot G_r} \quad (4.20)$$

where D_p is in rads, M_w is in grams, and G_r is in radicals per 100 eV.

Substituting Equation 4.20 into Equation 4.18 and solving for y yields:

$$y(z) = r_b \cdot \sqrt{-\ln \left[\left(\frac{9.65 \cdot 10^{11}}{100 \cdot \sqrt{\pi}} \right) \cdot \left(\frac{V_s \cdot X \cdot e}{S_a \cdot J_a \left(\frac{\rho \cdot z}{r_a} \right) \cdot j_{\max} \cdot r_b \cdot G_r \cdot M_w \cdot F} \right) \right]} \quad (4.21)$$

4.2. Experimental Setup and Design

As shown above, the initial process model involved four processing parameters and seven material parameters. The beam parameters were: 1) beam diameter; 2) beam current; 3) beam scanning speed; and 4) electron energy. A fifth processing parameter, important for layering the monomer vapor, was partial pressure within the specimen chamber. The material used within this investigation was styrene which forms a thermoplastic polymer. Therefore, the material parameters needed for this investigation included: 1) monomer density; 2) electron stopping power (energy absorption coefficient); 3) electron range; 4) weight-average molecular weight of the resulting polymer; 5) G-value for radical formation; 6) percent conversion for solidification; and 7) percent radicals forming chains.

As suggested above, several parameters were found to be important from a materials viewpoint. Most important is the radiation sensitivity represented by the G-value for radical formation. Because of its high radiation sensitivity, low cost, and wide availability, styrene was chosen as the material system for the preliminary investigation. In addition, much radiation polymerization research has been conducted using styrene resulting in a large base of literature from which to extract material data including those parameters specified above.

Using the model developed above and material data for a styrene monomer system, a sensitivity analysis was performed to determine the ranges required for the various electron beam parameters. These ranges were needed to identify an appropriate EB device

for conducting the experiment. For specifying EB device requirements, the most important parameters were found to be the beam current and the scan speed since these parameters directly control the exposure dose. Other parameters, such as beam diameter, electron energy, and partial pressure, while important in determining the final shape of the interaction volume, were found not to affect exposure dose as directly and were not considered as important for specifying EB device requirements. In general, the following values for beam current and scan speed were found to result in polymerization conditions within styrene:

- beam current = 0.1 nanoamps
- beam scan speed = 1 cm/sec

Electron energy was found to control the depth of polymerization within the styrene. Values between 5 and 25 keV were found to result in penetration depths in the range of 0.5 to 9.0 μm . Since the preliminary investigation did not consider the effects of electron scattering, it was found that beam diameter had very little influence on the expected results. However, it was desirable that the beam diameter be smaller than the dimensions of the desired voxel geometry. As such, it was determined that a voxel geometry with dimensions on the order of 0.5 micrometer would show better than an order of magnitude improvement over the resolution of existing micro-scale freeform fabrication equipment (see Chapter 2). The current, scan speed, and electron energy values specified above all fall within the parameters available within a scanning electron microscope (SEM).

Ultimately, an ESEM was chosen as the electron beam source. In addition to meeting the above parameter specifications, the ESEM is capable of processing a sample with as much as 20 torr of atmosphere. At room temperature, the vapor pressure of styrene falls below 20 torr. Thus, it was found that the ESEM could be used to condense a layer of styrene monomer from vapor onto a chilled specimen holder.

Subsequently, an experiment was designed to prove feasibility of the proposed micro-scale freeform fabrication process. Based on the simple electron energy dissipation model developed above, an experimental design was formulated involving two beam spot size settings, two electron energies, and two beam scanning speeds. Spot size was chosen because it controls both beam current and beam diameter with the diameter enlarging with the beam current. Beam current and scan speed were chosen because it directly affects exposure dose. Beam diameter was chosen because it directly affects linewidth. Electron energy was chosen because it affects linedepth. Using these three parameters, an eight-run fractional design was developed as shown in Figure 4.2. Ultimately, these three beam parameters adequately addressed all of the beam parameters within the model.

All preliminary experiments were performed at Battelle Pacific Northwest Laboratories in Richland, Washington. Specific equipment used in these experiments included the ElectroScan Model E-3 ESEM with an LaB_6 filament. Ninety-nine plus percent pure styrene supplied by Aldrich Chemical Company, Inc., was used in the experiment.

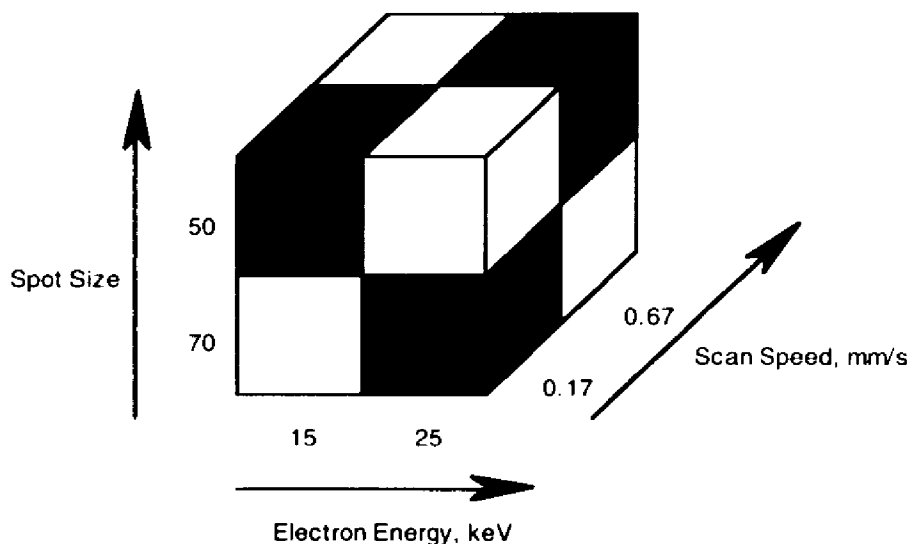


Figure 4.2. Experimental design for the preliminary investigation.

4.3. Experimental Procedure

As mentioned the objectives of the experiment were simple: prove feasibility of the proposed micro-scale freeform fabrication process. This involved three steps: 1) take a series of adjacent EB scans across the surface of the monomer forming a polymer micro-structure; 2) separate the resultant polymer micro-structure from the remaining liquid monomer; and 3) image the micro-structure.

Execution of this procedure involved two presumptions: 1) an appropriate monomer system; and 2) an EB source. For the reasons stated above, the experiment was performed using an ESEM to process liquid styrene monomer. Processing was conducted in a styrene vapor atmosphere both to allow liquid deposition of the styrene onto a chilled substrate as well as to prevent evaporation of the liquid layer once deposited. Figure 4.3

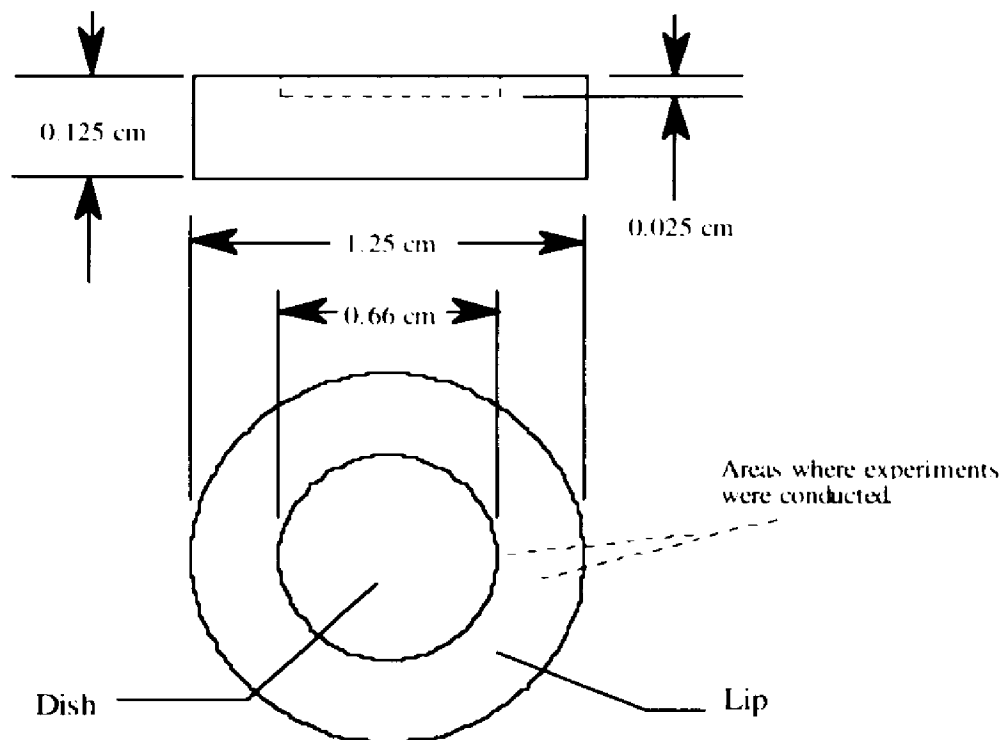


Figure 4.3. Schematic of the sample holder used in the preliminary investigation.

shows the geometry of the sample holder used within these experiments. Notice that most of the work conducted consisted of depositing and processing the liquid styrene on the lip of the sample holder.

Throughout the experiment, consultation was sought from ElectroScan in Wilmington, Massachusetts, concerning how to process and image the polymer structures fabricated. One issue involved the deposition of the liquid styrene. Initial trials were conducted by placing a sample of styrene monomer in the sample holder and processing within a water vapor atmosphere. However, it was found that the styrene would evaporate prior to exposure. Resolution involved replacing the water vapor with a styrene vapor and condensing the vapor onto a chilled sample holder. Cooling of the sample holder required the use of a Peltier (cold) stage.

To reduce the scattering of the beam within the chamber, it was necessary to minimize the chamber pressure. Consequently, the sample holder was typically cooled down to its maximum capacity (around 5 C) where the vapor pressure of styrene was about two torr. Thus, condensation and processing of the liquid styrene could be performed at low pressure.

Another issue involved controlling the beam scan speed since a specific scan speed could not be set on the ESEM. An alternative way to set the scan speed was to vary the scanning distance and time per frame. In scanning one frame, an average scan velocity for that frame can be determined by dividing the total distance traveled by the total time. Parameters for setting frame scan time are provided on the ESEM. Scanning distance can be controlled by varying the magnification which varies the field-of-view. In all, scan velocities were calculated using the following simple formula:

$$\text{fov} = (t_f * V_s) / l_f \quad (4.22)$$

where fov is the microscope field-of-view (mm/line); t_f is the frame scan time (seconds/frame); V_s is the beam scan velocity (mm/sec); and l_f is the number of lines per frame (lines/frame). The frame scan time and number of lines per frame are both

parameters which can be set on the ESEM. The fov can be controlled by the magnification. Thus, to set a specific scanning velocity at a particular combination of frame scan time and lines per frame, an fov was calculated and then used to determine the appropriate magnification.

The specific procedural steps used to perform the preliminary investigation can be found in Appendix A.

4.4. Preliminary Results

Eight runs were made in the preliminary investigation to determine the feasibility of using EB polymerization in a micro-scale freeform fabrication process. Each run involved multiple trials in which numerous adjacent scans were made over the surface of the liquid styrene to form a square polymer pad. Process feasibility was determined based on the reliability of polymer formation under different operating conditions and the precision (shape definition) of the resultant geometry. Results from the eight runs are shown in Table 4.1. Notice that insufficient data was collected for run number 6.

Table 4.1. Preliminary results showing feasibility for micro-scale EB process.

| Run* | Electron Energy (keV) | Spot Size | Scan Velocity (mm/s) | Percent of trials forming polymer | Shape Definition |
|------|-----------------------|-----------|----------------------|-----------------------------------|------------------|
| 1 | 25 | 70 | 0.1667 | 67 | best |
| 2 | 25 | 70 | 0.667 | 78 | fair |
| 3 | 25 | 50 | 0.1667 | 100 | fair |
| 4 | 25 | 50 | 0.667 | 83 | fair |
| 5 | 15 | 70 | 0.1667 | 50 | poor |
| 6 | 15 | 70 | 0.667 | - | - |
| 7 | 15 | 50 | 0.1667 | 50 | poor |
| 8 | 15 | 50 | 0.667 | - | - |

* All trials were conducted at a working distance of approximately 7 mm using a Peltier stage set for approximately 6°C inside a chamber with a partial pressure (of styrene) of approximately 2.5 torr. Sample holders were made of aluminum.

Several preliminary conclusions were drawn from these results regarding the feasibility of an EB-based micro-scale freeform fabrication process. First, the inconsistency in the process reliability was found to reflect several difficulties involved in the experimental procedure. Initial trials were plagued by insufficient saturation of the ESEM chamber with the styrene vapor. Typically, better reliability was found after the chamber had been pumped down for more than 2 hours. To remedy this problem, the vapor pressure of the styrene was raised with the use of a heating element resulting in a much shorter saturation period.

Other difficulties included depositing precise thicknesses of styrene. The condensate thickness was controlled by the temperature of the sample holder and the vapor pressure within the chamber. The procedure was found to be very sensitive to the vapor pressure setting. Essentially, once condensation had been initiated, the thickness constantly fluctuated depending upon whether the setting was left above or below the vapor pressure of the styrene. Notice that as the electron energy decreased, the reliability of the process decreased. This can be explained in large part by the fluctuation of the styrene thickness. In general, the lower the electron energy the shorter the electron penetration resulting in a shorter depth of polymerization. If the depth of polymerization does not exceed the thickness of the fluid, then the polymer formed can not attach itself to metal substrate. If the thickness of the fluid is under a constant flux, the reliability of the process is significantly undermined. This one difficulty could account for all of the reliability experienced within the preliminary investigation. Consequently, it was decided that polymer was probably formed under all circumstances, but only appeared as a solid pad in those trials where the depth of polymerization exceeded the actual thickness of the fluid deposited.

Finally, it was also interesting that the best shape definition was found to be at high electron energy, slow scan speed, and large spot size values. This is comprehensible in light of the fact that large spot size values result in smaller beam diameters. Further, to

make up for the loss of current due to a larger spot size, a slower scanning velocity was needed. Finally, the high electron energy minimized the electron scattering within the liquid layer as in typical microlithography applications.

While certain conditions were found to provide the best shape definition, few of the square pads produced were found to be satisfactory. Many of the squares were found to be defective in some way (e.g. sides not straight, uneven surface, poor corner definition). In addition, it was noted that all pads were found to be oversized with respect to the EB pattern used to form them. Both of these observations were explained by considering the backscattered electrons produced by the metal substrate. Like in microlithography, backscattered electrons can cause a proximity effect which was verified by the oversized dimensions of the square. Other explanations for the pad defects include unstable condensation thicknesses during processing and the large volumetric shrinkage which styrene undergoes during polymerization.

Subsequent to this experimental work, several attempts were made to fabricate a multi-layer microstructure by processing a liquid styrene layer on top of a pre-existing polymer pad. To improve the chances of success, the beam conditions for producing the best shape definition were used to fabricate this microstructure (i.e. 25 keV, 70 spot size, 0.1667 mm/s). Figure 4.4 shows a micrograph of a multi-layer microstructure formed by polymerizing one square pad on top of another. The bottom pad is shown jutting out from the side of the sample holder and was formed by first filling the sample holder dish to its brim and, then, patterning a square extending halfway over the edge of the sample holder. This micrograph suggests that an EB-based micro-scale freeform fabrication process is feasible.

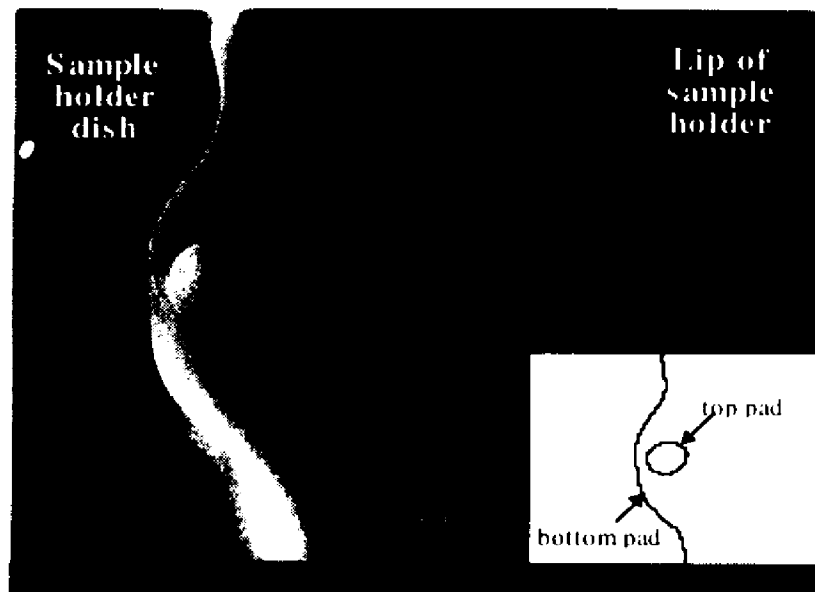


Figure 4.4. Micrograph of the multi-layer micro-structure formed during the preliminary investigation.

4.5. Preliminary Findings

Overall, the results were found to support further investigation of an EB-based micro-scale freeform fabrication process. However, because of the difficulty in controlling the thickness of the deposited monomer and the large volumetric shrinkage associated with polymerization, it was determined that the use of radiation-sensitive monomers would not work. Instead, the use of EB resists were proposed as an alternative to radiation-sensitive monomers with the major advantage being that the thickness of EB resist layers can be controlled much more precisely. Instead of condensing the material from a vapor phase as done in the preliminary investigation, it was decided that EB resist layers could be spin-coated. A new procedure was envisioned that would use repeated cycles of spin-coating and EB patterning in the formation of a multi-layer block of resist. The final step would involve the separation of the exposed and unexposed regions of the block using a chemical solvent.

In addition, it was concluded that better two-dimensional shape definition would require smaller beam sizes. Likewise, it was decided that better three-dimensional surface texture would require better voxel resolution. As suggested in Chapter 2, current micro-scale freeform fabrication technologies have voxel resolutions down to roughly 5 μm cubed. At 25 keV, the depth of polymerization is several micrometers. Thus, it was proposed that to improve the surface texture of three-dimensional objects, the electron energy would need to be reduced.

Finally, while net-shape polymer pads were formed in the preliminary investigation, a great deal of dimensional distortion was noted which was explained in large part by electron backscattering. Another advantage of low-energy EB processing is a significant reduction in the proximity effect. This is due to an overall reduction in the scattering range of the electrons as they penetrate the resist. Thus, it was concluded that low-energy EB patterning would help reduce dimensional distortion as well as help to reduce the voxel dimensions. As such, it was also concluded that a new model would be needed to better understand the effects of scattering.

5. PRIMARY INVESTIGATION

Based upon the findings of the preliminary investigation, further investigation into an EB-based micro-scale freeform fabrication process was conducted. The objectives of this investigation were to develop and validate an analytical process model incorporating low-energy electron scattering and to use the knowledge acquired from this process model in fabricating a more refined multi-layer microstructure. The model predicts the ultimate width and depth of the cured line formed by scanning a low-energy (less than 10 keV) electron beam over the surface of an electron resist. Model validation was sought by comparing model results with data from the low-energy electron microlithography literature. Further, experimental validation of the model was sought by exposing PMMA, a well-known EB resist, within the sample chamber of an environmental scanning electron microscope (ESEM). Development was conducted via agitation in a solution of methyl isobutyl ketone (MIBK) and isopropanol (IPA). This investigation is described in more detail below.

5.1. Low-Energy Electron Penetration Profile (LEEPP) Model

In order to fabricate a refined multi-layer microstructure, an analytical model was needed for predicting the voxel geometry formed by scanning a low-energy electron beam over the surface of an EB resist. Unlike the prior model, this model required the incorporation of electron scattering theories to account for the large amount of electron scattering within solids.

As mentioned in Chapter 2, several attempts have been made to analytically model the scattering behavior of collimated electrons within electron resists for the purposes of predicting electron penetration profiles [NOSK69], [GREE74], [HAWR74]. These attempts have been somewhat successful for electron energies above 10 keV. However, below 10 keV, these models have failed largely due to the fact that the electron scattering

reaches diffusion conditions within the resist. No attempts have been made to analytically model the diffusive behavior of low-energy electrons in electron resists.

Glezos, et al., [GLEZ92] have recently developed a model named LITHOS for predicting the energy dissipation function within a composite substrate using the diffusion approximation to the Boltzmann transport equation. The diffusion approximation results in a probability distribution for diffusive electron penetration over the electron range. This depth diffusion distribution represents the probability that an electron with the energy, E , can penetrate a distance, z . The depth diffusion distribution is multiplied by a conditional probability distribution for lateral electron scattering to result in a final electron density distribution. However, the model has not been applied to electron energies less than 10 keV.

Below, a model is derived for predicting the linewidth and linedepth of low-energy electron penetration profiles (LEEPP). The LEEPP model is similar to the LITHOS model in that it calculates an electron density distribution by multiplying a depth diffusion distribution by a conditional probability distribution for lateral electron scattering.

However, the models differ in six important aspects. In the LEEPP model:

1. the depth diffusion distribution is based upon Jacob's modified age diffusion theory for materials with lower atomic numbers (e.g. electron resists). This makes the model more accurate and computationally efficient;
2. the transport mean free path is calculated for non-relativistic electrons following [NOSK69]. This also makes the model more computationally efficient;
3. the material stopping power is calculated by the Bethe energy loss equation corrected by Love, et al., for low-energy electrons;
4. the electron spatial probability distribution for forward-scattering electrons is more consistent with the multiple-forward scattering literature;

5. the electron density distribution does not consider back-scattering which is more reasonable for low-energy electrons; and
6. the model does not account for solubility rates.

These differences are indicated in more detail below.

Consider a Gaussian electron-beam being scanned in a straight line at a constant velocity, V_0 , over the electron resist as shown below. As in Chapter 4, the coordinate system shown in Figure 5.1 will be adopted with the x-axis coincident with the centerline of the scanned beam. It is assumed that the absorption of electron energy within the resist follows the energy dissipation function as specified by Everhart [EVER71]. Under these conditions, the total energy dissipated per unit path length (per incident electron), $\Delta E/\Delta z$, in an absorbing material is given by:

$$\frac{\Delta E}{\Delta z} = S_{in} \cdot J(\zeta_{in}) \quad (5.1)$$

where S_{in} is the stopping power of the absorbing material estimated by using Bethe's

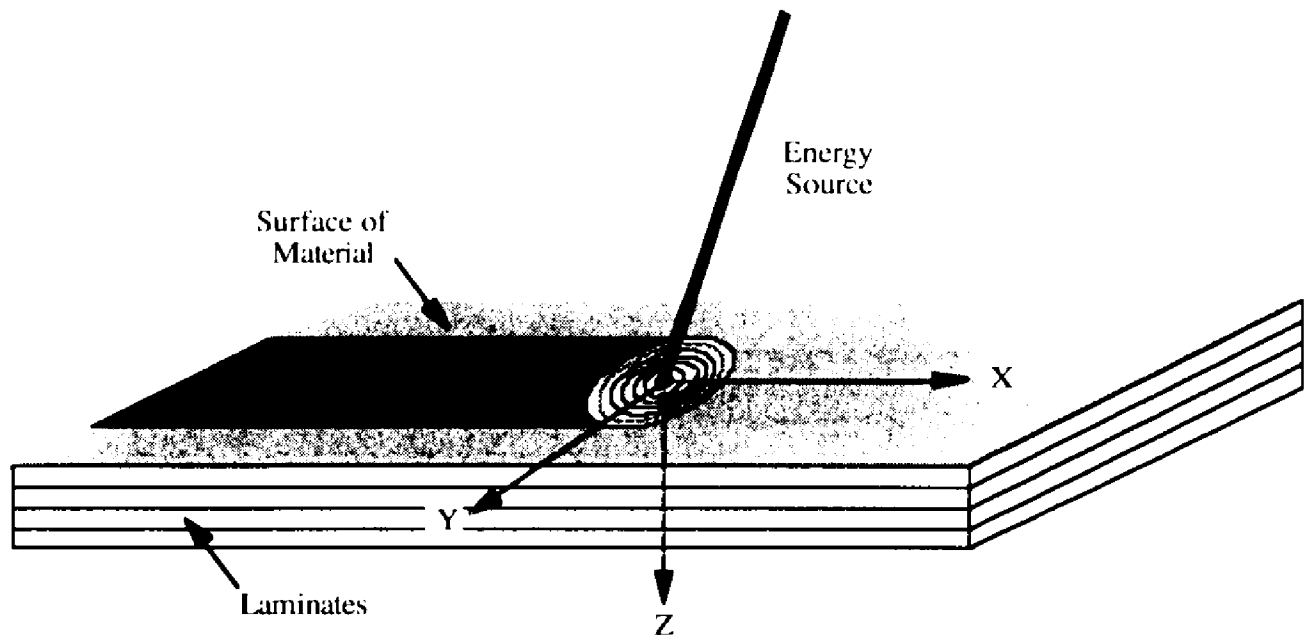


Figure 5.1. Coordinate system for the model developed in the primary investigation.

continuous slowing down approximation [BROD82] with Love's modification for low energy [LOVE78] and $J(\zeta_e)$ is the normalized energy dissipation function for electrons in low-atomic number materials as a function of the electron penetration, ζ_e , in g/cm^2 [EVER71]. An alternative method used by Glezos, et al., [GLEZ92] is to use the stopping power modification for low-energy electrons proposed by Rao-Sahib and Wittry [RAO74]. However, Love's method more precisely compensates for a multi-element target. Further, Love's modification has been found to permit exact integration with respect to energy [LOVE78] which is a requirement of the present model.

Further, consider a very fine beam (less than 100 Å diameter) normal to a homogeneous substrate. Calculation of the energy dissipation per unit volume, D , within that substrate begins by defining the spatial electron density distribution, ε , within that substrate. Thus, expanding Equation 5.1:

$$D = \varepsilon \cdot [S_e \cdot J(\zeta_e)] \quad (5.2)$$

The spatial electron density distribution can be found by the convolution integral [HAWR74], [NOSK69]:

$$\varepsilon = \int_0^\infty \int_0^{2\pi} \rho(r, z, E) \cdot N(R) \cdot R \, d\phi \, dR \quad (5.3)$$

where $\rho(r, z, E)$ is the electron probability distribution as a function of the radial distance from the incident point, r , penetration depth, z , and electron energy, E ; and $N(R)$ is the total number of incident electrons as a function of the distance from the beam center point, R . $N(R)$ can be calculated from:

$$N(R) = \int \frac{j_0}{e} \exp\left(-\frac{R^2}{R_b^2}\right) dt \quad (5.4)$$

where e is the electronic charge, j_0 is the maximum beam current density, and r_b is the Gaussian halfwidth beam radius.

Proximity effects, which are due to electron backscattering, are minimized when using a low-energy electron beam (less than 10 keV) due to a reduced scattering range [RADZ92], [SUGI88], [MCCO92]. Thus, it is assumed that the major source of lateral spreading is due to forward scattering. This assumption simplifies the model which should result in an improvement in processing time.

Following Glezos, et al. [GLEZ92], the forward scattering electron probability density function can be calculated by distinguishing two parts:

$$\rho(r, z, E) = \rho(z, E) \cdot \rho(r/z, E) \quad (5.5)$$

where $\rho(z, E)$ is the planar electron probability density (depth diffusion distribution) of finding an electron having penetrated a depth z with an energy E and $\rho(r/z, E)$ is the correlated probability density of finding an electron deviated horizontally by r given that it is found in depth z of the sample having energy E and belonging to the primary (forward scattered) part of the beam.

For a beam which dissipates all energy within a substrate (such as in micro-scale freeform fabrication applications), modeling must account for diffusive electron scattering [COSS64]. Age diffusion theory [BETH38] can be used to calculate the electron probability distribution, ρ , as a function of penetration depth, z , and electron energy, E [GLEZ92]. However, it has been pointed out that traditional age diffusion theory is poor for an atomic number, Z , less than 30 [JACO74]. Jacob [JACO74] modified the age diffusion theory for low Z materials at electron energies < 1 MeV. According to this reformulation, for a planar source at the resist surface:

$$\rho(z, E) = \frac{\exp\left(-\frac{z^2}{4\tau}\right)}{\sqrt{4\pi\tau}} \quad (5.6)$$

where τ is the electron age defined by Jacob [JACO74] and z is the depth of penetration.

The correlated probability density due to the primary beam, $\rho(r/z, E)$, has been determined as a function of the radial distance and penetration depth of the beam [SCOT49]:

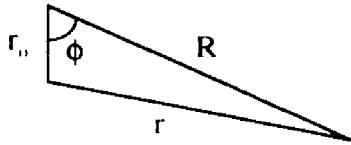
$$\rho(r/z, E) = \frac{3\lambda}{4\pi z^3} \exp\left(-\frac{3\lambda r^2}{4z^3}\right) \quad (5.7)$$

where λ is the transport mean free path of the electron as a function of electron energy, E , as defined by Nosker [NOSK69]. This form of the multiple forward-scattering model is more consistent with the literature [SCOT49], [NOSK69], [HAWR74] than that chosen by Glezos, et al., [GLEZ92]. In addition, the method chosen by Glezos for calculating the transport mean free path was originally developed for higher energy electrons [BETH38] and is more mathematically involved.

Taking the derivative of Equation 5.4 with respect to time and combining with Equations 5.3, 5.6, and 5.7, we have the electron density distribution per unit time for a stationary beam (dot response) as a function of r and z :

$$\dot{\epsilon} = \int_0^\infty \int_0^{2\pi} \frac{\exp\left(-\frac{z^2}{4\tau}\right)}{\sqrt{4\pi\tau}} \cdot \frac{3\lambda}{4\pi z^3} \exp\left(-\frac{3\lambda r^2}{4z^3}\right) \cdot \left(\frac{j_0}{e}\right) \exp\left(-\frac{R^2}{R_0^2}\right) \cdot R \, d\phi \, dR \quad (5.8)$$

where the relationship between r , R , ϕ , and r_0 (the response radius from the center of the Gaussian beam) is defined below:



where R is the radial distance of an electron from the center of the Gaussian electron beam, r is the radial distance of the incident electron scattered from the point of incidence, and r_0 is

the resultant radial distance of the incident electron from the center of the Gaussian electron beam after scattering.

For purposes of comparing Equation 5.8 with the dot response from [GLEZ92], Equation 5.8 can be reduced to:

$$\dot{\epsilon} = [\rho(z, \tau) \cdot b] \cdot \frac{J_0}{\pi e} \int_0^\infty \int_0^{2\pi} \exp(-br^2) \cdot \exp(-aR^2) \cdot R \, d\phi \, dR \quad (5.9)$$

where

$$\rho(z, \tau) = \frac{\exp\left(-\frac{z^2}{4\tau}\right)}{\sqrt{4\pi\tau}}$$

$$b = \frac{3\lambda}{4z^3}$$

$$a = \frac{1}{R_b^2}$$

In contrast, the dot response suggested by [GLEZ92] is as follows:

$$\dot{\epsilon} = [\rho(z, \sigma, \lambda) \cdot b'] \cdot \frac{J_0}{\pi e} \int_0^\infty \int_0^{2\pi} \exp(-b'r^2) \cdot \exp(-aR^2) \cdot R \, d\phi \, dR \quad (5.10)$$

where

$$\rho(z, \sigma, \lambda) = \frac{1}{\sqrt{\pi\sigma}} \exp\left(-\frac{z^2}{4\sigma^2}\right) \left\{ 1 - \frac{\sqrt{\pi\sigma}}{\Delta\lambda} \exp\left[\left(\frac{z}{2\sigma} + \frac{\sigma}{\Delta\lambda}\right)^2\right] \operatorname{erfc}\left(\frac{z}{2\sigma} + \frac{\sigma}{\Delta\lambda}\right) \right\}$$

$$b' = \frac{3\lambda}{2z^3}$$

$$a = \frac{1}{R_b^2}$$

Glezos used the original age diffusion theory developed by Bethe where σ is the square root of the original Bethe diffusion age (i.e. $\sigma^2 = \int \alpha(E) \, dE$) and

$$\alpha(E) = \frac{\lambda}{3} \left(\frac{dE}{dz}\right)^{-1} \quad (5.11)$$

In comparing the dot responses from the LEEPP model developed above (Equation 5.9) and the LITHOS model (Equation 5.10), differences are found in the ρ and b or b' terms. The greater difference lies in the ρ terms (the planar electron probability densities) which are based upon age diffusion theory. The ρ term developed in the LEEPP model is based upon the modified age diffusion theory specified by Jacob [JACO74]. The advantage of this approach is that it permits more accurate modeling of low atomic number materials such as electron resists. In addition, use of the modified age diffusion theory results in computational advantages. A comparison of the computational differences in these models can be found in Section 5.3.

Continuing with the LEEPP model development, Equation 5.8 can be solved and converted from polar coordinates to Cartesian coordinates (i.e. $r_0^2 = x^2 + y^2$):

$$\dot{\epsilon} = \left[\frac{j_0}{e} \cdot \frac{\exp\left(\frac{-z^2}{4\tau}\right)}{\sqrt{4\pi\tau}} \cdot \frac{b \cdot \exp[-b \cdot (x^2 + y^2)]}{(a+b)} \right] \cdot \left[1 + \frac{1}{\sqrt{\pi}} \cdot \int_0^\pi \exp\left[\frac{b^2 \cdot (x^2 + y^2) \cdot \cos^2(\phi)}{a+b}\right] \cdot \operatorname{erf}\left(\frac{\sqrt{x^2 + y^2} \cdot b \cdot \cos(\phi)}{\sqrt{a+b}}\right) \cdot \left(\frac{\sqrt{x^2 + y^2} \cdot b \cdot \cos(\phi)}{\sqrt{a+b}}\right) d\phi \right] \quad (5.12)$$

Equation 5.12 is considered the dot response per unit time for a zero-radius, stationary beam. This equation can be solved numerically.

Returning to the original set of assumptions, the beam is scanned in the x direction. To determine the electron density per unit time experienced by a single point (y,z) below the surface of the resist, Equation 5.12 can be solved at various values of x while holding y and z constant and a curve can be fit for the electron density per unit time experienced by that point as follows:

$$\epsilon(x @ y, z) = C_0 + C_1x + C_2x^2 + C_3x^3 + C_4 \exp\left(-\frac{x^2}{r_b^2}\right) \quad (5.13)$$

where C_n for $n = 0$ to 4 are curve fit coefficients. Integrating this equation over time results in the electron probability density at any point (y, z) within the interaction profile resulting from a beam scan. Recognizing that $dt = dx/V_e$:

$$\epsilon(x @ y, z) = \left(\frac{1}{V_e}\right) \int C_0 + C_1x + C_2x^2 + C_3x^3 + C_4 \exp\left(-\frac{x^2}{r_b^2}\right) dx \quad (5.14)$$

Equation 5.14 is considered the line response (electron density) for a zero-radius beam being scanned over a surface. Combining this with Equation 5.2, we have the energy distribution, D :

$$D = \left[\frac{S_e \cdot J(\zeta_e)}{V_e}\right] \cdot \int C_0 + C_1x + C_2x^2 + C_3x^3 + C_4 \exp\left(-\frac{x^2}{r_b^2}\right) dx \quad (5.15)$$

Thus, by evaluating Equation 5.15 over the loci of (y, z) points at which the energy density is equal to the critical energy for dissolution, an interaction profile can be established representing the forward-scattering of the beam.

Practically, to evaluate this profile, a second curve can be fit for the energy density distribution at any depth by holding z constant:

$$D(y @ z) = K_0 + K_1y + K_2y^2 + K_3y^3 + K_4 \exp\left(-\frac{y^2}{r_b^2}\right) \quad (5.16)$$

where K_n for $n = 0$ to 4 are curve fit coefficients. By subtracting the critical energy for dissolution from the right hand side of Equation 5.16 and setting it equal to zero, the equation can be numerically solved for the root providing the linewidth, y , at depth, z . The evaluation of the linewidth over the range of penetration provides a general forward scattering profile within the resist.

5.2. Model Implementation

The model was implemented in MathCAD 5.0 Plus using an IBM PS/2 Model 57 SX. A printed copy of the model can be found in Appendix B. Overall, the model seeks to calculate the energy dosages imparted by the electron beam below the surface of the resist (the line response) and to use this line response to determine the extent to which a developer solvent will dissolve the affected resist. To accomplish this, the model is subdivided into six sections: 1) entry of input parameters; 2) calculation of material and process constants; 3) definition of the dot response; 4) calculation of the incident line response; 5) calculation of the subsurface line response; and 6) presentation of results.

Figure 5.2 summarizes the model implementation in a graphical schematic. As shown on the leftmost side of Figure 5.2, the model requires various input parameters which characterize the electron beam and material system used. These input parameters are found in the first two lines of the first page of Appendix B. The first line contains all of the material parameters for the model with the second line containing the electron beam parameters.

Material parameters used in the model consist of the molecular formula, the density, and the critical dosage for dissolution (D_c). The molecular formula is used to calculate the weighted atomic weights (A_w), weighted atomic numbers (Z_w), and weighted ionization energies (I_w) of each element within the material. For simplicity, it is assumed that all electron resists evaluated consist of carbon, hydrogen, and oxygen atoms. Thus, the molecular formula is specified by setting the variables C, H, and O to the number of atoms per molecule. The density is specified in g/cm^3 . The critical dosage for dissolution is specified in $\text{eV}/\mu\text{m}^3$.

As mentioned, electron beam parameters are specified in the second line of the first page. Parameters required include the electron accelerating voltage (E_0), one half of the Gaussian halfwidth of the beam (r_b), average beam current (i_{avg}), and line charge density

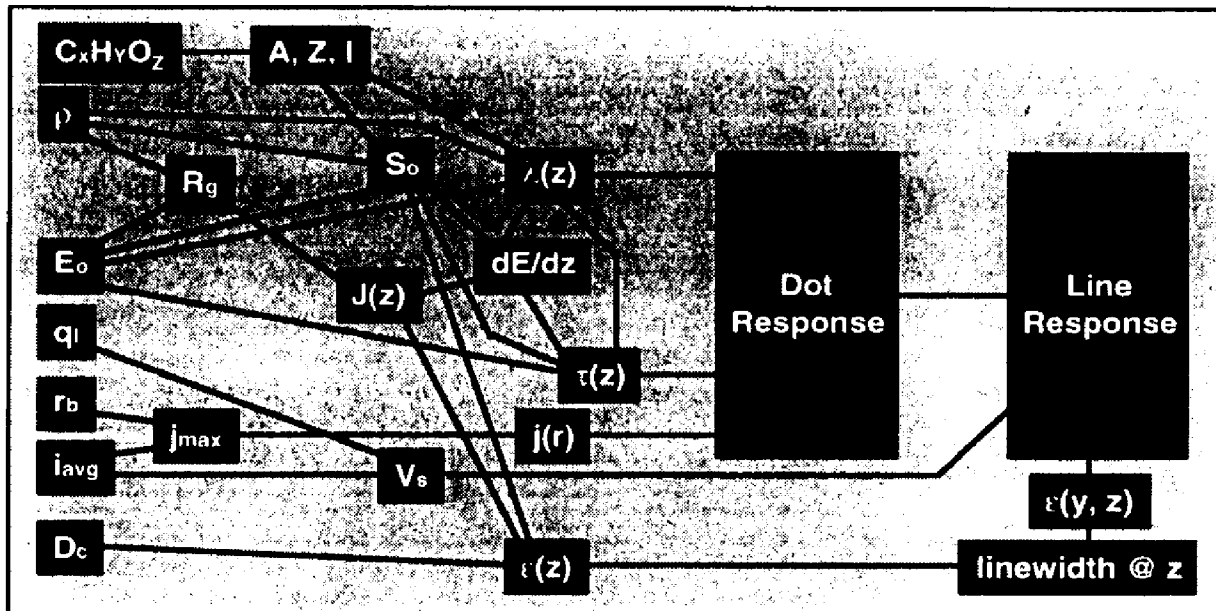


Figure 5.2. Summary of the model implementation showing the interrelationships between model parameters and variables. All input parameters are shown on the left with the result being the linewidth at each depth, z , found in the lower right.

(q_l). Electron accelerating voltage is specified in eV. The Gaussian halfwidth of the beam is defined as the point along the radius of the beam at which the electron intensity is $1/e = 36.8\%$ that of the center. One half of this value is an accepted estimate of the beam radius. This value is specified in μm . Beam current is specified in amps and line charge density is specified in coulombs/ μm . For fine beam sizes (less than $0.1 \mu\text{m}$) as used in microlithography, line charge density is used to specify the amount of exposure and is calculated by dividing the beam current by the scan velocity.

The rest of page one of Appendix B represents the section for calculating material and process constants. First the maximum current density (j_o) is calculated. This is done by calculating the average current density (j_{avg}) over the range 0 to r_b , setting this value equal to the integration of Equation 4.8 from 0 to r_b divided by r_b , and solving for j_o (j_{max}). The average current density over the range 0 to r_b is found by multiplying the average current by the percentage of the current between 0 and r_b and dividing by the area. The next set of equations are used to calculate the stopping power of the material (S) as a

function of electron energy (E) [LOVE78]. As mentioned, the molecular formula is used to calculate several weighted constants needed for calculating the stopping power. Finally, the electron range (R_g) into the material is calculated.

The second page of Appendix B is the section for defining the dot response. In order to calculate the line response within the material, the dot response, resulting from the exposure of a single electron beam spot, must first be calculated. Calculation of the dot response involves the calculation of several secondary parameters including the electron energy (E_k), transport mean free path (λ_k), and diffusion age (τ_k). The counting variable k indicates the need to calculate these parameters as a function of the penetration depth into the material (z_k). Penetration depth is represented over a discrete range of numbers bounded by the electron range (R_g). Finally, the critical electron density for dissolution ($eddc_k$) at each depth (z_k) is found by dividing the critical dosage for dissolution by the stopping power of the material at each depth [$S(E_0) \cdot J(z_k)$]. Notice that page three is simply a continuation of page two.

The fourth and fifth pages of Appendix B represent the sections for calculating the incident and subsurface line responses, respectively. Essentially, this is performed by integrating the dot response over time. The dot response is fit to a curve represented by $F(s) \cdot K$ where $F(s)$ is defined on the first page and K represents the vector of coefficients for the curve fit. After integrating this dot response curve fit over time (as time progresses Δt , the beam, scanning at velocity V_s , will move Δs so that $dt = ds/V_s$), the resultant line response is then fit to a second curve represented by $F(s) \cdot C$ where C represents the vector of coefficients for the line response curve fit. Given the line response in $F(s) \cdot C$ and the critical electron density for dissolution, $eddc$, the root can be found for the width at which the line response (at depth z) is at D_c . Solution of these widths over the range of z is stored in *Vals*. The final page presents the results in both tabular and graphical form.

Operation of the model involves mainly supplying the input parameters and recording the linedepth and widest linewidth. (The linewidth must be multiplied by a factor of 2.) Modification of values $n1$ and $n3$ on page five may be required. In general, these numbers should remain set to the values of $n1$ and $n3$. However, to make the model run faster, they may be adjusted so that line response calculations may be made over a smaller range of depths. Also, because several equations are solved using numerical methods, some modification of seed values may be required. In particular, on page five some manipulation of the seed variable s may be required before the numerical solver *root* will work in solving for *Vals*. Additional manipulation of the variable *yval* at the top of page five may be required in order for the *root* function to work in variable *radius*.

5.3. Comparison of LEEPP Model with Existing Models

As mentioned, no analytical model currently exists for modelling the diffusive behavior of low-energy electrons in electron resists. The LITHOS model developed by Glezos, et al., [GLEZ92] meets some of the requirements since it uses a diffusion approximation to the Boltzmann transport equation. However, the model has not been applied to electron energies less than 10 keV.

To further differentiate the LEEPP model from the LITHOS model, both models were implemented in the same computer environment so that the results could be contrasted. To remain consistent with the LEEPP model, only the forward-scattering portion of the LITHOS model was implemented. Tables 5.1 and 5.2 contrast some of the values calculated by the two models. These values were calculated for the following set of input parameters:

- Material: PMMA -
Chemical formula: $C_5H_8O_2$

Table 5.1. Various computed values from the computer implementation of Equation 5.9 (i.e. the LEEPP model).

| Penetration Depth (μm) | b | Planar electron density distribution, $\rho(z, \tau)$ | Dot Response, $\dot{\epsilon}$ (electrons/cm ² /s) | Linewidth (μm) |
|--|-------|--|---|--------------------------------|
| 0.05 | 8,757 | 3.304 | $6.454 \cdot 10^{10}$ | 0.148 |
| 0.075 | 2,459 | 2.512 | $4.669 \cdot 10^{10}$ | 0.148 |
| 0.1 | 975 | 2.056 | $3.465 \cdot 10^{10}$ | 0.151 |
| 0.125 | 465 | 1.752 | $2.526 \cdot 10^{10}$ | 0.159 |
| 0.15 | 249 | 1.53 | $1.78 \cdot 10^{10}$ | 0.170 |
| 0.175 | 144 | 1.354 | $1.21 \cdot 10^{10}$ | 0.186 |
| 0.2 | 89 | 1.206 | $7.996 \cdot 10^9$ | 0.217 |
| 0.225 | 57 | 1.074 | $5.179 \cdot 10^9$ | 0.241 |
| 0.25 | 38 | 0.95 | $3.307 \cdot 10^9$ | 0.264 |
| 0.275 | 26 | 0.832 | $2.089 \cdot 10^9$ | 0.284 |
| 0.3 | 18 | 0.715 | $1.304 \cdot 10^9$ | 0.293 |
| 0.325 | 13 | 0.602 | $8.041 \cdot 10^8$ | 0.281 |
| 0.35 | 9 | 0.493 | $4.882 \cdot 10^8$ | 0.239 |
| 0.375 | 7 | 0.391 | $2.911 \cdot 10^8$ | 0.118 |
| 0.4 | 5 | 0.3 | $1.7 \cdot 10^8$ | 0 |

Table 5.2. Various computed values from the computer implementation of Equation 5.10 (i.e. the LITHOS model [GLEZ92]) implemented as a part of this thesis.

| Penetration Depth, (μm) | b' | Planar electron density distribution, $\rho(z, \sigma, \lambda)$ | Dot Response, $\dot{\epsilon}$ (electrons/cm ² /s) | Linewidth, (μm) |
|---|--------|---|---|---------------------------------|
| 0.05 | 19,140 | 4.767 | $9.414 \cdot 10^{10}$ | 0.152 |
| 0.075 | 5,418 | 3.52 | $6.792 \cdot 10^{10}$ | 0.152 |
| 0.1 | 2,167 | 2.756 | $5.076 \cdot 10^{10}$ | 0.152 |
| 0.125 | 1,045 | 2.202 | $3.75 \cdot 10^{10}$ | 0.153 |
| 0.15 | 566 | 1.746 | $2.648 \cdot 10^{10}$ | 0.156 |
| 0.175 | 332 | 1.328 | $1.724 \cdot 10^{10}$ | 0.160 |
| 0.2 | 206 | 0.908 | $9.723 \cdot 10^9$ | 0.170 |
| 0.225 | 134 | 0.454 | $3.885 \cdot 10^9$ | 0.159 |
| 0.25 | 90 | -0.067 | $-4.466 \cdot 10^8$ | 0 |

| | | | |
|---|----------------------------------|----------------------|--------------------|
| | Density: | 1.1 | g/cm ³ |
| | Critical dosage for dissolution: | 0.9·10 ²² | eV/cm ³ |
| • | Processing conditions - | | |
| | Incident electron energy: | 5000 | eV |
| | Gaussian beam radius: | 0.075 | μm |
| | Average beam current: | 50 | pA |
| | Line charge density: | 0.938 | C/cm |

These conditions are representative of the experimental conditions delineated in Section 5.5 used to verify the LEEPP model.

As shown, the two models are in major disagreement concerning the resultant linewidth and linedepth. The maximum linewidth and linedepth predicted by the LEEPP model is roughly 0.6 and 0.4 μm, respectively, while the LITHOS model predicts about 0.34 and 0.225 μm, respectively. This is due to the different trends found in the dot response. While the LITHOS model begins with larger values of the dot response than the LEEPP model, the values drop much more sharply and, by one-third of the electron range, have fallen to zero. In fact, as shown, the dot response for the LITHOS model eventually becomes negative which is physically impossible. Upon investigation of the LITHOS model, the largest discrepancy between the two models came from the values of the ρ term. In the LITHOS model, the ρ term is based upon the age diffusion theory of Bethe, Rose, and Smith [BETH38]. It has been pointed out that the age diffusion theory is poor for materials with atomic numbers less than 30 [JACO74] such as electron-sensitive polymers. This has been corrected in the ρ term of the LEEPP model.

Many attempts have been made to model the diffusive behavior of low-energy electrons using Monte Carlo simulation [MCCO92], [PETE92]. However, analytical

models are typically much faster than Monte Carlo models. As reported in [GLEZ94], the LITHOS model was found to require 16 times *less* CPU time compared to a similar Monte Carlo calculation (SAMPLE 1.7a) for 10,000 electrons. As such, a computer experiment was conducted using the LEEPP and LITHOS models to determine which ran fastest. The exact same input parameters were given both models. In addition, the same number of linewidths were calculated (i.e. both were made to calculate estimated linewidths between 0.1 and 0.225 μm of penetration). The calculation time for the LEEPP and LITHOS models were 5 minutes 40 seconds and 6 minutes 30 seconds, respectively.

This result suggests that in addition to being more accurate at low-energies, the LEEPP model is roughly 15% faster than the forward-scattering portion of the LITHOS model. It is suggested that this time savings is due to the computational savings in calculating the $\rho(z,E)$ portion of the dot response. Again, since only the forward-scattering portion of the LITHOS model was implemented, this comparison was made using the same aspects of the two models. Consequently, it is expected that the LEEPP model would be faster than existing Monte Carlo simulations also.

5.4. Model Validation

Validation of the low-energy electron penetration profile (LEEPP) model was performed by comparing model results with experimental data in the form of developed profiles. Model results consisted of the maximum linewidth and linedepth from the general forward scattering profile as determined by the low-energy electron scattering model explained in the previous section. Developed profiles were found in the low-energy electron scattering literature.

Three primary sources of experimental data were found for model validation. Wolf, et al. [WOLF71], measured electron beam energy-dissipation profiles for 5, 10, 15,

and 20 keV electrons in polymethyl methacrylate (PMMA) polymer on a SiO₂-Si layered substrate. The results consist of a family of developed profiles obtained by varying the exposure dose (charge per unit length). The resist used was DuPont Elvacite 2041 with a sensitivity of 10 μC/cm² at 10 to 15 keV [WOLF71], a density of 1.2 g/cm³, and an average molecular weight of 760,000 [POSS75]. The resist thickness was 4000 Å and the estimated beam half-width at 20 keV was 125 Å [GREE74]. The developer used was a 1:3 solution of methyl-isobutyl ketone:isopropanol (MIBK:IPA). Under these conditions, several values for the critical dosage for dissolution were found in the literature. Greeneich and Van Duzer [GREE74] used a value of $0.68 \cdot 10^{22}$ eV/cm³ for Wolf's data while Kyser and Murata [KYSE74] used $1.1 \cdot 10^{22}$ eV/cm³. Possin and Norton [POSS75] derived a value of $1.5 \cdot 10^{22}$ eV/cm³ for Elvacite 2041 using 1:3 solution of MIBK:IPA as a developer. Overall, a value of $1 \cdot 10^{22}$ has been accepted as a typical value for DuPont Elvacite 2041 using MIBK:IPA as a developer [KYSE75].

In Figure 5.3, a comparison is made between the maximum linewidth of the developed profiles and the LEEPP model. Comparisons were made for 5 keV electrons over a range of line charge densities. A critical dosage of dissolution for Wolf's data was found to be roughly $1.5 \cdot 10^{22}$ eV/cm³. This value was accounted for based upon the fact that it was still within the range of values reported in the literature. In addition, the details of the development conditions were not reported. It is well known that MIBK:IPA as a developer is very time dependent [GREE74]. It is suspected that the development time was short relative to other reported experiments since a shorter development time would raise the critical dosage of dissolution thereby reducing the linewidth. This point is further supported below.

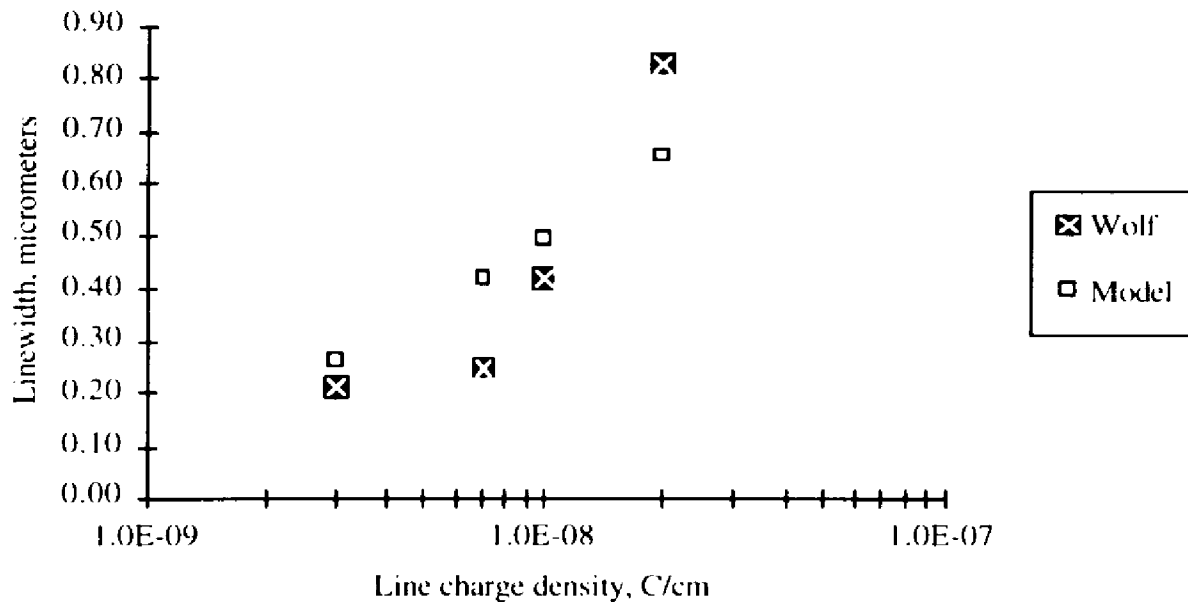


Figure 5.3. Comparison of LEEPP model linewidth results with Wolf, et al. [WOLF71], for 5 keV electrons over a range of exposure doses (line charge densities). The critical dosage for dissolution used in the model was $1.5 \cdot 10^{23}$ eV/cm².

As shown, the results are in reasonably good agreement. The average percent error for the four points in this graph is 33.5 percent. Some discrepancy between the model and Wolf's data was expected in that the profiles created by Wolf, et al. [WOLF71], were generated in 0.4 μm of resist over a Si substrate. The range of 5 keV electrons in PMMA is roughly 0.6 μm . Therefore, it is expected that electron backscattering from the substrate may have introduced additional energy resulting in larger linewidths at larger line charge densities. Other discrepancies may result from assumptions concerning how the scanning electron microscope (SEM) was operated. The lines fabricated by Wolf, et al., were made by scanning the electron beam in a dot-matrix fashion rather than continuously. In other words, the exposure lines were created by on/off blanking of an SEM beam to form a high-density sequence of spots roughly 50 \AA apart [GREE74]. This stands in contrast to the

LEEPP model above which assumes that the beam is scanned continuously over the resist surface. As such, additional data was sought for model verification.

Possin and Norton [POSS75] also investigated profile development using DuPont Elvacite 2041. Unlike Wolf, et al., Possin and Norton studied profile development solely within thick resists, thus, eliminating the influence of the substrate material. Electron energies employed were 5 and 10 keV and the estimated beam spot size was 500 to 1000 Å. Like Wolf, et al., the developer used was a 1:3 solution of MIBK:IPA.

In Figure 5.4, a comparison is made between the maximum linewidths found by Possin and Norton and the LEEPP model. As before, comparisons were made for 5 keV electrons over a range of line charge densities. A critical dosage of dissolution of $0.68 \cdot 10^{22}$ eV/cm² was used for this comparison. This is the lowest estimate of the critical dosage of dissolution for PMMA cited in the literature. Use of this value was accounted for based upon the development conditions used by Possin and Norton. Possin and Norton developed by immersing the samples for one minute and spraying for an additional 30 seconds. Recognizing that spray development is a more rapid development method than immersion development [ELLI86], this can be considered a long development time. Many developments of PMMA using MIBK:IPA cited in the literature involve immersion development conditions of one minute and shorter [MCCO92], [PETE92]. Longer development times would tend to decrease the critical dosage for dissolution.

Again, as shown in Figure 5.4, results are in good agreement. The average percent error for the four points in this graph is 22.2 percent. It is observed that while the model predicts the trend in linewidth adequately, it consistently predicts linewidths smaller than the literature data. This may be due to two reasons. First, the value for the critical dosage for dissolution, $0.68 \cdot 10^{21}$ eV/cm², was arbitrarily assigned based on values found in the literature. It was assigned simply because the development conditions favored a smaller critical dosage value and it was the smallest value reported in the literature. By decreasing

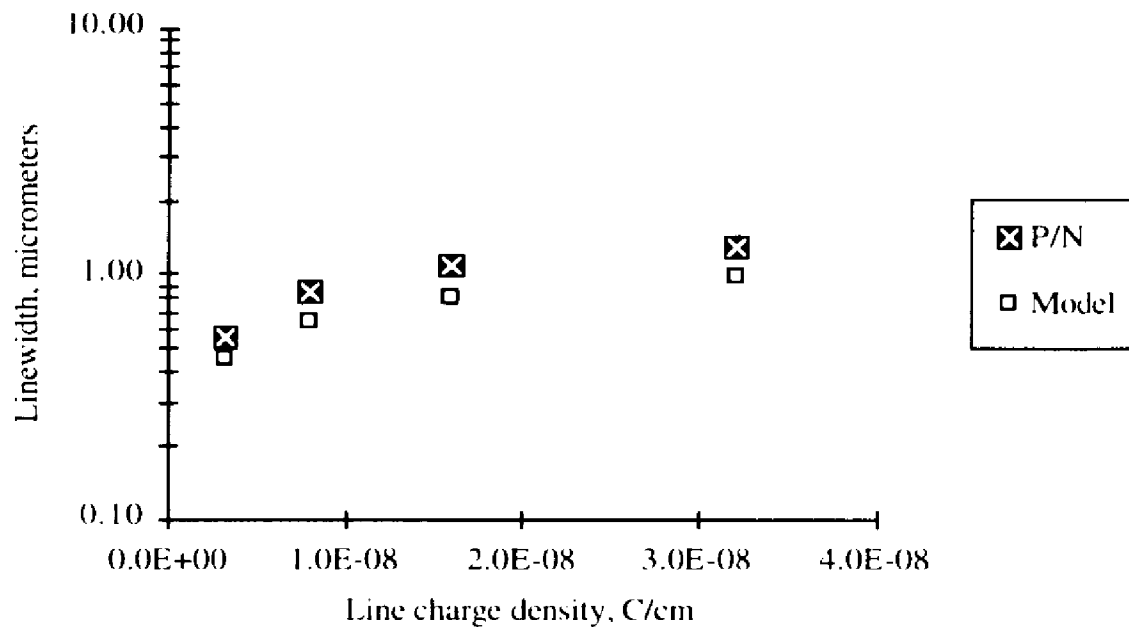


Figure 5.4. Comparison of LEEPP model linewidth results with Possin and Norton, 1975 for 5 keV electrons over a range of exposure doses (line charge densities). The critical dosage for dissolution used in the model was $0.68 \cdot 10^{22}$ eV/cm³.

this value less than $0.1 \cdot 10^{21}$ eV/cm³, the trends could be made to coincide. Second, the beam halfwidth for this data was estimated to be 500 to 1000 Å, 5 to 10 times larger than that reported in the general microlithography literature. This might suggest that the beam is not actually Gaussian, making the Gaussian assumption in the model invalid. As will be shown in the next section, the Gaussian assumption can have a significant effect on the reliability of the model.

Investigation of these two sets of data revealed that large discrepancies exist between the values being used in the literature for the critical dosage for dissolution. As mentioned, Greeneich and Van Duzer [GREE74] used a value of $0.68 \cdot 10^{22}$ eV/cm³ for Wolf's data while Possin and Norton [POSS75] used a value of $1.5 \cdot 10^{22}$ eV/cm³ for their data. However, the data collected by Possin and Norton would suggest that their critical

dosage of dissolution should be *less*. Within the line response of a resist, the dosages become smaller farther away from the centerline. Thus, since Possin and Norton used the same material under similar exposure conditions and Possin and Norton's linewidths are significantly larger, it would seem only reasonable that the critical dosage predicted would be smaller. Yet, Possin and Norton's critical dosages are *larger* than Greeneich and Van Duzer. Such discrepancies lend further credibility to the LEEPP model since it has been able to reconcile these differences by using different critical dosages. Because of these discrepancies, further validation was sought.

Sugita and Tamamura [SUGI88] studied the resist exposure characteristics of focused low-energy electron beams by exposing phenylmethacrylate-methacrylic acid (ϕ -MAC) copolymer using a high resolution, computer-controlled SEM. As before, the results consist of a family of developed profiles obtained by varying the exposure dose (charge per unit length) and the accelerating voltage. Resist thickness was 1 μm which is greater than the penetration depth of the 5 keV electrons. The beam diameter was roughly estimated to be in the range of 10-30 nm with a beam current from a LaB₆ filament in the range of 1-10 pA. The developer used was diisobutylketone-dioxane at 23°C. The sensitivity of ϕ -MAC to a 20 kV exposure under these conditions is about 20 $\mu\text{C}/\text{cm}^2$ compared to 10 $\mu\text{C}/\text{cm}^2$ for Elvacite 2041 under a 10-15 kV exposure. (It was assumed that the sensitivity of the Elvacite 2041 was around 50 $\mu\text{C}/\text{cm}^2$ at 20 kV.) As such, the critical dosage for dissolution for ϕ -MAC was estimated to be roughly 2.5 times less than that for PMMA (i.e. between $6.0 \cdot 10^{21}$ and $2.7 \cdot 10^{21}$ eV/cm²).

In Figures 5.5 and 5.6, a comparison is made between the maximum linewidth and linedepth of the developed profiles and the model evaluated at a critical dosage of $6.0 \cdot 10^{21}$ eV/cm². As above, comparisons were made for 5 keV electrons over a range of line charge densities. Again, the results are in good agreement. The average percent error for doses in

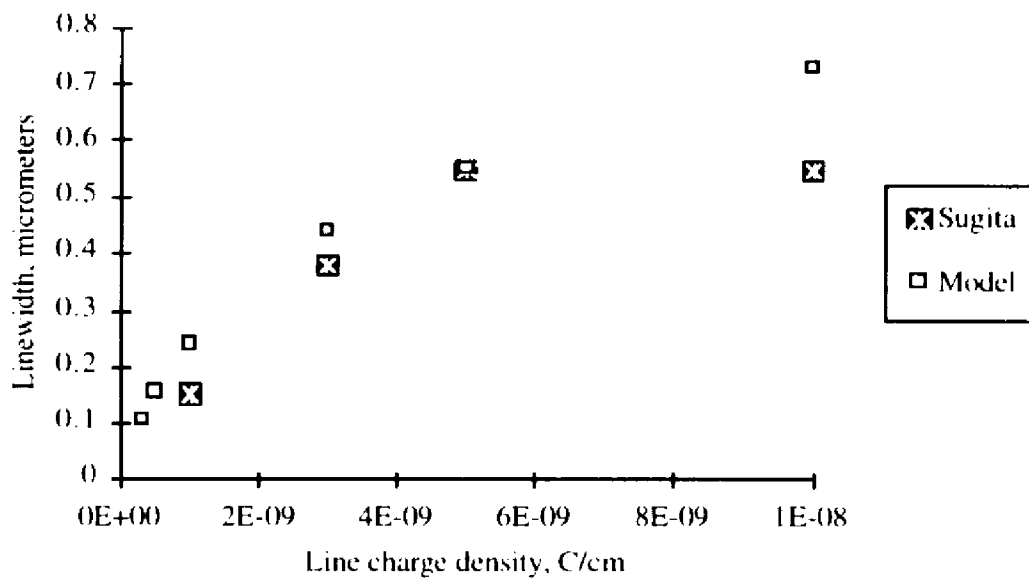


Figure 5.5. Comparison of LEEPP model linewidth results with Sugita and Tamamura [SUGI88] for 5 keV electrons over a range of exposure doses (line charge densities). The critical dosage for dissolution used in the model was $6.0 \cdot 10^{-1} \text{ eV/cm}^2$.

the range of 10^{-9} to 10^{-8} C/cm is 28.2 percent and 14.6 percent for the linewidth and linedepth, respectively.

Note that above about $5 \cdot 10^{-9} \text{ C/cm}$ in Figure 5.5 and $3 \cdot 10^{-9} \text{ C/cm}$ in Figure 5.6, the linewidth and linedepth for the literature data becomes constant. This has been attributed to the electrostatic charging of the resist by the electrons. Above these values the electrons begin repelling one another and prevent further penetration. This effect is not accounted for in the scattering model.

5.5. Experimental Setup and Design

Because of the discrepancies between the critical dosages cited in the PMMA literature, it was decided that additional experimental data needed to be collected. Such data

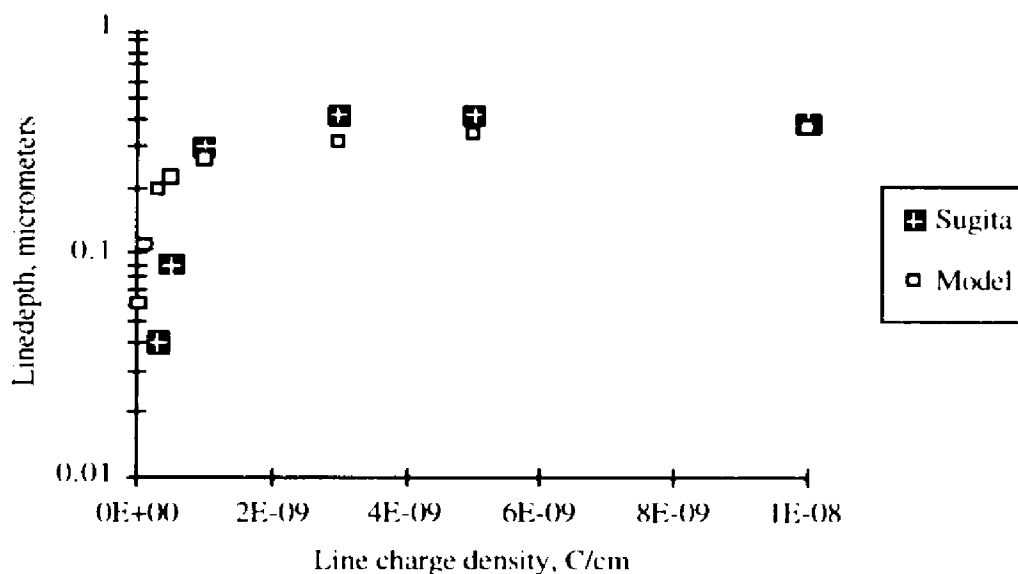


Figure 5.6. Comparison of LEEPP model linedepth results with Sugita and Tamamura [SUGI88] for 5 keV electrons over a range of exposure doses (line charge densities). The critical dosage for dissolution used in the model was $6.0 \cdot 10^{21}$ eV/cm².

could be used to determine if the reconciliatory assumptions used above were valid.

Assumptions made during model validation included:

1. Longer development times will decrease the critical dosage of dissolution which should result in larger linewidths over the range of line charge densities.
2. Non-Gaussian beam current distributions -result in greater discrepancies between the LEEPP model and experimental results.
3. Resist sensitivity can be used to relate the critical dosage of dissolution between material systems.

Thus, experimental conditions were chosen to test the validity of these assumptions.

An environmental scanning electron microscope (ESEM) was chosen to expose the resists. In addition, to its ability to operate at low accelerating voltages (5 kV) over a wide range of line charge densities, the instrument most closely resembles the conditions under

which a production-scale MicroFFED device would operate. That is, it was envisioned from the onset of this research that a production device would require a fast layering mechanism such as polymer evaporation. Such a layering mechanism would require millitorr pressures similar to those found in the ESEM. For proof-of-principle purposes during the experiment, spin coating was chosen over polymer evaporation as the layering mechanism since it was more readily available.

Experiments were designed to validate the assumptions used in model validation. All experiments involved the determination of linewidth and linedepth as a function of line charge density. An electron accelerating voltage of 5 kV was chosen in accordance with the low-voltage data available in the literature. An experimental design was initially formulated involving seven line charge densities. Based upon experiments reported in the literature, the range of line charge densities was chosen to be between $1 \cdot 10^{-9}$ and $5 \cdot 10^{-8}$ C/cm. Each line charge density was designed to be replicated four times to improve data reliability. Data collection for this initial design formed a baseline for comparing subsequent experiments involving the variation of pre-baking and development conditions.

5.6. Experimental Procedure

The objective of the experiment was simple: validate the low-energy scattering model. This involved four steps: 1) sample preparation; 2) sample exposure; 3) sample development; and 4) data collection. Sample preparation was conducted on 3 inch (7.62 cm) diameter Si wafers with a <100> orientation. Wafers were spin coated with a 4%, 6%, and 9% solids PMMA standard resist provided by Olin-Ciba Geigy ($\rho = 1.1 \text{ g/cm}^3$; $M_w = 495,000$). Spin speeds ranged from 500 to 4000 RPM for a duration of 45 seconds. Samples were prepared for exposure by scratching the back of the Si wafer with a diamond scribe and cleaving the resist over a sharp corner.

Sample exposure was made using an ElectroScan Model E-3 ESEM with a Tungsten filament. All exposures were conducted at an accelerating voltage of 5 kV with a chamber pressure less than 0.1 torr. Line charge densities were varied by changing the scan velocity within the ESEM. Scan velocity was controlled by altering the beam magnification in the specimen chamber. Beam magnification controlled the speed of a mechanical stage within the specimen chamber. By change the beam from a frame scan mode to a point beam mode, the line charge density could be controlled by moving the stage under the beam. The relationship between scan velocity (V_s) and beam magnification (M) was found to be:

$$V_s = 10^{[\log(M)+4.95]} \quad (5.16)$$

where V_s is in $\mu\text{m/s}$.

Sample development was conducted in a 1:3 solution of MIBK:IPA under slight agitation for 45 seconds. After development the sample was rinsed in methanol and deionized water and allowed to air dry. Prior to imaging the resist, $\sim 100 \text{ \AA}$ of gold was deposited on the surface of the specimen to improve imaging resolution. Linewidth data was collected by imaging the specimen from the top while linedepth data was collected by imaging the profile. The profile was prepared by cleaving the wafer across the lines in a manner similar to that described in the sample preparation section [HATZ71]. Data collected for each line involved collecting three data points at three separate locations. An example of some specific procedural steps used to perform one of the primary experiments can be found in Appendix C.

6. FINDINGS

Experimental data was collected to further substantiate the validity of the low-energy electron penetration profile (LEEPP) model. The use of literature data during model validation revealed that large discrepancies exist between the values used for the critical dosage for dissolution. Use of the LEEPP model to reconcile these discrepancies was found to add credibility to the model. Thus, experiments were designed to test the assumptions made during model validation to reconcile the literature.

An initial experiment was conducted under baseline sample preparation, exposure, and development conditions. Subsequent experiments were performed to contrast variations in sample exposure and development. Final efforts were made to fabricate a multi-layer microstructure using the knowledge acquired from developing and validating the LEEPP model. Results from these experiments are discussed in more detail below.

6.1. Experimental Results

PMMA was chosen as the electron resist for the experiment. The resist was layered onto Si wafers using standard spin coating technology and exposed using an environmental scanning electron microscope (ESEM). Development was conducted in a 1:3 solution of methyl isobutyl ketone (MIBK) and isopropanol (IPA). Imaging of the line profiles was conducted in both an ESEM and a high-vacuum SEM. Three sets of seven lines were exposed, developed, and imaged for each set of conditions specified in the sections below. Each line was measured three times in three separate locations for data reliability.

6.1.1. Baseline Data

Experimental validation of the low-energy electron penetration profile (LEEPP) model was performed by comparing model linewidth and linedepth results with

experimental data. To benchmark the effects of various processing conditions on linewidth and linedepth, a baseline set of data was collected. Sample preparation involved spin coating PMMA electron resist (6% solids in chlorobenzene; $M_w = 495,000$; 1.1 g/cm^3) at 500 RPM for a duration of 45 seconds. This gave a thickness of approximately $0.7 \mu\text{m}$ which is greater than the electron range. Sample substrates were Si wafers with a $\langle 100 \rangle$ orientation. After spinning the wafers, softbaking was performed at 115°C for 45 seconds. After softbake, the wafers were subdivided into $5 \times 10 \text{ mm}$ samples by scratching the back of the wafer with a diamond scribe and breaking the wafer over a sharp edge.

Sample exposure was conducted at an accelerating voltage of 5 kV with a chamber pressure less than 0.1 torr. Seven exposure doses were selected ranging from $0.3 \cdot 10^8$ to $6.0 \cdot 10^8 \text{ C/cm}$. Beam current was measured before and after exposure using a Faraday cup attached to the side of the sample holder. Beam current was in the range of 50 pA and the distance between the sample and the secondary electron detector was approximately 0.5 to 1.0 mm (i.e. working distance was 6.0 mm). Scan distance and time were recorded after each scan to verify scan velocity. The estimated beam half-width at 5 keV was estimated to be between 0.05 and $0.1 \mu\text{m}$. Samples were not coated with a metal overlayer.

Sample development was performed by immersion for 45 seconds in a 1:3 solution of methyl-isobutyl ketone:isopropanol (MIBK:IPA). Samples were slightly agitated during immersion. Immediately following development, samples were rinsed in methanol and deionized water and allowed to air dry. To improve the sample imaging, approximately 100 \AA of gold film was deposited on the specimen surface after development. Samples were imaged in both the ESEM and a high-vacuum SEM at low accelerating voltage (less than 10 keV) to reduce material distortion. Figure 6.1 shows a micrograph of a submicrometer voxel profile imaged in the high-vacuum SEM. The bar in the micrograph represents $0.5 \mu\text{m}$.

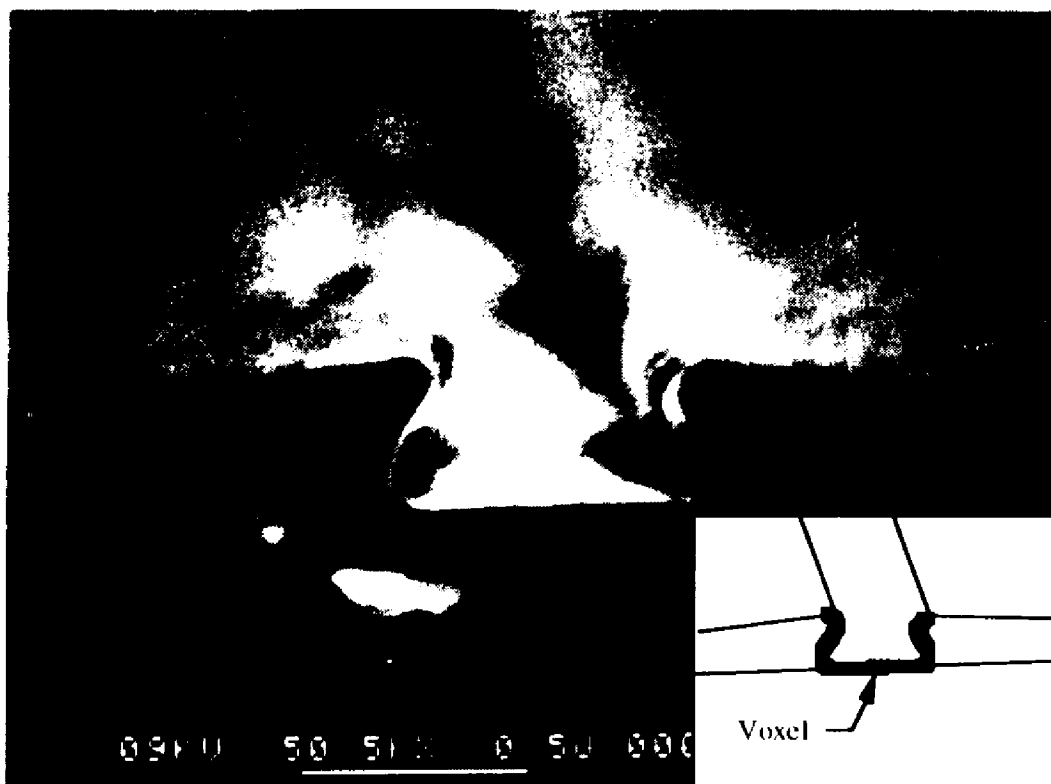


Figure 6.1. A micrograph of a voxel profile.

In Figures 6.2 and 6.3, a comparison is made between the linewidths and linedepths of the experimental profiles and the LEEPP model. A critical dosage of dissolution of $0.9 \cdot 10^{22} \text{ eV/cm}^3$ was used for this evaluation. This value was accounted for based upon Equation 2.9 which states that resist sensitivity (and thus absorbed dosage) is directly proportional to density and weakly proportional molecular weight. The density of the KTI PMMA resist was found to be 9% smaller than that for the Elvacite 2041 (1.1 g/cm^3 compared with 1.2 g/cm^3). Via Equation 2.9, the molecular weight of the KTI PMMA was found to affect the sensitivity another 1% ($M_w = 495,000$ versus $760,000$). Thus, it was assumed that the KTI PMMA was 10% less sensitive than the Elvacite 2041 which has an accepted dosage for dissolution of $1.0 \cdot 10^{22} \text{ eV/cm}^3$.

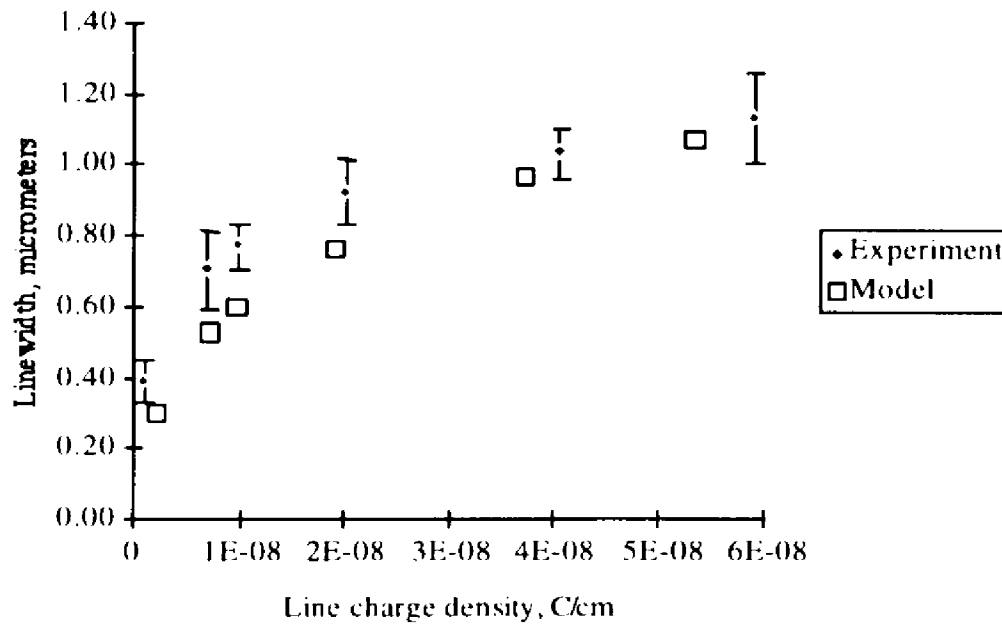


Figure 6.2. Comparison of LEEPP model linewidth with baseline experimental results for 5 keV electrons over a range of exposure doses (line charge densities). The critical dosage for dissolution used in the model was $0.9 \cdot 10^{22}$ eV/cm³.

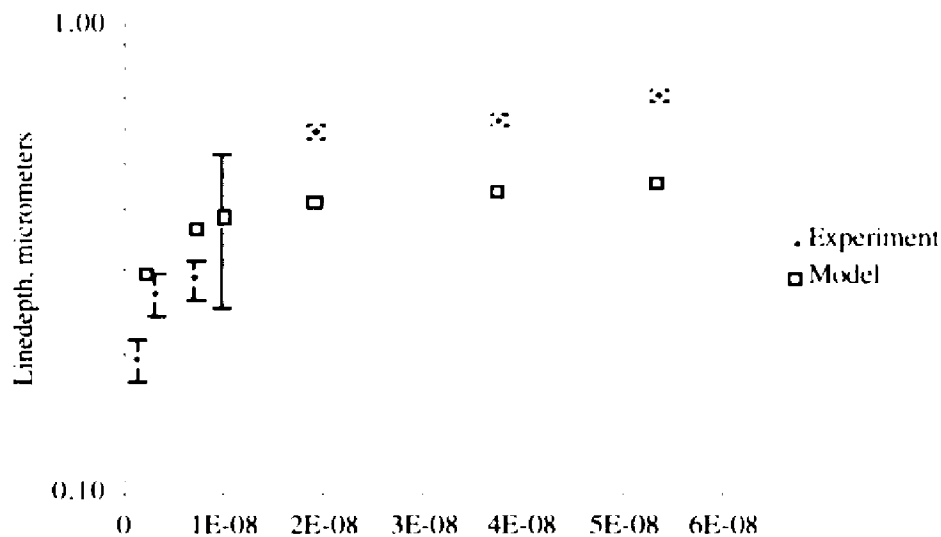


Figure 6.3. Comparison of LEEPP model linedepth with baseline experimental results for 5 keV electrons over a range of exposure doses (line charge densities). The critical dosage for dissolution used in the model was $0.9 \cdot 10^{22}$ eV/cm³.

As shown, the results are in excellent agreement providing further validation for the LEEPP model. The average percent error is 17.1 percent and 23.2 percent for the linewidth and linedepth, respectively. The experimental results for the linedepth in Figure 6.3 shows some discrepancy. This was attributed to the inconsistencies associated with collecting the linedepth data. The procedure required cleaving the sample over a sharp edge after exposure and development and then mounting the sample at the proper angle on the sample holder for imaging. These processes were found to be difficult to perform with repeated consistency. Figures 6.4 and 6.5 show some of the difficulties encountered. Figure 6.4 shows a sample profile which did not cleave cleanly. As a result, it is impossible to image the voxel geometry. Figure 6.5 shows a sample profile which was not mounted properly. Again, the voxel geometry is impossible to image. Consequently, over the course of the experimentation, less linedepth data was collected than linewidth data.

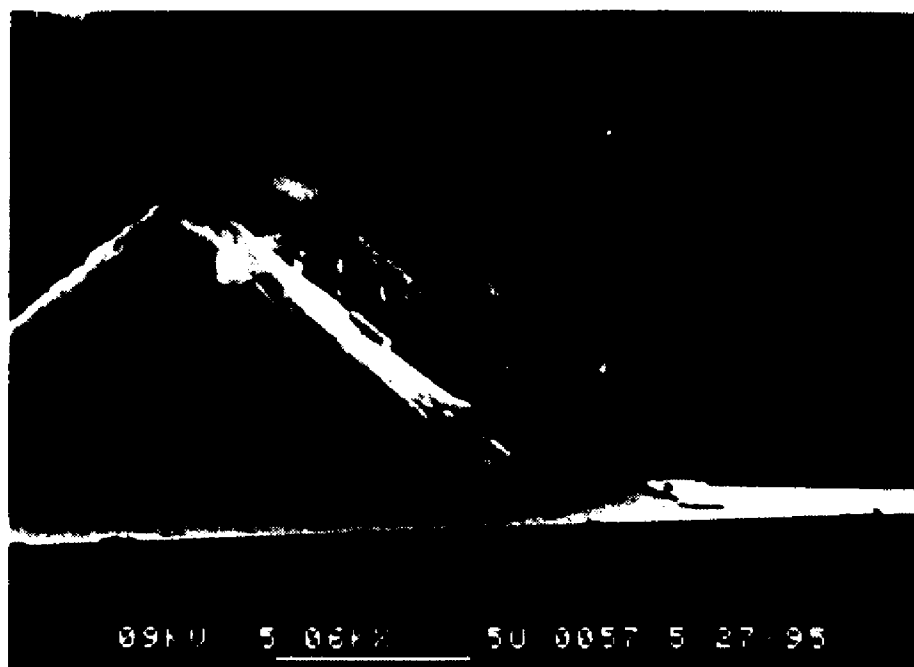


Figure 6.4. A micrograph of a sample profile showing problems encountered with cleaving the sample.



Figure 6.5. A micrograph showing problems related to improper mounting of the sample on the sample holder.

Alternatively, linewidth data was imaged from the top of the sample as shown in Figure 6.6. This procedure was found to be much simpler and permitted more consistent

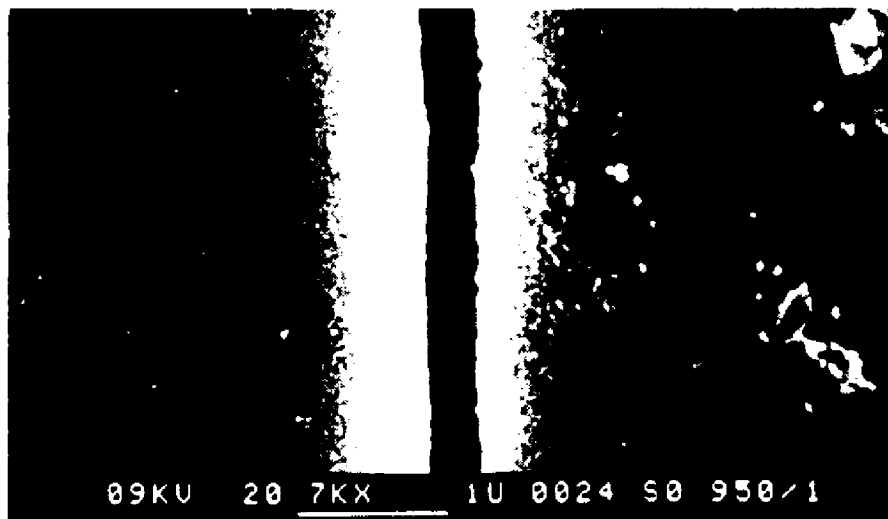


Figure 6.6. A micrograph of the top of a resist sample showing the image which was measured for collecting linewidth data.

results. Discrepancies between measuring linewidths from the profile versus the top were found to be less than 5% even with the undercutting shown in Figure 6.1. The undercutting is largely a phenomenon of electron backscattering from the Si substrate. In deeper resist, the undercutting problem was eliminated as shown in Figures 6.7 and 6.8.

One additional problem was encountered in imaging the electron penetration profiles. As shown in Figures 6.1, 6.7, and 6.8, it was virtually impossible to align the cross-section of the voxel perfectly perpendicular to the line of sight of the microscopes. As a result, it was assumed that some measurement error would be encountered due to the measurement of profile dimensions at an angle. To counter this problem, a method was established whereby the entire sample was micrographed at low magnification prior to sample imaging. Figure 6.9 is a low-magnification micrograph of a sample that has been mounted vertically on the side of a sample holder. By measuring the actual length of the sample and measuring the length of the projected resist surface via the micrograph, an estimate of the angle between the plane of the resist surface and the line of sight could be established. This angle was used to adjust for the misalignment error between the sample surface and the line of sight.



Figure 6.7. A micrograph showing the elimination of profile undercutting in thick resist.

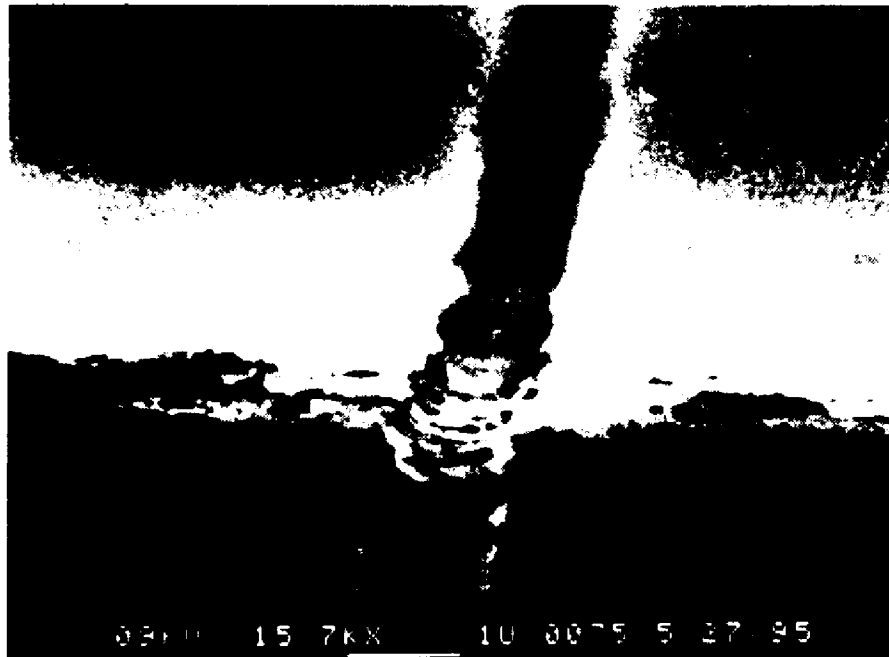


Figure 6.8. A second micrograph showing the elimination of profile undercutting in thick resist.

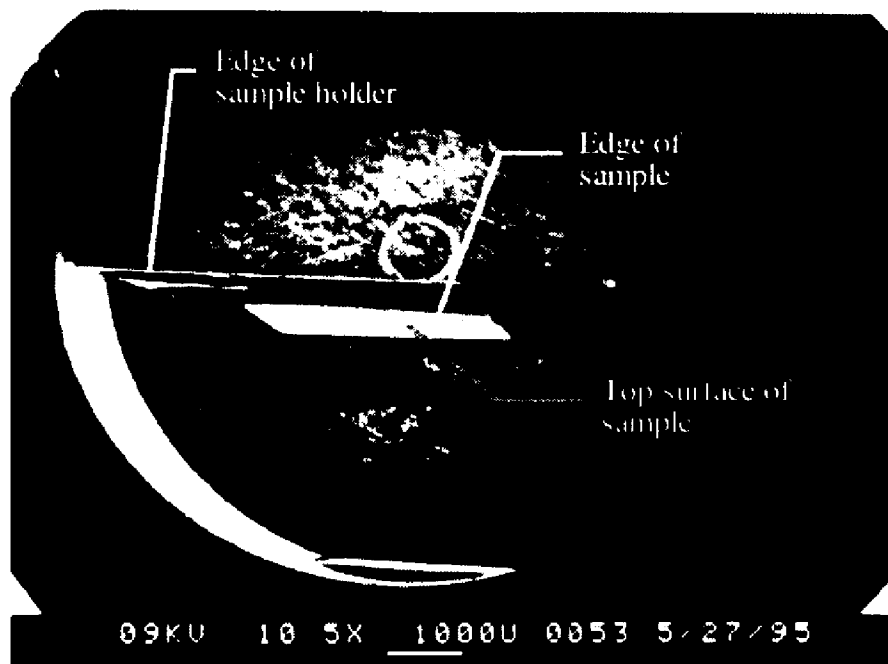


Figure 6.9. A low-magnification micrograph of sample to be imaged showing that an angle exists between the profile surface and the microscope's line-of-sight.

Other efforts were made to improve the accuracy of the data collected via micrographs. A National Bureau of Standards electron microscope standard was used to determine the magnification accuracy of the microscopes. Results showed that the high-vacuum SEM had less magnification error than the ESEM with an undersize error of less than 4%. Consequently, all remaining experimental measurements were conducted via the SEM.

One final observation concerns the effect of processing PMMA at high exposure doses. Figure 6.10 shows a line exposed at a high exposure dose. As shown, the exposed line was found to have a solid inner line of PMMA which did not dissolve in development. This phenomenon was observed in other samples at high exposure doses and was found to increase in size with increasing dosage. As reported in [GREE74], PMMA is known to act as a negative resist at high exposure doses. Thus, the inner solid line was attributed to

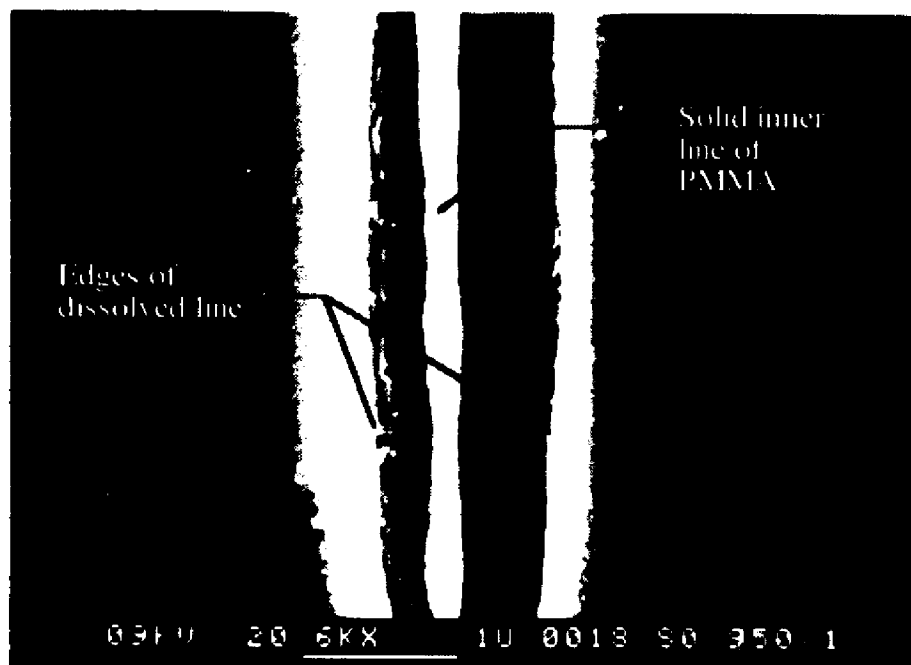


Figure 6.10. A micrograph showing the negative-resist behavior in PMMA at high exposure doses. The exposure was for a 5 keV beam incident on 0.4 micrometers of PMMA coated on a Si substrate.

cross-linking of the PMMA. Generally, the onset of this cross-linking behavior limits the exposure dose and, thus, the speed at which PMMA can be processed.

6.1.2. Development Time Effects

Additional experiments were conducted to better understand the effects of development time upon profile dimensions. For these experiments, sample preparation was the same as the baseline experiments. Resist thickness was approximately $0.7\ \mu\text{m}$. Sample exposure was also the same as the baseline experiments with the exception that three exposure doses were selected ranging from $0.7 \cdot 10^8$ to $2.0 \cdot 10^8\ \text{C/cm}$. Sample development conditions were as before with the exception that development was performed on three separate samples for 45, 75, and 105 seconds. After development, approximately $100\ \text{\AA}$ of gold film was deposited on the specimen surfaces for imaging purposes. Samples were imaged in a high-vacuum SEM at low accelerating voltage (less than 10 kV) to reduce material distortion.

In Figure 6.11, a comparison is made between the linewidths obtained from the three samples. Clearly, as reported, sample development in 1:3 MIBK:IPA is highly time-dependent. Using the LEEPP model, the critical dosages of dissolution for the 45, 75, and 105 second developments were found to be roughly 0.9 , 0.08 , and $0.01\ \text{eV/cm}^2$, respectively.

6.1.3. Chamber Pressure Effects

A final set of experiments were conducted to understand the effects of chamber pressure on voxel geometries. The relationship between chamber pressure and profile dimensions was important since it was expected that the actual implementation of the MicroFFED process would involve some level of atmosphere within the vacuum chamber.

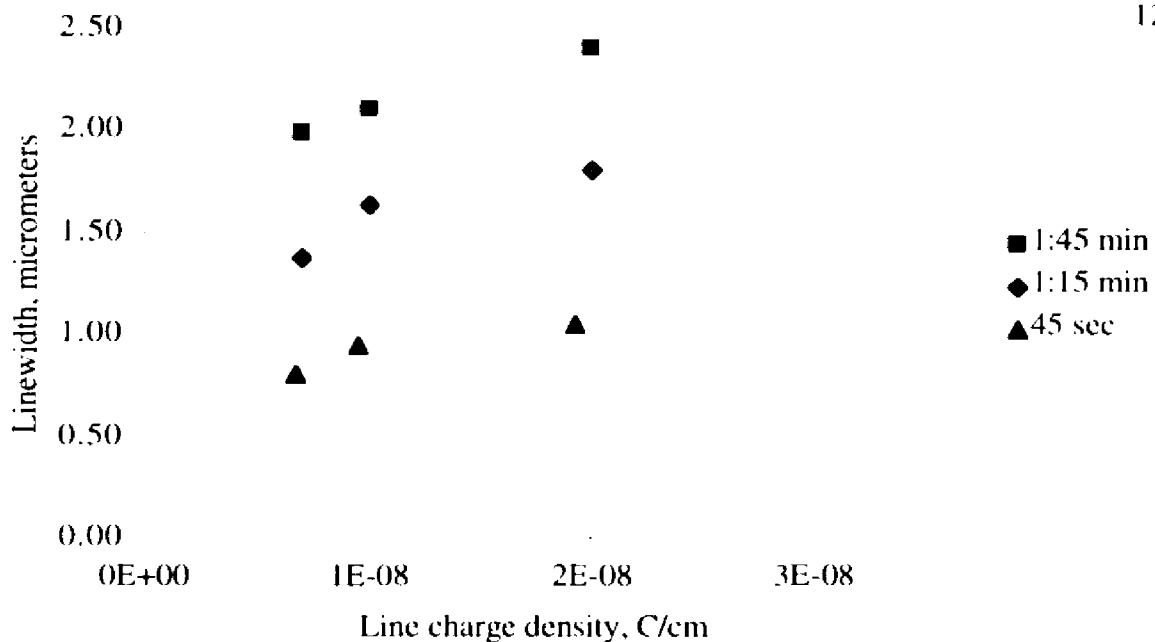


Figure 6.11. Graph showing the effect of development time on electron penetration profile dimensions. Samples were developed in a 1:3 solution of MIBK:IPA in approximately 0.7 μm of resist.

For these experiments, sample preparation and exposure conditions were the same as those used in the baseline experiments. Resist thickness was approximately 0.7 μm . Exposure doses ranged from $0.3 \cdot 10^{-8}$ to $6.0 \cdot 10^{-8}$ C/cm. Sample development conditions were as those in the baseline experiments. Sample development was performed by immersion for 45 seconds in a 1:3 solution of methyl-isobutyl ketone:isopropanol (MIBK:IPA). After development, approximately 100 Å of gold film was deposited on the specimen surfaces for imaging purposes. Samples were imaged in a high-vacuum SEM at low accelerating voltage (less than 10 kV) to reduce material distortion.

In Figure 6.12, a comparison is made between the linewidths created under different chamber pressures. As expected, the linewidths increase with increasing chamber pressure. This result is due to the increased scattering of the beam by vapor molecules as the pressure is increased. As claimed by ElectroScan, the ESEM vendor, the resultant

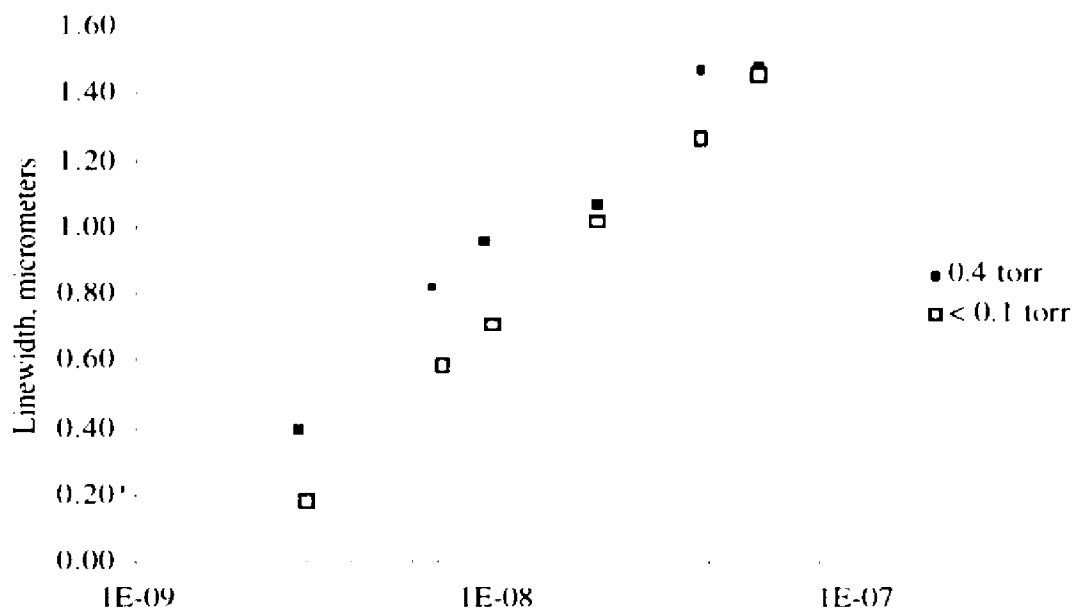


Figure 6.12. Graph showing the effect of chamber pressure on linewidth in 0.7 micrometers of PMMA resist. Preparation, exposure, and development conditions of the samples were the same.

current distribution becomes more flared as shown in Figure 6.13. The flared portion of the distribution is called the beam skirt.

6.2. Analysis of Results

As mentioned before, the above experiments were designed to justify the assumptions used in model validation. Assumptions made during model validation are restated below:

1. Longer development times will decrease the critical dosage of dissolution which should result in larger linewidths over the range of line charge densities.
2. Non-Gaussian beam current distributions result in greater discrepancies between the LEEPP model and experimental results.

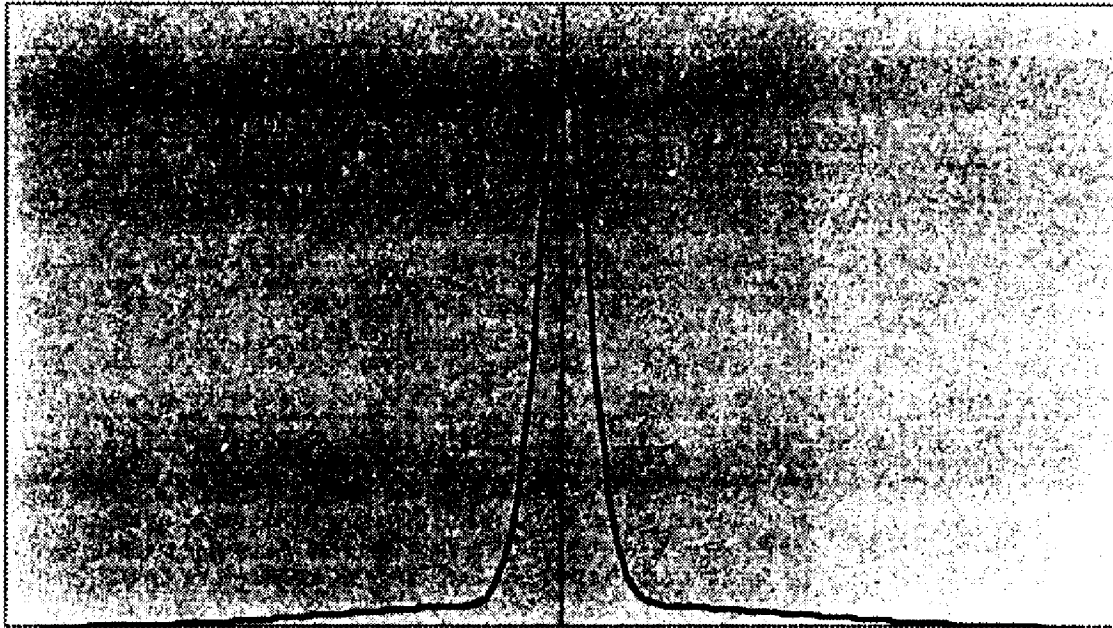


Figure 6.13. Example beam current distribution at specimen surface in typical ESEM as a result of beam scattering in the vapor environment. The flared portion at the base of the distribution is called the beam skirt.

3. Resist sensitivity can be used to relate the critical dosage of dissolution between material systems.

Clearly, resist development using a 1:3 solution of MIBK:IPA is time-dependent. To determine whether the difference in linewidth between the Wolf and Possin/Norton data could be justified by this time-dependency of development, a graph was prepared using the same scales as those used in Figure 6.11. Comparing Figure 6.14 and Figure 6.11, the magnitude of the difference in linewidth between the literature data is well within the magnitude of difference shown in Figure 6.11. This suggests that the discrepancy in data above could easily be explained by the use of different development times. Further, this graph shows that the linewidths collected by Wolf and Possin/Norton are smaller than those recorded in Figure 6.11. Given that the development time used by Possin/Norton was in the same range as that of the longest development time shown in Figure 6.11, it can

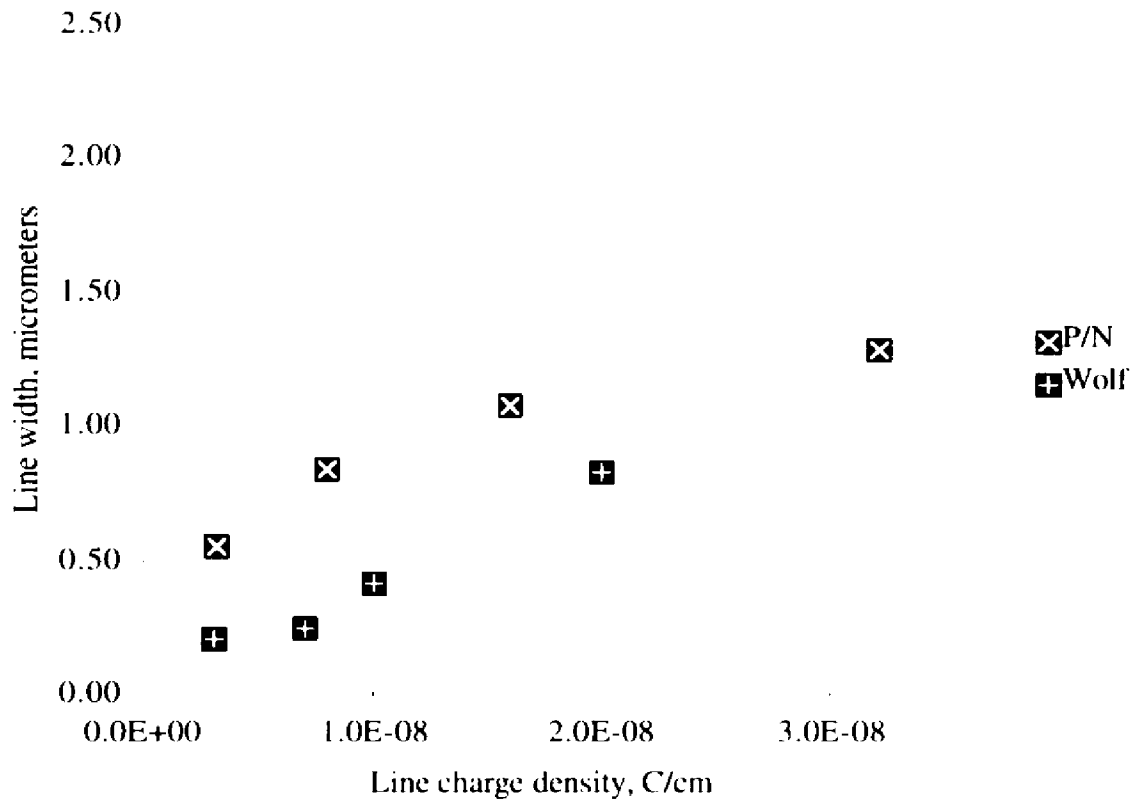


Figure 6.14. Graph showing the magnitude of difference between the data of Wolf and Possin/Norton relative to the data in Figure 6.10.

be deduced that the sensitivity of the KTI PMMA standard electron resist used in the experiments above is less than that of DuPont Elvacite 2041. In other words, the KTI PMMA requires less exposure dosage per unit linewidth. This is consistent with the fact deduced earlier that the critical dosage for dissolution for the KTI PMMA standard resist was 10% less than that of the Elvacite 2041 due to molecular weight and density differences.

Of further interest is the fact that the LEEPP model predicted nearly a two order of magnitude decrease in the critical dosage of dissolution due to the effect of development time. This is a drastic difference in the value of D_c when compared with the literature which generally accepts a value of $1.0 \cdot 10^{22}$ eV/cm³ for all PMMA resists under all

conditions. To further determine whether this range in D_c was warranted, values for the average absorbed dose based upon solubility rate calculations were compared with those found by the model.

Example calculations for the average absorbed dose are shown in Appendix D. Solubility rate calculations were adapted from the solubility rate model proposed by Kyser and Viswanathan [KYSE75]. These calculations are shown at the top of the page in Appendix D with the material constants shown on the left and an estimate of the solubility rate (SR) on the right. The constants A and B are adapted from the work of Greeneich as reported by Kyser and Viswanathan. The solubility rate is estimated by dividing the measured linedepth by the total development time. These material constants and solubility rate are then used to calculate the average absorbed dosage (E_{avg}). Calculations for E_{avg} using the LEEPP model are shown on the bottom half of the page. A line is fit to the line response experienced at the centerline of the beam scan. To get an absorbed dose equation as a function of penetration depth, the line response (in C/cm^2) is multiplied by the energy released per electron per unit penetration depth which can be calculated by multiplying the material stopping power [$S(E_0)$] by its depth dose distribution [$J(zz)$]. This absorbed dose function is then integrated over the penetration depth and divided by the change in penetration depth to acquire an average absorbed dose.

Comparison of the average absorbed dose values calculated via these two different methods are shown below in Table 6.1. Average absorbed dose values for the LEEPP model were found to be roughly twice as large as those calculated using solubility rates which is quite good considering the vastly different means by which these values were computed. Reasons for this discrepancy in average absorbed dose may lie in the modified age diffusion theory used in the LEEPP model which Jacob originally developed for materials with $Z > 13$ and the depth dose distribution which Everhart [EVER71] verified for materials with $10 < Z < 15$. While this comparison shows that the model may be

Table 6.1. A comparison of the average absorbed doses calculated using solubility rates^{1,3,3} and the LEEPP model over a range of development times.

| Development time (seconds) | Linedepth (micrometers) | Average absorbed dose calculated using solubility rates ($1 \cdot 10^{22}$ eV/cm ³) | Average absorbed dose calculated using LEEPP model ($1 \cdot 10^{22}$ eV/cm ³) |
|----------------------------|-------------------------|--|---|
| 45 | 0.5 | 4.5 | 9.6 |
| 75 | 0.6 | 4.1 | 8.0 |
| 105 | 0.65 | 3.9 | 7.4 |

overstating the energy dose distribution within the resist, the amount overstated does not account for the two order of magnitude change in D_c found in the data of Figure 6.11.

The assumption that non-Gaussian beam current distributions result in greater discrepancies between the LEEPP model and experimental results is strongly supported by Figure 6.12. All baseline data was collected with a chamber pressure less than 0.1 torr. Figure 6.12 suggests that increasing the chamber pressure results in a generally larger linewidth and, thus, a larger discrepancy with the model. Since all experimental conditions between the two experimental data sets were the same, it is likely that the increase can be attributed to changes in the chamber pressure resulting in changes to the electron beam current distribution within the ESEM.

Other chamber pressure effects were found. Figures 6.15 and 6.16 contrast two samples with identical preparation, exposure, and development conditions with the exception that the first was exposed at a chamber pressure less than 0.1 torr and the second was exposed at 0.4 torr. Notice that in the first micrograph, a series of small match-shaped residues have formed. This is due to the negative-resist behavior of the PMMA described in Section 6.1.1 above. However, what this indicates is that the energy deposition in the resist moved through cycles as the resist was exposed. The tip of the matchhead indicates the point at which the energy deposition was the greatest. Notice that the linewidth is the greatest here also. This behavior is attributed to the cyclical charging and discharging of the resist to the Si substrate underneath resulting in localized pockets of increased energy

dosage. Notice that the resist exposed at 0.4 torr does not have this residue. This is attributed to the fact that the increased amount of atmosphere (in this case water vapor) helped the charge to trickle away resulting in a smaller discharge. The end effect was that the lines exposed at higher chamber pressures tended to be straighter and less varied than the lines exposed at lower chamber pressures. Assuming a triangular distribution for the linewidths in Figures 6.15 and 6.16, the standard deviation of the line in Figure 6.15 is roughly one-half the standard deviation of the line in Figure 6.16.

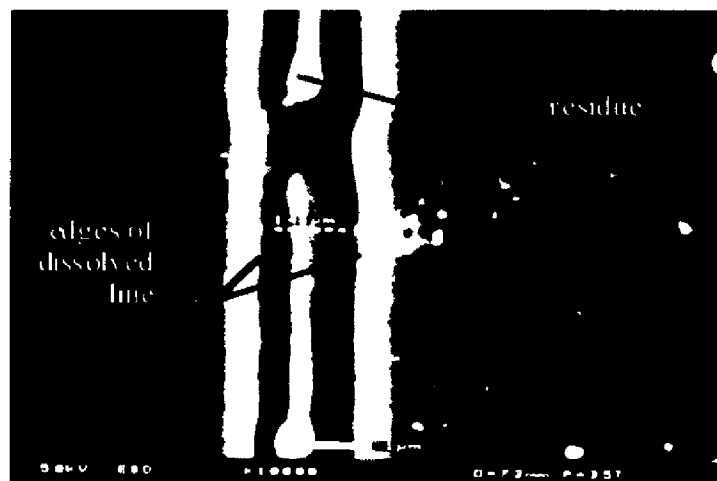


Figure 6.15. A micrograph showing the results of a sample exposed at a chamber pressure less than 0.1 torr under a high exposure dose.



Figure 6.16. A micrograph showing the results of a sample exposed at a chamber pressure setting of 0.4 torr under a high exposure dose.

The significance of these findings is that a tradeoff exists between too much and too little atmosphere. Too much atmosphere can result in unnecessary broadening of the line while too little atmosphere can result in poor precision and poor definition.

Finally, it is clear that the baseline data supports the notion that resist sensitivity can be used to relate the critical dosage of dissolution between material systems. As shown above, the value for the critical dosage for dissolution is critical to electron penetration profile prediction models. This data along with the data of Sugita and Tamamura indicates that there is a strong relationship between resist sensitivity and the critical dosage of dissolution. This is reasonable since resist sensitivities are influenced by the same set of preparation, exposure, and development conditions which affect the critical dosage of dissolution. These initial results are promising in that a method for consistently establishing the critical dosage of dissolution for new material systems does not exist.

A final observation involves the shape and size of the voxel geometry created by the MicroFFED method. Figures 6.7 and 6.8 show that the voxel geometry is much more square than the geometries generated by UV curing processes. As shown in Figure 6.17, voxel geometries generated by UV-curing processes lead to the development of stress risers on the surface of micro-mechanical parts resulting in poorer mechanical properties.

Further, Figure 6.18, shows a voxel geometry generated by the MicroFFED process with dimensions well below 1 μm in size. This is in contrast to the 5 μm voxel geometry dimensions for existing UV-based micro-scale freeform fabrication methods. Based on experience in the rapid prototyping industry, these findings imply that the surface texture and mechanical strength of devices fabricated via the MicroFFED method should surpass those of existing UV-based micro-scale freeform fabrication methods.

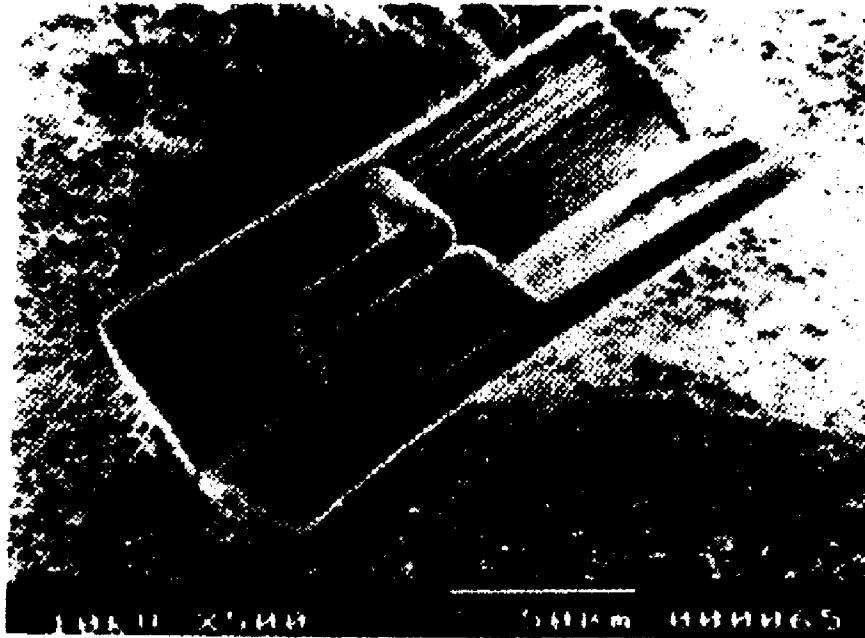


Figure 6.17. A micrograph of a UV-cured micro-mechanical part showing the potential for stress risers on the surface [IKUT94].

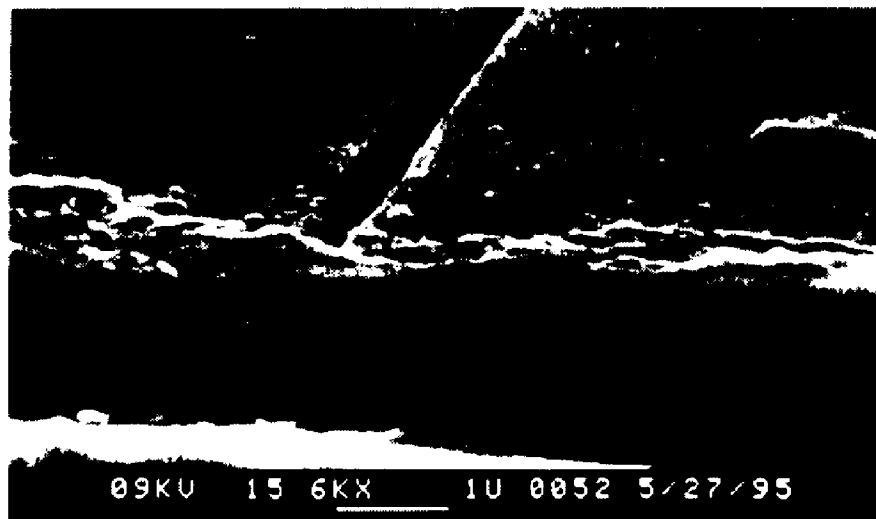


Figure 6.18. A micrograph showing EB-generated voxels with dimensions well below 1 μm .

6.3. Multi-Layer Micro-Structure

Subsequent to this experimental work, several attempts were made to fabricate a multi-layer micro-structure by successive cycles of exposure and development in a thick polymer resist layer. Exposure and development conditions were used which were known to produce small, consistent voxel geometries. Exposure was at 5 keV with a line charge density of $0.3 \cdot 10^{-8}$ C/cm and a chamber pressure of 0.4 torr. Development conditions included immersion development in a 1:3 concentration of MIBK:IPA for 45 second at room temperature.

Figure 6.19 shows a micrograph of a multi-layer microstructure formed as a result. The micrograph shows two patterns of squares which have been fabricated into the resist layer to form sub-micrometer stairsteps. Three layers are shown in the micrograph (A, B, and C). The stairsteps are roughly 0.5 micrometers in depth.

As shown in the top micrograph of Figure 6.19, the exposures were slightly misaligned. Alignment was performed by using the corner points of the specimen to locate its center. Once the center was located, five exposures were taken with one in the center and the four others centered 50 μm from the center in each direction. After development, a second set of exposures were made using the same procedure. These squares were made smaller for the purpose of fabricating stairsteps.

In fabricating the squares, it was not possible to control the precise location of each adjacent scan using the ESEM. The squares were made using the ESEM's photograph mode where the number of lines per frame is fixed. Exposure dose was controlled by considering the number of scans per voxel. For a field-of-view of 65 micrometers (≈ 2000 X magnification) in photo-scan mode (2000 scans/frame), the number of scans for a 0.5 μm voxel (created by above exposure and development conditions) was found to be:

$$0.5 / (65/2000) \approx 15 \text{ scans/voxel}$$

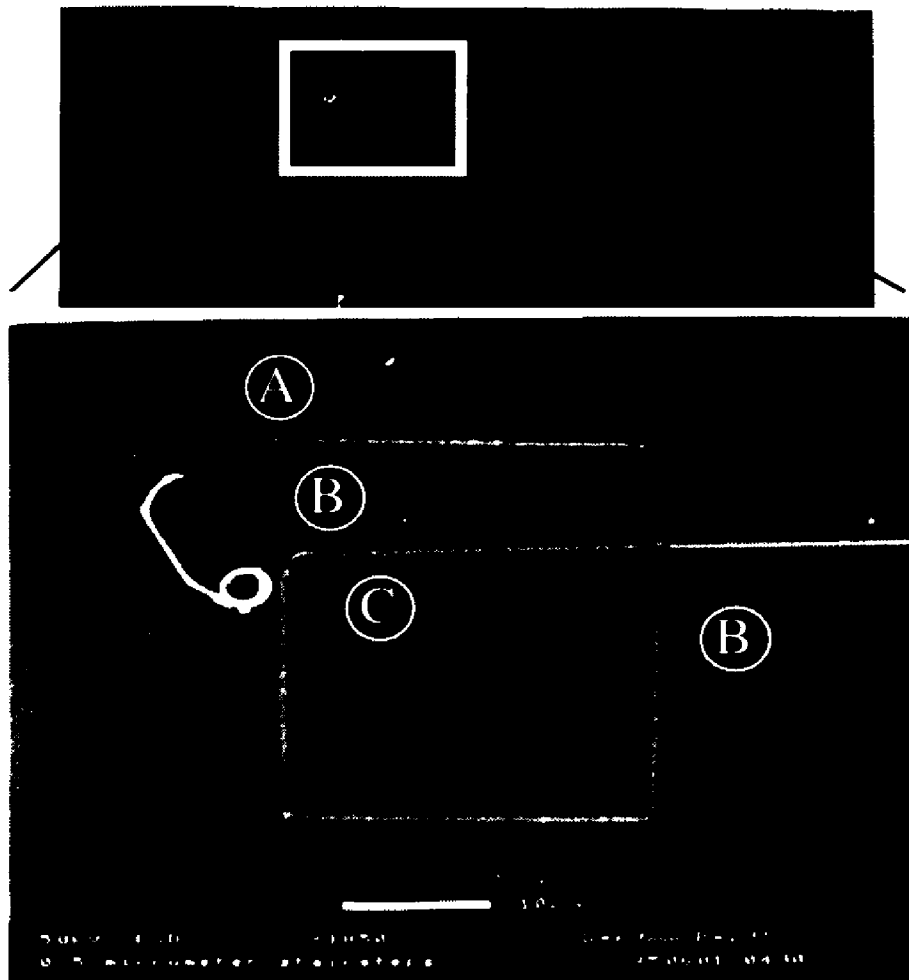


Figure 6.19. A micrograph showing $0.5\ \mu\text{m}$ stairs fabricated by the MicroFFED process. The picture shows three layers (A, B, and C) with B and C being 0.5 and $1.0\ \mu\text{m}$ deeper than A, respectively.

This suggested that to achieve a $0.3 \cdot 10^{-8}\ \text{C/cm}$ exposure dose per voxel, the required exposure dose per scan would need to be:

$$0.3 \cdot 10^{-8} / 15 \approx 0.02 \cdot 10^{-8}\ (\text{C/cm})/\text{scan}$$

As a result, the photo-scan time per frame was adjusted to provide this line charge density. With more sophisticated exposure equipment capable of exact placement of each voxel, the LEEPP model could be used to determine the distance between the centers of adjacent voxels.

A pre-assembled micro-structure could not be fabricated with this approach. However, the significance of the multi-layer micro-structure shown in Figure 6.19, should not be underestimated. This micro-structure proves that the direct application of electron-beam energy to electron resists can be used as an additive freeform fabrication method. In addition, the dimensions of Figure 6.19 prove that the dimensional resolution of this approach is an order of magnitude better than existing micro-scale freeform fabrication technologies. This micro-structure proves that this technique is capable of removing excess material within an additive freeform fabrication scheme which is an essential condition for pre-assembly. Further experiments should be conducted to show that this method meets the necessary conditions for pre-assembly: 1) that it provides easy removal of excess material; and 2) that it does not require the use of supports during fabrication.

7. SUMMARY AND CONCLUSIONS

It is anticipated that future micro-mechanical systems will consist of circuits, actuators, sensors, power sources, manipulators, end effectors, and other components all integrated onto a single chip. To achieve this sophistication, future microfabrication technologies must be capable of precision mechanical fabrication and assembly. While much progress has been made in precision micro-mechanical fabrication, current micro-mechanical assembly techniques are still very primitive. Recently, some progress has been made using single-step, *in situ* fabrication methods capable of producing non-planar, *pre-assembled* micro-structures.

At normal-scales, one fabrication method capable of producing *in situ* pre-assemblies is that of additive freeform fabrication. The object of this thesis has been to apply additive freeform fabrication principles to micro-mechanical fabrication. The approach has been to use electron beams to selectively form layers of electron resist and is called Micro-scale Freeform Fabrication using Electron-beam Degradation (MicroFFED). The expected advantages of this process over existing micro-mechanical fabrication processes include its ability to fabricate pre-assemblies and its sub-micrometer resolution leading to high aspect ratios, good surface texture, and sub-micrometer dimensional precision and repeatability.

Current micro-scale freeform fabrication techniques exist but none are capable of pre-assembly. In addition, these techniques provide limited resolution resulting in poor surface texture, dimensional accuracy, and aspect ratio. A critical issue in the development of an improved micro-scale freeform fabrication process is the control of the voxel geometry dimensions created by taking a single electron beam scan across the surface of an electron resist. Current polymer coating and microlithography models for predicting the electron penetration profile were found inadequate for the proposed process since it will operate at much lower electron accelerating voltages.

7.1. Investigations

A preliminary, proof-of-principle investigation was performed to determine the feasibility of using an electron beam and an electron-sensitive material to fabricate micro-mechanical structures. Results from this investigation found that the edge definition and ultimate resolution of the process could be improved by processing a polymer in the solid state at low electron energies.

Further investigation into an EB-based micro-scale freeform fabrication process was conducted through the process of exposing electron resist layered by spin coating methods. The objective of this investigation was to validate an analytical process model incorporating low-energy electron scattering and to use the knowledge acquired from this process model in fabricating a more refined multi-layer microstructure.

Model validation was sought by comparing model results with data from the low-energy electron microlithography literature. The use of literature data during model validation revealed that large discrepancies exist between the values used for the critical dosage for dissolution. Use of the model to reconcile these discrepancies was found to add credibility to the model. Further validation of the model was sought by exposing an EB resist within the sample chamber of an environmental scanning electron microscope (ESEM). Final efforts were made to fabricate a multi-layer microstructure using the knowledge acquired from developing and validating the model.

7.2. Conclusions

The following conclusions were reached as a result of the aforementioned investigations:

1. Low-energy electrons can be used to create voxels suitable for micro-scale freeform fabrication since they reduce the scattering range of the penetrating electrons resulting in limited proximity effects. This is evident based upon the fact that a multi-layer micro-structure was fabricated using voxels generated by low-energy electron beams. It is further evident by the size of the voxels produced in the primary investigation showing limited proximity effects.
2. The critical dosage for dissolution for the development of PMMA in 1:3 methyl isobutyl ketone:isopropanol is development-time sensitive. This is evident by the experimental results collected concerning the effect of development times.
3. The critical dosage for dissolution can be estimated for different combinations of material systems and development solvents based upon its sensitivity. This is evident based upon the three sets of literature data and one set of experimental data which were fit using resist sensitivity as an indicator of critical dosage for dissolution.
4. Width of the voxel geometry is much more sensitive to exposure dose than depth. This is evident based upon the experimental data collected in this thesis which shows that linedepth changes much less than linewidth over a wide range of exposure doses.
5. A conductive vapor can be used to effectively trickle off the electrostatic charging of the resist without the use of a metal overlayer. This is evident based upon the comparison of the linewidth variability as a function of chamber pressure.
6. Under proper conditions, the dimensional resolution of the proposed MicroFFED process exceeds that of existing micro-scale freeform

fabrication techniques. This is evident based upon the size of the voxel geometries which were produced within the primary investigation of this thesis.

7. The voxel geometry produced by the MicroFFED process is much more square than that of existing micro-scale freeform fabrication techniques. This is evident based upon the shape of the voxel geometries which were produced within the primary investigation of this thesis.

In addition to these conclusions, the following contributions have been made as a result of this research:

1. Development of a unique analytical model capable of predicting low-energy electron penetration profiles within different electron resist systems;
2. Fabrication of a multi-layer microfabrication using electron-beam degradation of electron resists; and
3. Development of a method for estimating the critical dosage for dissolution of a resist/developer system based upon resist sensitivity values.

Several additional insights have been made. The analytical model has been used to reconcile discrepancies found in the current low-energy microlithography literature. Preliminary proof-of-concept of the MicroFFED process has found several potential issues involved with its development including charging of the resist, layering of the resist, and development of the final micro-mechanical structure.

7.3. Application Potential

As mentioned elsewhere in this thesis, the application potential of a freeform micro-mechanical fabrication technology is extremely broad including fields as diverse as biomedicine, electronics, and micro-robotics. The real issue is the usefulness of the fabricating material. To this end, three ideas are submitted:

1. Since PMMA exhibits excellent optical properties, the MicroFFED technique has a large potential for application in microoptics and integrated optics. By alternating layers with materials of different indices of refraction, a planar light guide structure could be fabricated. Such a method could be useful in fabricating a microspectrometer.
2. Net-shape micro-scale powder processing techniques have been advanced for using UV-based curing processes in the binding together of sub-micrometer ceramics. Such a technique would be ideally suited for the MicroFFED process.
3. It is expected that this process could be used to fabricate integrated microelectromechanical systems (MEMS) directly from a conductive polymer.

Appendix A. EXPERIMENTAL PROCEDURE FOR THE PRELIMINARY INVESTIGATION

1. Setup ESEM

- a. Fill vacuum flask with sample. Be sure that the volume of the sample is adequate to sustain a vapor over the length of the experimental session.
- b. Remove water vapor vacuum flask from flask holder and disconnect the flask from the “wet” valve. Hook sample vacuum flask to “wet” valve.

Only do step c if the sample needs to be heated to increase the vapor pressure.

- c. Insert heating mantle into flask holder. Insert vacuum flask into heating mantle. Tape may be necessary to hold flask in place. Hook up rheostat to heating mantle. Set rheostat temperature according to the desired vapor pressure. (For styrene, a temperature of approximately 45°C worked sufficiently.)
- d. Install Peltier stage with sample holder. Sample holder is to be empty at this stage (i.e. no fluid injected yet).
- e. Evacuate the chamber using “wet” mode. If unattended, it will take the chamber over 2 hours to saturate the chamber. To accelerate saturation, increase the chamber pressure to 5 torr above the vapor pressure using the flood button. Do this 5 times to ensure that the chamber is saturated.
- f. Set working distance to about **7 mm**. (No pressure differentials beyond one aperture diameter.) Use magnification of 500x to setup the chamber.
- g. Set electron accelerating voltage and spot size. (See experimental design below for more details on accelerating voltage and spot size.)

The following parameters have been chosen to prove out the experimental setup for styrene:

- electron energy = **25 keV**
- spot size = **70**
 - beam diameter = 0.01 micrometers
 - beam current = 0.1 nanoamps

- h. Determine the magnification and scan speed needed to get the appropriate beam scan velocity by calculating the field-of-view.

$$\text{fov} = (t_f * V_s) / l_f$$

where

fov - the microscope field-of-view (mm/line)

t_f - frame scan time (seconds/frame)

V_s - beam scan velocity (mm/sec)

l_f - number of lines per frame (lines/frame)

fov will help to determine the magnification needed to get the proper field-of-view width on the screen.

The following parameters have been chosen to fabricate multi-layer structures on the order of 5 microns (fov = 5 microns). Given that the photo scan speed is set to $t_f = \mathbf{60 \text{ secs./frame}}$ at $l_f = 2000$ lines/frame):

$$V_s = (\text{fov} * l_f) / t_f = (0.005 * 2000) / 60 = 0.1667 \text{ mm/s}$$

- Magnification = _____x

- i. "Blank" the beam off of the specimen using the upper column alignment control. Click "save set" to save the blanked position.

2. Deposit Condensate

- a. Set the stage temperature to its desired value.

The following parameter has been chosen to prove out the experimental setup for styrene:

- stage temperature = **6 °C**

- b. Set chamber pressure to the vapor pressure of styrene at the above stage temperature.

The following parameter has been chosen to prove out the experimental setup for styrene:

- chamber pressure = **2.2 torr** (vapor pressure at ~6 °C)

- c. By incrementing the pressure in small steps and then lowering the pressure back to the vapor pressure, a thin film of monomer can be deposited on the surface of the sample holder. This condensation should appear as black splotches on the monitor. When the entire surface is covered with a thin layer, e.g. the whole surface has just enough monomer to turn black, the specimen is ready to be scanned. Be sure to lock in the vapor pressure so that the thickness of the condensate is not changed during the scan.

3. Conduct Trial

- a. "Blank" the beam off of the specimen by pressing "restore" in the beam alignment menu.
- b. Set photo scan rate and magnification to desired values.
- c. To create a solid plane, **activate frame scan mode**. To create a single solid line, activate line scan mode.
- d. Do the following steps simultaneously:
 - Activate "0" on upper column alignment control.
 - Click "start" on record menu.
- e. When finished, "blank" the beam to a position off of the sample.
- f. Reset the magnification to around 500x and reset the beam onto the sample by pressing "0" on the beam upper alignment column menu.
- g. Slowly evaporate the remaining condensate by lowering the chamber pressure below the vapor pressure. This should reveal the solid which was polymerized under the microscope beam.

******* This completes the procedure for one trial. *******

Continue repeating step 3 to complete the total number of experimental trials.

Appendix B. SAMPLE MATHCAD PLUS 5.0 IMPLEMENTATION OF THE LOW-ENERGY ELECTRON PENETRATION PROFILE (LEEPP) MODEL

The following model was implemented in MathCAD 5.0 Plus using an IBM PS/2 Model 57 SX. A detailed description of the model can be found in Section 5.2. A derivation of the mathematics involved can be found in Section 5.1.

Overall, the model seeks to calculate the energy dosages imparted by a low-energy electron beam (less than 10 keV) below the surface of an electron-sensitive polymer resist and to use these dosages to determine the extent to which a developer solvent will dissolve the affected resist. To accomplish this, the model is subdivided into six sections: 1) entry of input parameters; 2) calculation of material and process constants; 3) definition of the dot response; 4) calculation of the incident line response; 5) calculation of the subsurface line response; and 6) presentation of results.

The model requires various input parameters which characterize the electron beam and material system used. These input parameters are found in the first two lines of the first page of Appendix B. The first line contains all of the material parameters for the model with the second line containing the electron beam parameters. The rest of page one represents the section for calculating material and process constants.

The second page is the section for defining the dot response. Notice that page three is simply a continuance of page two. The fourth and fifth pages represent the sections for calculating the incident and subsurface line responses, respectively. The final page presents the results in both tabular and graphical form.

Operation of the model involves mainly supplying the input parameters and recording the maximum linewidth and linedepth. (The linewidth must be multiplied by a factor of 2 since only half of the line is modelled.) Modification of values $n1$ and $n3$ on page five may be required. In general, these numbers should remain set to the values of $n1$ and $n3$. However, to make the model run faster, they may be adjusted so that line response

calculations may be made over a smaller range of depths. Also, because several equations are solved using numerical methods, some modification of seed values may be required. In particular, on page five some manipulation of the seed variable s may be required before the numerical solver *root* will work in solving for *Vals*. Additional manipulation of the variable *yval* at the top of page five may be required in order for the *root* function to work in variable *radius*.

$$\begin{array}{l}
 C = 5 \quad H = 8 \quad O = 2 \quad \rho = 1.1 \quad Dc = 0.9 \cdot 10^{22} \cdot 10^{-4} \cdot 10^{-4} \\
 Eo = 5000 \quad rb = 0.075 \quad iavg = 50 \cdot 10^{-12} \quad ql = 0.938 \cdot 10^8 \cdot 10^{-4} \text{ Vs} \quad \frac{iavg}{ql} \quad Vs = 53.305
 \end{array}$$

$$j\%rb = \frac{\int_0^{rb} \exp\left(-\frac{x^2}{rb^2}\right) dx}{\int_0^{10 \cdot rb} \exp\left(-\frac{x^2}{rb^2}\right) dx} \quad javg := \frac{iavg \cdot j\%rb}{\pi \cdot rb^2} \quad jo := \frac{javg \cdot rb}{\int_0^{rb} \exp\left(-\frac{r^2}{rb^2}\right) dr}$$

$$ii = 1..3$$

$$Zw_1 := 6$$

$$Zw_2 := 1$$

$$Zw_3 := 8$$

$$Aw_1 := 12$$

$$Aw_2 := 1$$

$$Aw_3 := 32$$

$$Cw_1 := \frac{C \cdot Aw_1}{C \cdot Aw_1 + H \cdot Aw_2 + O \cdot Aw_3} \quad Cw_2 := \frac{H \cdot Aw_2}{C \cdot Aw_1 + H \cdot Aw_2 + O \cdot Aw_3} \quad Cw_3 := \frac{O \cdot Aw_3}{C \cdot Aw_1 + H \cdot Aw_2 + O \cdot Aw_3}$$

$$lw_{ii} := \frac{(13.5 \cdot Zw_{ii}) + \left[\left[9.76 + 58.8 \cdot (Zw_{ii})^{-1.19} \right] \cdot Zw_{ii} \right]}{2} \quad lp := \frac{\sum_{ii} \frac{Cw_{ii} \cdot Zw_{ii}}{Aw_{ii}} \cdot \ln(lw_{ii})}{\sum_{ii} \frac{Cw_{ii} \cdot Zw_{ii}}{Aw_{ii}}}$$

$$Rg := \frac{4 \cdot \left(\frac{Eo}{1000} \right)^{1.75}}{\rho} \cdot 10^{-2}$$

$$S(E) := \left[\left[\left(\frac{\rho}{lp} \right) \cdot \left(\sum_{ii} \frac{Cw_{ii} \cdot Zw_{ii}}{Aw_{ii}} \right) \cdot \left(\frac{1}{1.18 \cdot 10^{-5} \cdot \sqrt{\frac{E}{lp}} + 1.47 \cdot 10^{-6} \cdot \frac{E}{lp}} \right) \right] \right] \cdot 10^3 \cdot 10^{-4}$$

$$Rg = 0.608$$

$$S(Eo) = -4.939 \cdot 10^3$$

$$F(x) := \begin{bmatrix} 1 \\ x \\ x^2 \\ x^3 \\ \exp\left(-\frac{x^2}{rb^2}\right) \end{bmatrix}$$

$$ex2 := \text{floor}(\log(rb) - 0.5)$$

$$ex3 := \text{floor}\left(\log\left(\frac{jo}{c}\right)\right) - 3$$

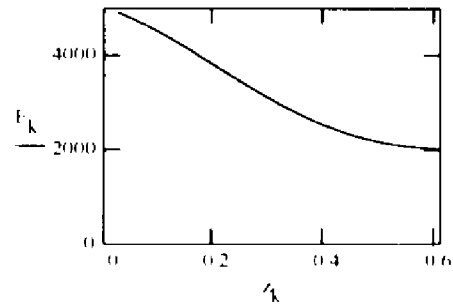
$$e := 1.602 \cdot 10^{-19}$$

$$ex1 = \text{floor}(\log(Rg) / 0.5) \quad n1 = 1 \quad res = 4 \quad n3 = \text{floor} \left(\frac{Rg}{10^{ex1}} \cdot res \right)$$

$$k = n1..n3 \quad z_k = k \cdot \frac{10^{ex1}}{res}$$

$$J(z) = 5.69 \cdot \frac{z^3}{Rg} + 12.4 \cdot \frac{z^2}{Rg} + 6.21 \cdot \frac{z}{Rg} + 0.6 \quad dE_k = S(E_0) \cdot \int_0^{z_k} J(z) dz \quad E_k := E_0 + dE_k$$

$$\lambda_k := \sum_{ii} Cw_{ii} \cdot \left[\frac{5.12 \cdot 10^{-3} \cdot (E_k)^2 \cdot Aw_{ii}}{\rho \cdot (Zw_{ii})^2 \cdot \ln \left[\frac{0.725 \cdot \sqrt{E_k}}{(Zw_{ii})^{1/3}} \right]} \right] \cdot 10^{-8} \cdot 10^4$$



$$\tau_k := \frac{1}{3} \cdot \left[\int_{E_k}^{E_0} \frac{1}{-S(E) \cdot \left[\frac{d}{dE}(S(E)) + \frac{2}{\lambda_k} \right]} dE \right]$$

$$a := \frac{1}{rb^2} \quad b_k := \frac{3 \cdot \lambda_k}{4 \cdot (z_k)^3}$$

$$\text{DotResp}(x, y, z, b, \tau) := \left[\frac{j\omega \cdot \exp\left(\frac{-z^2}{4 \cdot \tau}\right)}{\sqrt{4 \cdot \pi \cdot \tau}} \cdot \frac{b \cdot \exp[-b \cdot (x^2 + y^2)]}{(a + b)} \right] \quad \bullet \text{ (continued on next page)}$$

$$eddc_k := \frac{Dc}{-S(E_0) \cdot J(z_k)}$$

$$\int_0^\pi \operatorname{erf}\left(\frac{\sqrt{x^2 + y^2} \cdot b \cdot \cos(\phi)}{\sqrt{a+b}}\right) \cdot \left(\frac{\sqrt{x^2 + y^2} \cdot b \cdot \cos(\phi)}{\sqrt{a+b}}\right) d\phi$$

```

n = 0
yval = 2*rb

radius = root(log(jo*exp((yval)^2)/rb^2), ex3, yval)

maxy = radius*10^ex2

m1 = 0
m2 = floor(maxy/10^ex2)
m2 = if(m2 < 5, 5, 10)

j = m1..m2
y_j = j/m2*maxy

maxx_j = radius^2 - y_j^2

i = m1..m2
x_i_j = i/m2*maxx_j

delta_i_j = jo*exp((x_i_j^2 + y_j^2)/rb^2)
delta_i_j = if(delta_i_j < 0, 0, delta_i_j)

i = (m1+1)..m2
delta_i_j = if(delta_i_j < delta_{i-1,j}, 0, delta_i_j)
i = m1..m2

K^{i,j} = linfit(x^{i,j}, delta^{i,j}, F)

LineResp_j = \int_{Vs=0}^{maxx_j} F(s) * K^{i,j} ds

C := linfit(y, LineResp, F)

Vals_{n,0} := z_n

s := -.02
Vals_{n,1} := root\left[\frac{F(s) * C - \left(\frac{Dc}{-S(Eo) * J(0)}\right)}{10^{ex3}}, s\right]

Vals = (0 -0.109)

```

n1 = 2 n3 = 24

nn = n1..n3 yval = 2·rb ex3_{nn} = floor(log(DotResp(0,0,z_{nn},b_{nn},τ_{nn}))) + 2

radius_{nn} = root(log(DotResp(0,yval,z_{nn},b_{nn},τ_{nn}))) - ex3_{nn}·yval

maxy_{nn} = radius_{nn} · 10^{ex2} j = m1..m2 y_{l,nn} = $\frac{j}{m2}$ · maxy_{nn}

maxx_{l,nn} = radius_{nn}² · y_{l,nn}²

i = m1..m2 x_{l,j} = (nn - 1)·(m2 - 1) + $\frac{i}{m2}$ · maxx_{l,nn}

δ_{l,j} = (nn - 1)·(m2 - 1) + DotResp(x_{l,j},y_{l,nn},z_{nn},b_{nn},τ_{nn})

δ_{l,j} = (nn - 1)·(m2 - 1) if δ_{l,j} = 0,0,δ_{l,j} = (nn - 1)·(m2 - 1)

i = (m1 - 1)..m2

δ_{l,j} = (nn - 1)·(m2 - 1) if δ_{l,j} = δ_{l-1,j} · δ_{l-1,j} = 0,δ_{l,j} = (nn - 1)·(m2 - 1)

i = m1..m2

K_{l,j} = (nn - 1)·(m2 - 1) + linfit(x_{l,j},δ_{l,j},F)

LineResp_{j,nn} = $\int_{s=0}^{s=\maxx_{l,nn}}$ F(s) · K_{l,j}^{(nn-1)·(m2+1) + s} ds

C^{'nn'} := linfit(y^{'nn'},LineResp^{'nn'},F)

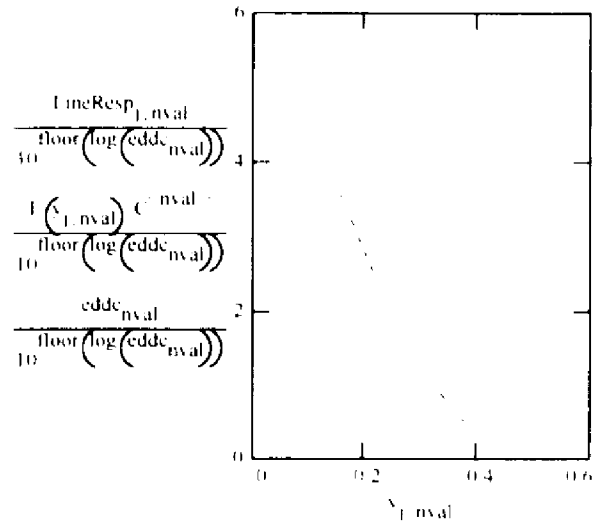
Vals_{nn,0} = z_{nn}

s := 2·rb Vals_{nn,1} := if eddc_{nn} · F(0) · C^{'nn'}, root $\left[\frac{F(s) \cdot C^{'nn'} - (eddc_{nn})}{10^{\text{floor}(\log(eddc_{nn}))}} \cdot s \right], 0 \right]}}$

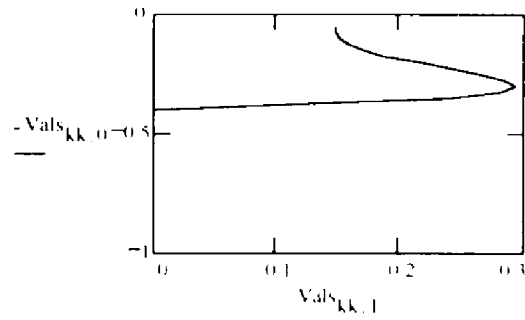
WRITEPRN(LineResp) Vals

nval 12

| | |
|-------|--------|
| 0 | -0.109 |
| 0 | 0 |
| 0.05 | 0.148 |
| 0.075 | 0.148 |
| 0.1 | 0.151 |
| 0.125 | 0.158 |
| 0.15 | 0.17 |
| 0.175 | 0.186 |
| 0.2 | 0.217 |
| 0.225 | 0.241 |
| 0.25 | 0.264 |
| 0.275 | 0.283 |
| 0.3 | 0.293 |
| 0.325 | 0.281 |
| 0.35 | 0.239 |
| 0.375 | 0.118 |
| 0.4 | 0 |
| 0.425 | 0 |
| 0.45 | 0 |
| 0.475 | 0 |
| 0.5 | 0 |
| 0.525 | 0 |
| 0.55 | 0 |
| 0.575 | 0 |
| 0.6 | 0 |



kk := n1..n3



Appendix C. SAMPLE EXPERIMENTAL PROCEDURE FOR PREPARING, EXPOSING, AND DEVELOPING LOW-ENERGY ELECTRON PENETRATION PROFILES IN ELECTRON RESIST

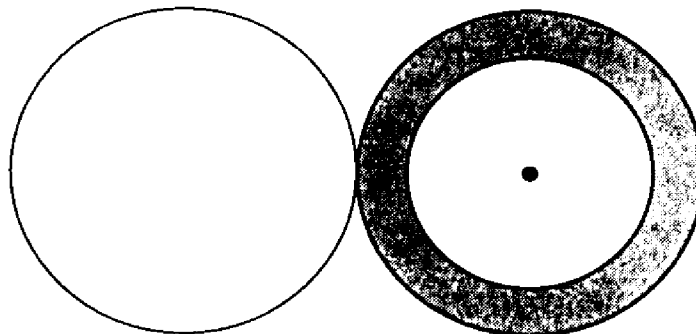
Principal Investigator: Brian K. Paul, PNL

Consultants: Dr. Robert Davis, Electronic Materials & Processing
Dr. Maria Klimkiewicz, MRL
Tom Hardt, ElectroScan

Experimental Procedure

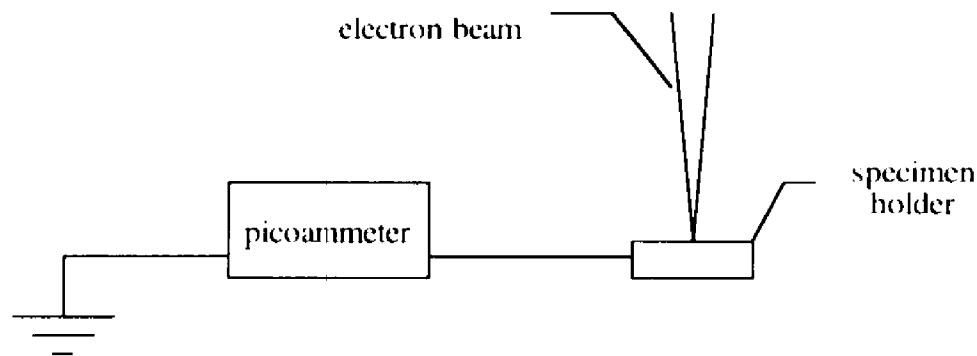
1. Prepare Sample

- a. Spin coat PMMA (9% solids in chlorobenzene; $M_w \sim 495,000$) at 2000 RPM for a duration of 45 secs. Should give thickness of approximately 0.7 micrometers.
- b. Scratch back of wafer with diamond scribe. Break off sample along the scratch. Be sure that the wafer is held between two hard surfaces along the scratch and use a hard cleaving device. Make the cleave quickly trying not to damage the resist layer on the wafer.
- c. Choose 2 samples for exposure.
- d. Attach the samples to the sample holder. Draw a picture of the samples on the sample holder below:



2. Setup ESEM

- a. Insert sample holder into stage fixture. Also insert Faraday cup and hookup wiring as specified below:



- b. Adjust z-axis before evacuating chamber. Press "z-set" when finished.
- c. Evacuate the chamber using "wet" mode.
- d. Set electron accelerating voltage. The following parameter has been chosen for this experiment:
 - electron energy = **5 keV**
- e. Image and save all corners. Also, save the coordinate of the Faraday cup. Number the corners in the picture drawn in step 1.g. Be sure to rotate the specimen until its edges are parallel/perpendicular to the direction of travel.
- f. Adjust beam current to appropriate value at 0.0 torr. The following parameters have been chosen for this experiment:
 - beam current = **50 pA**
 - aperture size = **30 μm**
 - filament type = **Tungsten**
 - filament current = **2.5 A**
 - emission current = **125 μA**

Record condenser setting below:

- condenser =

- g. Determine the magnification needed to get the appropriate beam exposure. Magnification controls scan velocity as follows:

$$V_s = 10^{-(\log(\text{Mag})+4.95)}$$

where

V_s - beam scan velocity ($\mu\text{m}/\text{sec}$)

Mag - magnification of the beam

The following line charge densities, scan velocities, and magnifications have been chosen for this experiment:

- joystick direction = up

| Line Charge Density (C/cm) | Beam Current (C/sec) | Scan Velocity (cm/s) | Magnification (1 X) |
|----------------------------|----------------------|----------------------|---------------------|
| 3.0E-09 | 5.00E-11 | 1.7E-02 | 600 |
| 7.0E-09 | 5.00E-11 | 7.1E-03 | 1400 |
| 1.0E-08 | 5.00E-11 | 5.0E-03 | 2000 |
| 2.0E-08 | 5.00E-11 | 2.5E-03 | 4000 |

- h. Set working distance to about **6 mm** and refocus all four corners at the magnification specified. Set "No Vent Drop".
- i. Record beam current at 0.0 torr.
- beam current =
- j. Set chamber pressure to lowest possible vapor pressure while keeping good line definition. The following parameter has been chosen for this experiment:
- chamber pressure = **0.0 torr**
- k. Turn the contrast off and go to "standby" mode.
- l. Save some points at which the scans will start once the test specimen is inserted. Scans should be about 3 to 5 mm long and 50 μm apart.

| | | | |
|----------------|---------|------------|--|
| # of scans | 4 | | |
| | (+2)·50 | | |
| | -100 | | |
| center of scan | + | | |
| starting x | | starting y | |

3. Expose Specimen

- a. In "standby" mode, move to first (or next) starting point.
- b. Be sure that the following parameters are set:
- aperture size = **30 μm**
 - condenser =
 - chamber pressure = **0.0 torr**
 - contrast = **off**
 - working distance = **6 mm**
- c. Activate "wet" mode.

d. When aperture opens, do the following steps simultaneously:

- Start stop watch.
- Move joystick up.

e. Run joystick for:

| Scan | Scan Length (mm) | Scan Velocity (cm/s) | Scan Time (s) | Scan Time | |
|------|---------------------|-------------------------|------------------|-----------|-----|
| | | | | (min) | (s) |
| 1 | 3 | 1.70E-02 | 17.6 | 0 | 18 |
| 2 | 3 | 7.10E-03 | 42.3 | 0 | 42 |
| 3 | 3 | 5.00E-03 | 60.0 | 1 | 0 |
| 4 | 3 | 2.50E-03 | 120.0 | 2 | 0 |

f. When finished, release joystick and press "standby" simultaneously. Record data in following table.

| Scan | Mag (1x) | Coordinates Before Scan (μm) | | Coordinates After Scan (μm) | | Distance Traveled (μm) | Time (s) | Scan Velocity ($\mu\text{m/s}$) |
|------|-------------|---|---|--|---|---|-------------|--------------------------------------|
| | | x | y | x | y | | | |
| 1 | 600 | | | | | | 18 | |
| 2 | 1400 | | | | | | 42 | |
| 3 | 2000 | | | | | | 60 | |
| 4 | 4000 | | | | | | 120 | |
| 5 | 600 | | | | | | 18 | |
| 6 | 1400 | | | | | | 42 | |
| 7 | 2000 | | | | | | 60 | |
| 8 | 4000 | | | | | | 120 | |

Continue repeating step 3 until the total number of trials have been completed.

g. Record beam current at 0.0 torr.

- beam current =

h. Remove the sample from the specimen chamber.

4. Develop Specimen

- a. Develop specimen by agitation in a developer solvent. Suggested solvent is methyl isobutyl ketone (MIBK) and isopropanol (IPA) in a 1:3 ratio. Slightly agitate the first specimen for 25 seconds and the second 45 seconds. Surface of the specimen should be parallel with the direction of motion.
- b. Rinse in methanol and deionized water and allow to air dry.

5. Image Profile

- a. Deposit ~100 Å gold film on the surface of the specimen.
- b. Image the top of the linewidths in the ESEM and record data on video tape.
- c. Cleave the specimen across the lines and deposit ~100 Å gold film on the profile of the specimen.
- d. Image the top and profile of the specimen in the SEM.

******* This completes the procedure for one wafer. *******

Appendix D. CALCULATIONS OF THE AVERAGE ABSORBED DOSE IN THE ELECTRON RESIST

This appendix provides example calculations for the average absorbed dose. Solubility rate calculations were adapted from the solubility rate model proposed by Kyser and Viswanathan [KYSE75]. These calculations are shown at the top of the page in Appendix D with the material constants shown on the left and an estimate of the solubility rate (SR) on the right. The constants A and B are adapted from the work of Greeneich as reported by Kyser and Viswanathan. The solubility rate is estimated by dividing the measured linedepth by the total development time. These material constants and solubility rate are then used to calculate the average absorbed dosage (Eavg). Calculations for Eavg using the LEEPP model are shown on the bottom half of the page. A line is fit to the line response experienced at the centerline of the beam scan. To get an absorbed dose equation as a function of penetration depth, the line response (in C/cm²) is multiplied by the energy released per electron per unit penetration depth which can be calculated by multiplying the material stopping power [S(Eo)] by its depth dose distribution [J(zz)]. This absorbed dose function is then integrated over the penetration depth and divided by the change in penetration depth to acquire an average absorbed dose.

Mw 495000 zpen 0.5
 g 1.9·10⁻² SR zpen
 ρ 1.1 .75
 Na 6.022·10²³ SR 0.667
 B 9.33·10¹⁴
 A 3.86

$$E_{avg} = \frac{1}{Mw} \cdot \frac{SR \cdot 10^{14}}{B} \cdot \frac{1}{g} \cdot \rho \cdot Na$$

Eavg 4.51·10²²

E_{max} LineResp_{0.5} · J(0.125) · S(Eo) · 10¹²

SR 0.667

E_{low} LineResp_{0.025}^{zpen} · J(zpen) · S(Eo) · 10¹²

k3 zpen
 0.025

kkk 0..k3

zzz_{kkk} z_{kkk} n1

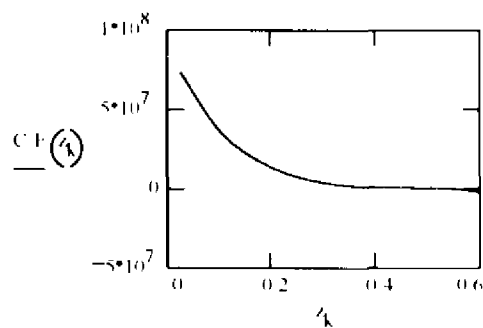
LL_{kkk} LineResp^{1 - 10⁻¹⁰}_{kkk} 3

E_{max} 2.562·10²³

C := linfit(zzz, LL, F) Eavg 4.51·10²²

E_{low} 4.55·10²⁰

$$\frac{\int_{n1-0.025}^{zzz_{k3}} -S(Eo) \cdot J(zz) \cdot C \cdot F(zz) \, dzz}{zzz_{k3} - 0.075} \cdot 10^{12} = 7.791 \cdot 10^{22}$$



k3 20

REFERENCES

- [ABRA93] Abramson, R. 1993. Rapid Tooling Applications at Ford AMDC (Dearborn, MI), Presented at the 1993 Ford Alpha Manufacturing Development Center Rapid Fabrication Seminar, Redford, MI, **October**.
- [ARON93] Aronson, R. B. 1993. So Rapid Prototyping Works: Now What? *Manufacturing Engineering*, **111**(5): 37-42.
- [ASHL92] Ashley, S. 1992. Rapid Mold-making for Investment Casting, *Mechanical Engineering*, **November**, 49-51.
- [BACK91] Backhaus, B. 1991. Saving Time, Money, and Resources, *Agricultural Engineering*, **November**, 11-13, 25.
- [BACK92] Backhaus, B. 1992. Using MCAE and Rapid Prototyping for Casting Design, *SAE Technical Paper Series*, p. 1-6.
- [BEDN93] Bednar, B., Kralicek, J., and Zachoval, J. 1993. *Resists in Microlithography and Printing*, Elsevier: Amsterdam.
- [BETH38] Bethe, H. A., Rose, M. E., and Smith, L. P. 1938. The Multiple Scattering of Electrons, *Proceedings of the American Philosophical Society*, **78**(4): 573-585.
- [BOMA92] Boman, M. and Westberg, H. 1992. Helical Microstructures Grown by Laser Assisted Chemical Vapor Deposition, *Proceedings of the IEEE Conference on Micro Electro Mechanical Systems*, Travemunde, Germany, **February 4-7**, 162-167.
- [BOUR92] Bourell, D. L., Marcus, H. L., Barlow, J. W., and Beaman, J. J. 1992. Selective Laser Sintering of Metals and Ceramics, *The International Journal of Powder Metallurgy*, **28**(4): 369-381.
- [BROD82] Brodie, I. and Muray, J. J. 1982. *The Physics of Microfabrication*, Plenum Press: New York, NY.
- [BRUN92] Brunger, W. H. and Kohlmann, K. T. 1992. E-Beam Induced Fabrication of Microstructures, *Proceedings of the IEEE Conference on Micro Electro Mechanical Systems*, Travemunde, Germany, **February 4-7**, 168-170.
- [BUHR92] Buhr, G., Hagedorn, R., Muller, T., Benecke, W., and Wagner, B. 1992. Pumping of Water Solutions in Microfabricated Electrohydrodynamic Systems, *Proceedings of the IEEE Conference on Micro Electro Mechanical Systems*, Travemunde, Germany, **February 4-7**, 25-30.
- [BURN93] Burns, M. 1993. *Automated Fabrication: Improving Productivity in Manufacturing*, PTR Prentice-Hall, Inc.: Englewood Cliffs, NJ.
- [CHAR60] Charlesby, A. 1960. *Atomic radiation and Polymers*, Pergamon: New York, 371.

- [CLEL76] Cleland, M. R. and Farrell, J. P. 1976. Methods for Calculating Energy and Current Requirements for Industrial Electron Beam Processing, *Proceedings of the Fourth Conference on Application of Small Accelerators*, North Texas State University, Denton, TX.
- [COSS64] Cosslett, V. E. and Thomas, R. N. 1964. Multiple Scattering of 5-30 keV Electrons in Evaporated Metal Films," *Brit. J. Appl. Phys.*, **15**: 883-906.
- [DEGA88] DeGarmo, E. P., Black, J T., and Kohser, R. A. 1988. *Materials and Processes in Manufacturing*, Macmillan: New York, NY.
- [DENT94] Denton, K. R. and Jacobs, P. F. 1994. Quickcast™ & Rapid Tooling: A Case History at Ford Motor Company, *Proceedings of the Fifth International Conference on Rapid Prototyping*, University of Dayton, Dayton, OH, **June 12-15**, 301-319.
- [ELLI86] Elliott, D. J. 1986. *Micro lithography: Process Technology for IC Fabrication*. McGraw-Hill: New York, NY.
- [ENGE92] Engelmann, G., Ehrmann, O., Simon, J., and Reichl, H. 1992. Fabrication of High Depth-to-Width Aspect Ratio Microstructures, *Proceedings of the IEEE Conference on Micro Electro Mechanical Systems*, Travemunde, Germany, **February 4-7**, 93-97.
- [EVER71] Everhart, T. E. and Hoff, P. H. 1971. Determination of Kilovolt Electron Energy Dissipation vs Penetration Distance in Solid Materials," *J. Appl. Phys.*, **42**(13): 5837-5846.
- [FARO92] Farooqui, M. M. and Evans, A. G. R. 1992. Microfabrication of Sub Micron Nozzles in Silicon Nitride, *Proceedings of the IEEE Conference on Micro Electro Mechanical Systems*, Travemunde, Germany, **February 4-7**, 150-153.
- [FEYG89] Feygin, M. 1989. Laminated Object Manufacturing, *Industrial Laser Review*, **3**(10).
- [FRAZ92] Frazier, A. B. and Allen, M. G. 1992. High Aspect Ratio Electroplated Microstructures Using a Photosensitive Polyimide Process, *Proceedings of the IEEE Conference on Micro Electro Mechanical Systems*, Travemunde, Germany, **February 4-7**, 87-92.
- [FUJI93] Fujita, H. 1993. Microfabrication and Micromachines, in *Modern Tools for Manufacturing Systems*, R. Zurawski and T. S. Dillon (Eds.), Elsevier Science Publishers, 409-416.
- [GIAN92] Gianchandani, Y. and Najafi, K. 1992. Batch Fabrication and Assembly of Micromotor-Driven Mechanisms with Multi-Level Linkages, *Proceedings of the IEEE Conference on Micro Electro Mechanical Systems*, Travemunde, Germany, **February 4-7**, 141-146.
- [GLEZ92] Glezos, N., Raptis, I., Tsoukalas, D., and Hatzakis, M. 1992. Application of a New Analytical Technique of Electron Distribution Calculations to the Profile Simulation of a High Sensitivity Negative Electron-Beam Resist, *J. Vac. Sci. Tech. B*, **10**(6): 2606-2609.

- [GLEZ94] Glezos, N., Raptis, I., and Hatzakis, M. 1994. LITHOS: A Fast Electron Beam Lithography Simulator, *Microelectronic Engineering*, **23**: 417-420.
- [GREE74] Greeneich, J. S. and Van Duzer, T. 1974. An Exposure Model for Electron-Sensitive Resists, *IEEE Transactions on Electron Devices*, **ED-21**(5): 286-299.
- [GRIF94] Griffin, C., Daufenbach, J., and McMillin, S. 1994. Desktop Manufacturing: LOM vs. Pressing, *American Ceramic Society Bulletin*, **73**(8): 109-113.
- [GUIL85] Guillet, J. 1985. *Polymer Photophysics and Photochemistry: An Introduction to the Study of Photoprocesses in Macromolecules*, Cambridge University Press: Cambridge, England.
- [HATZ71] Hatzakis, M. 1971. New Method of Observing Electron Penetration Profiles in Solids, *Applied Physics Letters*, **18**(1): 7-10.
- [HAWR72] Hawryluk, R. J. 1972. Electron Beam Exposure Profiles in Thin Polymer Films, *Int'l Conf. Electron Ion Beam Sci. Tech.*, Electrochemical Society: Princeton, NJ, **5**, 51-67.
- [HAWR74] Hawryluk, R. J., Hawryluk, A. M., and Smith, H. I. 1974. Energy Dissipation in a Thin Polymer Film by Electron Beam Scattering, *J. Appl. Phys.*, **45**(6): 2551-2566.
- [HERZ71] Herzog, R. F., Greeneich, J. S., Everhart, T. E., and Van Duzer, T. 1971. Computer-Controlled Resist Exposure in the Scanning Electron Microscope, *Record of the 11th Symposium on Electron, Ion, and Laser Beam Technology*, San Francisco Press: San Francisco, CA, **May 12-14**, 483-494.
- [HJOR90] Hjort, K., Schweitz, J. and Hok, B. 1990. Bulk and Surface Micromachining of GaAs Structures, *Proceedings of the IEEE Conference on Micro Electro Mechanical Systems*, Napa Valley, CA, **February 11-14**, 73-76.
- [HOFF73] Hoffman, C. R. 1973. Electron Beam Curing - A Non-Polluting System, in *Nonpolluting Coatings and Coating Processes*, J. L. Gardon and J. W. Prane (eds.), Plenum: New York, 195-206.
- [HOWA93] Howard, D. 1993. Rapid Tooling Applications at Ford PTO (Livonia, MI), Presented at the 1993 Ford Alpha Manufacturing Development Center Rapid Fabrication Seminar, Redford, MI, **October**.
- [IKUT93] Ikuta, K. and Hirowatari, K. 1993. Real Three Dimensional Micro Fabrication Using Stereo Lithography and Metal Molding, *Proceedings of the IEEE International Workshop on Micro Electro Mechanical Systems*, 42-47.
- [IKUT94] Ikuta, K., Hirowatari, K., and Ogata, T. 1994. Ultra-High Resolution Stereo Lithography for Three Dimensional Micro Fabrication, *Proceedings of the Fifth International Conference on Rapid Prototyping*, University of Dayton, Dayton, OH, **June 12-15**, 42-47.

- [INVE94] Investment Casting with Rapid Prototyping Patterns, 1994. *Rapid Prototyping Report*, **November**, 2-5.
- [JACO74] Jacob, J. H. 1974. Penetration and Energy Deposition of Electrons in Thick Targets, *J. Appl. Phys.*, **45**(1): 467-475.
- [JACO92] Jacobs, P. F. 1992. *Rapid Prototyping and Manufacturing: Fundamentals of Stereolithography*, Society of Manufacturing Engineers: Dearborn, MI.
- [JACO94] Jacobs, P. 1994. Presentation at the Vendors Forum, *Fifth International Conference on Rapid Prototyping*, University of Dayton, Dayton, OH, **June 12-15**.
- [JOY88] Joy, D. C. 1988. An Introduction to Monte Carlo Simulations, *Proceedings of EUREM 88*, York, England, Inst. Phys. Conf. Ser. No. 93: **1**, 23-32.
- [JUDY91] Judy, M., Cho, Y., Howe, R., and Pisano, A. 1991. Self-Adjusting Microstructures (SAMS), *Proceedings of the IEEE Conference on Micro Electro Mechanical Systems*, Nara, Japan, **January 30 - February 2**, 51-56.
- [KALP92] Kalpakjian, S. 1992. *Manufacturing Engineering and Technology*, Addison-Wesley: Reading, MA.
- [KOCH93] Kochan, D. 1993. *Solid Freeform Manufacturing*, Elsevier: Amsterdam.
- [KRUT91] Kruth, J. P. 1991. Material Incess Manufacturing by Rapid Prototyping Techniques, *CIRP Annals*, **40**(2): 603-614.
- [KYSE74] Kyser, D. F. and Murata, K. 1974. Monte Carlo Simulation of Electron Beam Scattering and Energy Loss in Thin Films on Thick Substrates, *Int. Conf. Electron Ion Beams Sci. Tech.*, (R. Bakish, ed.), Electrochemical Society, Princeton, NJ, **6**, 205.
- [KYSE75] Kyser, D. F. and Viswanathan, N. S. 1975. Monte Carlo Simulation of Spatially Distributed Beams in Electron-Beam Lithography, *J. Vac. Sci. Technol.*, **12**(6): 1305-1308.
- [LEWA91] Lewald, R. 1991. New Approach in Rapid Prototyping, *American Machinist*, **December**, 52-54.
- [LOVE78] Love, G., Cox, M. G., and Scott, V. D. 1978. A Versatile Atomic Number Correction for Electron-Probe Microanalysis, *J. Phys. D: Appl. Phys.* **11**: 7-21.
- [MARC90A] Marcus, H., Beaman, J., Barlow, J., and Bourell, D. 1990. From Computer to Component in 15 Minutes: The Integrated Manufacture of Three-Dimensional Objects, *Journal of Manufacturing*, **April**: 8-10.
- [MARC90B] Marcus, H. L., Beaman, J. J., Barlow, J. W., and Bourell, D. L. 1990. Solid Freeform Fabrication: Powder Processing, *Ceramic Bulletin*, **69**(6): 1030-1031.

- [MCCO92] McCord, M. A. and Newman, T. H. 1992. Low Voltage, High Resolution Studies of Electron Beam Resist Exposure and Proximity Effect, *J. Vac. Sci. Tech. B*, **10**(6): 3083-3087.
- [MENZ91] Menz, W., Bacher, W., Harmening, M., and Michel, A. 1991. The LIGA Technique - a Novel Concept for Microstructures and the Combination with Si-Technologies by Injection Molding, *Proceedings of the IEEE Conference on Micro Electro Mechanical Systems*, Nara, Japan, **January 30 - February 2**, 141-146.
- [MORI93] Morishita, H. and Hatamura, Y. 1993. Development of Ultra Manipulator System Under Stereo SEM Observation, *Proceedings of the IEEE/RSJ International Conference on Intelligent Robots and Systems*, Yokohama, Japan, **July 26-30**, 1717-1721.
- [MUEL92A] Mueller, T. 1992. Stereolithography: A Rapid Way to Prototype Die Cast Parts, *Die Casting Engineer*, **36**(3): 28-33.
- [MUEL92B] Mueller, T. 1992. Using Rapid Prototyping Techniques to Prototype Metal Castings, *SAE Technical Paper Series*, 1-5.
- [MULL90] Muller, R. S. 1990. *Sensors and Actuators*, **A21-A23**: 1-8.
- [NOSK69] Nosker, R. W. 1969. Scattering of Highly Focused Kilovolt Electron Beams by Solids, *J. Appl. Phys.*, **40**(4): 1872-1883.
- [O'CON93] O'Connor, L. 1993. Tiny Devices Take on Tough Tasks in Biomedicine, *Mechanical Engineering*, **December**: 62-67.
- [PACH93] Pacheco, J. 1993. *Rapid Prototyping*, Department of Defense, Manufacturing Technology Information Analysis Center, Chicago, IL, Contract number DLA900-90-D-0134.
- [PAK94] Pak, S. S. and Nisnevich, G. 1994. Interlaminar Strength and Processing Efficiency Improvements in Laminated Object Manufacturing, *Proceedings of the Fifth International Conference on Rapid Prototyping*, University of Dayton, Dayton, OH, **June 12-15**, 171-180.
- [PETE82] Petersen, K. E. 1982. Silicon as a Mechanical Material, *Proceedings of the IEEE*, **70**(5): 420-457.
- [PETE92] Peterson, P. A., Radzinski, Z. J., Schwalm, S. A., and Russell, P. E. 1992. Low-Voltage Electron Beam Lithography, *J. Vac Sci Tech. B.*, **10**(6): 3088.
- [POSS75] Possin, G. E. and Norton, J. F. 1975. Spatial Distribution of 5 and 10 Kilovolt Electron Beam Ionization in Solids, *Proceedings of the 8th Annual SEM Symposium*, IIT Research Institute, Chicago, IL, 458.
- [RAO74] Rao-Sahib, T. and Wittry, D. B. 1974. X-ray Continuum from Thick Elemental Targets for 10-50 keV Electrons, *J. Appl. Phys.*, **45**(11): 5060-5068.

- [RAPT93A] Raptis, I., Glezos, N., and Hatzakis, M. 1993. Use of the Boltzmann Transport Equation for the Evaluation of Energy Deposition in the Case of Electron Sensitive Resist Films over Composite Substrates, *Microelectronic Engineering*, **21**: 289-292.
- [RAPT93B] Raptis, I., Glezos, N., and Hatzakis, M. 1993. Analytical Evaluation of the Energy Deposition Function in Electron-Beam Lithography in the Case of a Composite Substrate, *J. Vac. Sci. Tech. B*, **11**(6): 2754-2757.
- [REIM79] Reimer, L. 1979. Electron-Specimen Interactions, *Scanning Electron Microscopy*, **II**: 111-123.
- [ROVI94] Rovick, J. S. 1994. An Additive Fabricator for High-Speed Production of Artificial Limbs, *Proceedings of the Fifth International Conference on Rapid Prototyping*, University of Dayton, Dayton, OH, **June 12-15**, 47-56.
- [RUSS93] Russell, A. R. 1993. Development of a Robotic Manipulator for Micro-assembly Operations, *Proceedings of the IEEE/RSJ International Conference on Intelligent Robots and Systems*, Yokohama, Japan, **July 26-30**, 471-474.
- [SACH92] Sachs, E., Cima, M., Bredt, J., Curodeau, A., Fan, T., and Brancazio, D. 1992. CAD-Casting: Direct Fabrication of Ceramic Shells and Cores by Three Dimensional Printing, *Manufacturing Review*, **5**(2): 117-126.
- [SARK94] Sarkis, B. and Kennerknecht, S. 1994. Rapid Prototype Casting: The Fundamentals of Producing Functional Metal Parts from Rapid Prototyping Models, *Proceedings of the Fifth International Conference on Rapid Prototyping*, University of Dayton, Dayton, OH, **June 12-15**, 291-300.
- [SCHA93] Schaer, L. 1993. Mold Fabrication Services for Rapid Tooling Applications at Tekcast Industries (New Rochelle, NY), Presented at the 1993 Ford Alpha Manufacturing Development Center Rapid Fabrication Seminar, Redford, MI, **October**.
- [SCHI82] Schiller, S., Heisig, U., and Panzer, S. 1982. *Electron Beam Technology*, John Wiley and Sons: New York, NY.
- [SCHM94] Schmidt, L. D. 1994. A Benchmarking Comparison of Commercial Techniques in Rapid Prototyping, *Proceedings of the Fifth International Conference on Rapid Prototyping*, University of Dayton, Dayton, OH, **June 12-15**, 333-352.
- [SCOT49] Scott, W. T. 1949. Correlated Probabilities in Multiple Scattering, *Physical Review*, **76**(2): 212-219.
- [SENI84] Senich, G. A. and Florin, R. E. 1984. Radiation curing of coatings, *JMS Rev. Macromol. Chem. Phys.*, **C24**(2): 239-324.
- [SHEP93] Sheppard, R. 1993. Engineered Tool Assembly Services at Weber Nickel Tooling Technology (Midland, Ontario, Canada), Presented at the 1993 Ford Alpha Manufacturing Development Center Rapid Fabrication Seminar, Redford, MI, **October**.

- [SLOC92] Slocum, A. H. 1992. Precision Machine Design: Macromachine Design Philosophy and Its Applicability to the Design of Micromachines, *Proceedings of the IEEE Conference on Micro Electro Mechanical Systems*, Travemunde, Germany, **February 4-7**, 37-42.
- [SPEN55] Spencer, L. V. 1955. Theory of Electron Penetration, *Phys. Rev.*, **98**(6): 1597-1615.
- [SPEN59] Spencer, L. V. 1959. *Energy Dissipation by Fast Electrons*, United States Department of Commerce, National Bureau of Standards, Monograph 1, September 10.
- [SUGI88] Sugita, A. and Tamamura, T. 1988. Resist Exposure Characteristics by a Focused Low Energy Electron Beam, *J. Electrochem. Soc.*, **135**(7): 1741-1746.
- [TAKA93] Takagi, T. and Nakajima, N. 1993. Photoforming Applied to Fine Machining, *Proceedings of the IEEE International Workshop on Micro Electro Mechanical Systems*, 173-178.
- [TRIM87] Trimmer, W. S. N. and Gabriel, K. J. 1987. Design Considerations for a Practical Electrostatic Micro-motor, *Sensors and Actuators*, **11**, 189-206.
- [UZIE93] Uziel, Y. 1993. An Unconventional Approach to Producing Investment Castings, *Modern Casting*, **August**, 30-31.
- [VANL88] Van Lintel, H. T. G., van de Pol, F. C. M., and Bouwstra, S. 1988. A Piezoelectric Micropump Based on Micromachining of Silicon, *Sensors and Actuators*, **15**: 153-167.
- [WEIS90] Weiss, L., Gursoz, E., Prinz, F., Fussell, P., Mahalingame, S., and Patrick, E. 1990. A Rapid Tool Manufacturing System Based on Stereolithography and Thermal Spraying, *Manufacturing Review*, **3**(1): 40-48.
- [WILS74] Wilson, J. E. 1974. *Radiation Chemistry of Monomers, Polymers, and Plastics*, Marcel Dekker, Inc.: New York.
- [WISE91] Wise, K. D. 1991. Integrated Microelectromechanical Systems: A Perspective on MEMS in the 90's, *Proceedings of the IEEE Conference on Micro Electro Mechanical Systems*, Nara, Japan, **January 30 - February 2**, 141-146.
- [WISE93] Wise, S. 1993. CEMCOM Corporation: Baltimore, MD, Telephone interview.
- [WOLF71] Wolf, E. D., Ozdemir, F. S., Perkins, W. E., and Coane, P. J. 1971. Response of the Positive Electron Resist Elvacite 2041 to Kilovolt Electron Beam Exposure, *Record of the 11th Symposium on Electron, Ion, and Laser Beam Technology*, R. F. M. Thornley (Ed.), San Francisco Press, Inc.: San Francisco, CA, 331-336.

Brian K. Paul

Upon graduation, Brian K. Paul became an Assistant Professor of Industrial Engineering at Oregon State University in Corvallis, Oregon. Before attending school at the Pennsylvania State University, he was affiliated with the Department of Energy's Pacific Northwest Laboratory (PNL) in Richland, Washington, where he worked as a Senior Research Engineer in manufacturing production systems analysis and design. Before working at PNL, Dr. Paul also worked as a Manufacturing Engineering Consultant with McDonnell Douglas Helicopter Company (1989); Manufacturing Systems Engineer for the Honeywell Industrial Automation Systems Division (1986-1989); and Industrial Engineer for the Boeing Military Airplane Company (1986).

He obtained his Ph.D. degree in Industrial and Manufacturing Engineering from the Pennsylvania State University in 1995 while employed at PNL, following his M.S. degree in Industrial Engineering from Arizona State University (1988) and his B.S. in Industrial Engineering from the Wichita State University (1985).

He is a Society of Automotive Engineers Doctoral Fellow (1992-1995), a Pennsylvania State University Benjamin Niebel Manufacturing Fellow (1992-1993), and a Honeywell Industrial Fellow in Computer-Integrated Manufacturing at Arizona State University (1986-1988). His awards include the Arizona State University Corporate Leaders Community Service Award (1993), Outstanding Young Men of America (1990), Excellence in Engineering Design Award from the Wichita Engineering Association (1985), and Outstanding Student Award from the Institute of Industrial Engineers (1985). He is listed in *Who's Who Among Students in American Universities and Colleges*, has served as editor for numerous society newsletters, and holds memberships in the American Powder Metallurgy Institute, Society of Manufacturing Engineers, and Institute of Industrial Engineers. He has consulted or performed research for many companies and government agencies. He is an Elected Member of Tau Beta Pi, Alpha Pi Mu, Mortarboard, and Omicron Delta Kappa.

Dr. Paul has written numerous technical journal articles and book chapters on manufacturing processes and systems. His research and teaching interests include rapid product development, micro-mechanical fabrication, and integrated manufacturing systems design. Example research projects and applications include micro-scale freeform fabrication using low-energy electron beam degradation of polymers, manufacturing system design of a repetitive remanufacturing facility, and synchronization of master schedules in an electronic assembly environment.